UNIVERSITÀ DEGLI STUDI FIRENZE

DOTTORATO DI RICERCA IN
Fisica e Astronomia

CICLO XXXV

COORDINATORE Prof. Raffaello D'Alessandro

Search for the Vector Boson Scattering process in $W^+W^- \to 2\ell2\nu$ final state with the CMS detector

Settore Scientifico Disciplinare FIS/04

Dottorando
Dott. Mattia Lizzo

Tutore
Prof. Piergiulio Lenzi

Coordinatore
Prof. Raffaello D'Alessandro

Anni 2019/2022

PhD in
Physics and Astronomy
Cycle XXXV

Search for the Vector Boson Scattering process in $\mathbf{W^+W^-} \rightarrow \mathbf{2\ell2\nu}$ final state with the CMS detector

Tutor:
Prof. Piergiulio Lenzi

Coordinator:
Prof. Raffaello D'Alessandro

Candidate:
Dr. Mattia Lizzo

Years:
2019-2022

Apprendre n'est pas savoir; il y a les sachants et les savants:
c'est la mémoire qui fait les uns, c'est la philosophie qui fait les autres.

Alexandre Dumas

Contents

Introduction

The discovery of the Higgs boson by the ATLAS and CMS collaborations at the CERN Large Hadron Collider (LHC) in 2012, and the ever increasing amount of data collected since then by the LHC, have generated fertile soil for the flourishing of precise measurements in the electroweak (EW) sector of the Standard Model (SM).

In this context, Vector Boson Scattering (VBS) processes, i.e., scattering diagrams among gauge vector bosons, are of great interest because of the action of the Higgs boson in preventing the unitarity violation of their cross sections in the high energy limit. The role of the Higgs boson mass in EW scattering has been known for decades, and VBS amplitudes are strongly dependent on this parameter, which ATLAS and CMS experiments have measured to be 125 GeV.

The VBS process is therefore ideal to test the structure of EW interactions, where the interplay between trilinear and quartic gauge couplings gives rise to a precise cancellation of terms, which, without a light Higgs boson, would be otherwise divergent. These processes are also particularly sensitive to beyond SM phenomena that may manifest as deviations in the tail of high energy spectra, like anomalous gauge couplings, and hence they can extend the reach of new physics direct searches.

However, unprecedent luminosity of data at the TeV energy scale and extremely precise knowledge of all background sources are mandatory to enable the study of these rare interactions at the LHC. As a matter of fact, the first VBS observation was only reported in 2018, where the EW production cross section of two W bosons having the same electric charge was measured. In recent years, more evidence and observations have been reported as other VBS channels were studied; nevertheless, among diboson final states, the one with two oppositely-charged W bosons has remained untackled so far, mainly because of the large background contamination affecting this mode.

The goal of this thesis is to deal with such a mechanism by considering the subsequent decay of each W boson into a light lepton (electron or muon) and its corresponding neutrino. Eventually, this has led to the first obser-

vation of the EW W^+W^- production, and its cross section is measured in a fiducial volume close to the reconstructed selection, in order to minimize extrapolation uncertainties. The analysis comprises the cases where the two leptons have either different ($e\mu$) or same leptonic flavor (ee and $\mu\mu$) and dedicated techniques are used to address these final states.

My contributions to this result are manifold and mostly outlined in Chapters 4, 5 and 6. I have carried out extensive studies on the background estimation and signal characterization, by employing several event generator tools designed for high energy physics, with the aim of assessing the robustness of our Monte Carlo (MC) predictions, and correct for relevant discrepancies with data arising in control regions. In particular, I compared different matrix element and parton showering simulations for the signal sample and I took care of validating the main background processes, by devising alternative strategies to estimate them whenever MC samples failed in doing so.

Moreover, I conceived the analysis categorization to select signal event candidates and fine-tuned the separation between signal and background processes in signal regions, chose the discriminating variables for the signal cross section extraction, combined the two leptonic channels, and, finally produced all the relevant numbers, plots and tables. The implementation and optimization of the Deep Neural Network (DNN) in the $e\mu$ final state, which will be described in Sec. 5.3, is not part of my work and it replaced the results I obtained with a simpler kinematic observable, as this approach helped us achieving slightly better performances.

This analysis is based on the Run 2 data set collected by the CMS experiment from 2016 to 2018, which corresponds to an integrated luminosity of 138 fb^{-1}. Results are in agreement with SM predictions within one standard deviation; they are publicly available in the CERN Document Server database [1] and have been accepted by the Physics Letters B journal.

Chapter 1

Vector boson scattering physics at the LHC

In this chapter, the Standard Model of particle physics (SM) is briefly described, focusing on the main aspects of the electroweak (EW) and strong interactions, with some special regards towards the EW symmetry breaking mechanism. Basic concepts related to physics at the Large Hadron Collider (LHC) are described in Secs. 1.1 and 1.2, mainly concerning proton-proton collisions kinematics and dynamics; a wide overview about current vector boson scattering experimental results is finally presented in Sec. 1.4.

1.1 The Standard Model of particle physics

The SM is a renormalizable quantum field theory [2] based on the local gauge symmetry $SU(3)_C \otimes SU(2)_L \otimes U(1)_Y$. The SM describes elementary particles, experimentally defined as point-like physics objects whose internal structure has not been observed at any energy scale. According to the SM, particles interact through EW and strong forces and they are characterized by two Lorentz invariants, the mass and the spin.

Ordinary matter constituents are spin-1/2 particles called fermions, further divided in two families: quarks and leptons. Both families are organized into three doublets of particles, known as generations, ordered according to an increasing mass hierarchy.

Leptons can interact only via the EW force and each doublet is composed by a particle with electric charge $Q = -1$ (electron e, muon μ, tau τ) and its corresponding null charge neutrino (ν_e, ν_μ, ν_τ):

$$\begin{pmatrix} \nu_e \\ e \end{pmatrix}, \begin{pmatrix} \nu_\mu \\ \mu \end{pmatrix}, \begin{pmatrix} \nu_\tau \\ \tau \end{pmatrix}$$

Quarks are sensitive to both EW and strong interactions: u-like quarks (up u, charm c, top t) have $Q = 2/3$, while d-like quarks (down d, strange s, bottom/beauty b) have $Q = -1/3$:

$$\begin{pmatrix} u \\ d \end{pmatrix}, \begin{pmatrix} c \\ s \end{pmatrix}, \begin{pmatrix} t \\ b \end{pmatrix}$$

In addition, quarks carry a color charge, but they are forced to form colorless bound states called hadrons. For each of these particles, a corresponding antiparticle exists, sharing the same mass and spin but with opposite sign additive quantum numbers. Within the SM, interactions between fermions occur through spin-1 bosons exchange. The photon (γ), along with the $W^\pm$ and Z bosons, are responsible for the EW force, and eight gluons (g) mediate the strong coupling between quarks. Their masses are shown in Table 1.1.

Interaction	Mediator	Mass (GeV)
	γ	0
Electroweak	$W^\pm$	80.377 ± 0.012
	Z	91.1876 ± 0.0021
Strong	g	0

Table 1.1: Masses of mediator particles in the SM [3].

$SU(3)_C$ is assumed to be an exact symmetry of the theory and it provides an accurate description for strong interaction phenomena. On the other hand, the $SU(2)_L \otimes U(1)_Y$ symmetry accounts for the EW part of the SM lagrangian density and has to be broken because otherwise both fermions and gauge bosons would be massless, which is experimentally disproved.

This problem is solved by introducing a scalar (or spin-0) field, known as the Higgs field (H), whose mass m_H is a free parameter of the model, hence it has to be measured. Technical details on how particles acquire their mass, as well as other features of the SM interactions, are discussed in the next sections.

1.1.1   Electroweak interactions

The theory of EW interactions, which embeds quantum electro-dynamics (QED), was formulated in the 1960s by S. L. Glashow [4], A. Salam [5] and S. Weinberg [6] as a non-Abelian gauge field theory, whose lagrangian density is required to be invariant under transformations of $SU(2)_L \otimes U(1)_Y$ symmetry group.

The Casimir operator[1] of the $SU(2)_L$ group is the weak isospin[2] T^2 while that of $U(1)_Y$ is the hypercharge Y thus, the fermionic fields can be taken as eigenstates of both Y and T^2, with eigenvalues respectively Y and $T(T+1)$.

It can be shown that the particle hypercharge and weak isospin are related to its electric charge Q by the following equation:

$$Q = T_3 + \frac{Y}{2} \tag{1.1}$$

where T_3 is the component of T along the third axis, arbitrarily chosen as the quantization axis.

The particle vector state ψ can be split into its chiral components ψ_L (left) and ψ_R (right) which are eigenstates for the projection operators χ_L and χ_R respectively. However, based on the observation of the parity symmetry violation in EW interactions, only the left (right) part of the particle (antiparticle) state is required to be a $T = 1/2$ weak-isospin doublet, while the other component is included as a singlet with $T = 0$. A summary is given in Table 1.2.

Elementary particle	T	T_3	Y	Q
Neutrinos	1/2	1/2	-1	0
Leptons	1/2	-1/2	-1	-1
u-quarks	1/2	1/2	1/3	2/3
d-quarks	1/2	-1/2	1/3	-1/3

Table 1.2: Quantum numbers of matter constituents under the $SU(2)_L \otimes U(1)_Y$ symmetry group.

From this consideration, along with the requirement of local invariance under a generic $SU(2)_L$ transformation, two problems arise:

- Fermionic fields are massless;

- Gauge bosons are massless.

The introduction of the Higgs boson allows the theory to predict the experimental evidence of the particle masses.

---

[1]It is defined as the operator that commutes with all the symmetry group's generators.
[2]Weak isospin T is a spin operator since the commutation rules for its components are:

$$[T_i, T_j] = i\epsilon_{ijk}T_k$$

1.1.2   The Higgs mechanism

As already mentioned, without further prescriptions, neither fermions nor gauge bosons are allowed to have mass different from zero. In order to deal with this incongruence and, at the same time, to preserve the description of the EW force provided by the $SU(2)_L \otimes U(1)_Y$ symmetry group, the existence of an additional complex scalar field is postulated, which enters in the lagrangian density as an isospin doublet:

$$\phi = \begin{pmatrix} \phi^+ \\ \phi^0 \end{pmatrix} = \frac{1}{\sqrt{2}} \begin{pmatrix} \phi_1 + i\phi_2 \\ \phi_3 + i\phi_4 \end{pmatrix} \tag{1.2}$$

where ϕ_i is a real field for $i = \{1, 2, 3, 4\}$.

The proposed solution is the spontaneous symmetry breaking (SSB) mechanism, also known as the Higgs mechanism [7]: while the EW lagrangian density intrinsically maintains its symmetry properties, the energy ground state (or vacuum state) is degenerate under a $SU(2)_L \otimes U(1)_Y$ transformation. The simplest interaction term for the ϕ doublet that does not violate the theory's renormalizability is given by:

$$V(\phi) = \mu^2 \phi^\dagger \phi + \lambda (\phi^\dagger \phi)^2 \tag{1.3}$$

The shape of the potential $V(\phi)$ depends on the μ and λ parameters. For instance, the condition $\lambda > 0$ sets a lower bound to the energy spectrum and ensures the existence of a ground state. Moreover, if μ is taken such that $\mu^2 < 0$, then the potential has the famous "mexican hat" shape shown in Fig. 1.1, which gives a minimum for:

$$\phi^\dagger \phi = -\frac{\mu^2}{2\lambda} \equiv \frac{v^2}{2} \tag{1.4}$$

Since $V(\phi)$ is rotationally invariant in the ϕ-space, it follows that there is a set of degenerate states spanned by the relation (1.4). Within a perturbation theory, as the SM is, the lagrangian density is expanded around the potential's minimum, which corresponds to one of the vacuum states that must be chosen amongst those satisfying equation (1.4). A given group of symmetries is said to be spontaneously broken once such a choice is performed.

When breaking the EW symmetry group $SU(2)_L \otimes U(1)_Y$ some care is needed: since the photon has null mass it means that the Higgs mechanism has to preserve the electromagnetic symmetry. In other words, only the W$^\pm$ and Z gauge bosons must acquire mass and this is achieved by requiring the lagrangian density to be invariant under $U(1)_Q$ transformations. Hence, the ground state ϕ_0 has to be electrically neutral and can be chosen as:
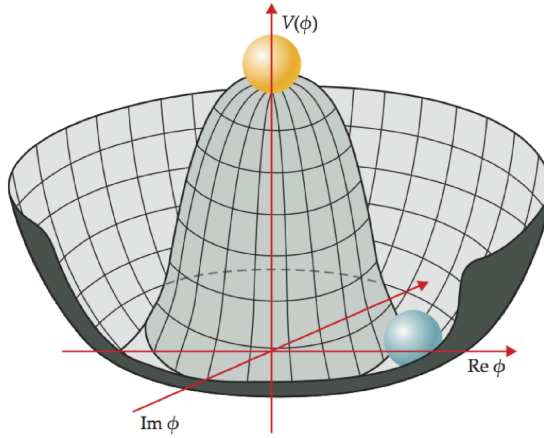
Figure 1.1: V(ϕ) behaviour for $\lambda > 0$ and $\mu^2 < 0$.

$$\phi_0 = \frac{1}{\sqrt{2}} \begin{pmatrix} 0 \\ v \end{pmatrix} \tag{1.5}$$

The ϕ field can be then expanded at first order as:

$$\phi(x) = \frac{1}{\sqrt{2}} \begin{pmatrix} 0 \\ v + H(x) \end{pmatrix} \tag{1.6}$$

where $H(x)$ represents the perturbation around the minimum and is the field associated to the Higgs boson.

The boson masses arises naturally when inserting (1.6) into the kinetic term of the scalar field:

$$m_W = \frac{v}{2}g, \qquad m_Z = \frac{v}{2}\sqrt{g^2 + g'^2}, \qquad m_H = v\sqrt{2\lambda} \tag{1.7}$$

where v, g, g' and λ are free parameters of the model.

Nevertheless, the Higgs mechanism does not account for the origin of the fermion masses, which is explained by introducing in the lagrangian density a coupling term, known as Yukawa coupling, between the fermion doublets and the Higgs field. Thus, all the massive fields within the SM interact with the Higgs boson through a term that is found to be proportional to the particle's mass itself.

EW theory predictions have been experimentally confirmed with outstanding precision since the discovery of the $W^\pm$ and Z gauge bosons during the 80s. The Higgs boson was the final missing piece until 2012, when the CMS and ATLAS collaborations at the Large Hadron Collider (LHC) in Geneve reported the observation of a new particle with mass around 125

GeV [8–10]. The properties of this particle are found to be consistent with those of the SM Higgs boson within the current experimental uncertainties.

1.1.3   Strong interactions

Phenomena involving the strong interaction are described by quantum chromodynamics (QCD), a non-Abelian gauge theory [11] based on the $SU(3)_C$ symmetry group. The requirement of the strong lagrangian density to be invariant under $SU(3)_C$ transformations, along with the fact that the group algebra has eight generators, gives rise to eight massless gauge boson mediators, called gluons.

The color symmetry is assumed to be exact, i.e. unbroken. As the electric charge is ensured to be conserved by the $U(1)_Q$ symmetry, similarly the invariance under $SU(3)_C$ transformations preserves a physics quantity called color, which may assume three different values for particle (blue, green and red) and antiparticle (anti-blue, anti-green and anti-red).

All color charged fields interact with each other by exchanging gluons but, differently from QED, the non-Abelian nature of the theory introduces some particular features. For instance, gauge bosons carry their own color charge[3], which are responsible for these particle to self-interact.

Furthermore, the QCD coupling constant[4] α_s is a decreasing function of the transferred momentum Q^2 between strong interacting particles, as it is shown in Fig. 1.2; two consequences arise from this consideration:

- At large Q scale, α_s approaches to zero and quarks can be considered as quasi-free interacting particles (asymptotic freedom [12]). In this scenario, cross section calculations can be carried out through perturbative methods such as those developed by perturbative QCD (pQCD).

- At low Q scale, a perturbative approach does not hold because the theory can not be expanded in series of α_s powers. In this regime, the intensity of the force increases with the distance, until the creation of a new quark-antiquark pair from the vacuum becomes more energetically advantageous than further increasing the interaction strength itself. This phenomena is called color confinement and is the reason why quarks can never be observed isolated. Instead, they form hadrons, which are colorless bound states.

---

[3]There are eight gluon color charges and they are different from those assigned to quarks and antiquarks.

[4]Within a quantum field theory, the coupling constant gives a measure of the intensity of the force.
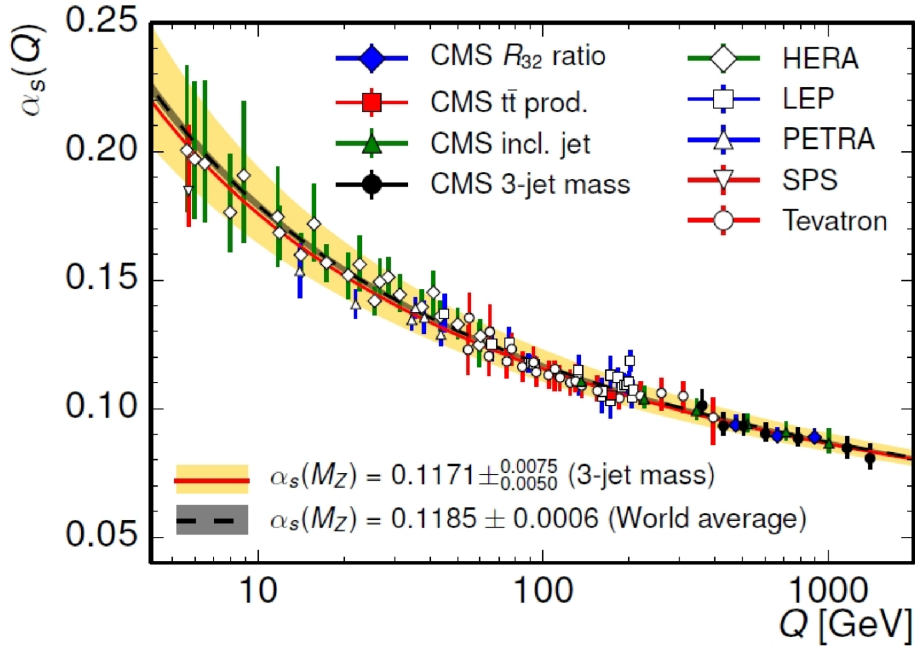
Figure 1.2: α_s running behaviour as a function of Q.

1.2   Proton-Proton collisions

In a single proton-proton (pp) collision at the LHC the energy in the center of mass system is on the TeV scale and the internal structure of the protons becomes relevant for describing the scattering process.

Protons are hadrons made up by three valence quarks (uud) surrounded by a sea of virtual quark-antiquark pairs, which are continually created and annihilated through the absorption and the emission of gluons. Thus, an inelastic collision can be naively seen as a quasi-free scattering of point-like constituents called partons which carry a fraction x of the hadron four-momentum. The probability density function $f(x)$ associated to this variable is the parton distribution function (PDF) and its normalization requires that:

$$\sum_i \int_0^1 x f_i(x) dx = 1 \qquad (1.8)$$

where the index i runs over all the partons. PDFs are predominantly measured in deep inelastic electron-proton scattering experiments and their shapes depend on the energy scale μ at which they are evaluated, as shown in Fig. 1.3. As long as the strong interaction coupling constant α_s is small, which is true in the high energy regime, the dynamics can be treated pertur-

batively and the evolution of the PDFs with respect to μ can be inferred by using the DGLAP equations [13].
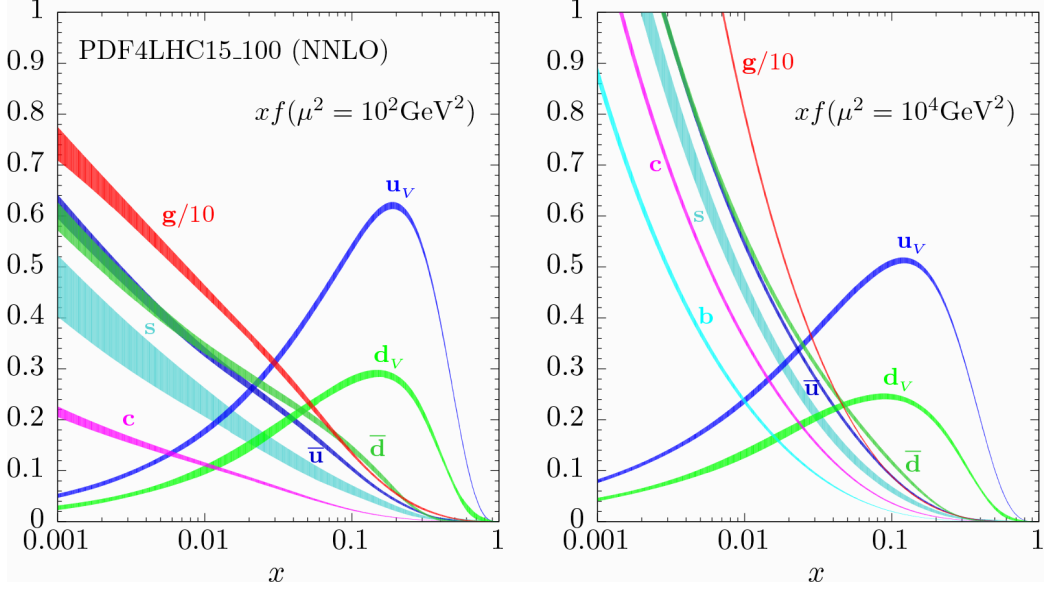
Figure 1.3: Parton distribution functions multiplied by x and evaluated at $\mu = 100$ GeV (on the left) and $\mu = 10$ TeV (on the right), which corresponds to the LHC energy scale.

Within a pp collision, several partons can interact. In the processes that are relevant for high energy physics experiments, typically a parton pair undergoes a large transferred momentum interaction, referred to as the hard scattering. Other partons in the two colliding protons give rise to softer scattering processes. At the LHC, the hard scattering is the physics event of interest because it allows for the production of a variety of particles with high transverse momentum. The soft component of the interaction is known as the underlying event, which is described by models implemented in Monte Carlo (MC) event generators. In most collisions, only this kind of subprocesses (minimum bias events) occurs.

A typical cross section calculation for a process $p + p \rightarrow F + X$, where F is the final state of interest and X is anything else, can be carried out by using the QCD factorization theorem. According to it, the total cross section can be written as:

$$\sigma_{p+p \rightarrow F+X} = \sum_{a,b} \int_0^1 dx_1 \int_0^1 dx_2 f_{a \backslash p_1}(x_1, \mu_F^2) f_{b \backslash p_2}(x_2, \mu_F^2) \hat{\sigma}_{a+b \rightarrow F}(\mu_F^2, \mu_R^2)$$

$$(1.9)$$

where:

- The sum is over all the initial state partons a and b that generate F;

- $f_{a\backslash p_1}(x_1, \mu_F^2)$ and $f_{a\backslash p_2}(x_2, \mu_F^2)$ are the probability densities for partons a and b to be found respectively within the protons p_1 and p_2 with a certain fraction of the proton momentum;

- μ_R is the renormalization scale, a parameter introduced in pQCD to treat the ultraviolet divergences;

- μ_F is the factorization scale, an arbitrary parameter that represents the energy scale at which the hard interaction and the non-perturbative evolution of partons occurs;

- $\hat{\sigma}_{p_1+p_2 \to F}(\mu_F^2, \mu_R^2)$ is the partonic hard scattering cross section for the process $p_1 + p_2 \to F$ and is evaluated using pQCD.

1.2.1 Hadron collider kinematics

The available energy for the creation of new particles in hard scattering processes is $\sqrt{\hat{s}} = \sqrt{x_1 x_2 s}$, where x_1 and x_2 are the four-momentum fractions carried by the interacting partons. Since in general $x_1 \neq x_2$, the center of mass frame of the two partons is boosted along the beam axis with respect to the laboratory system (i.e. the center of mass frame of the incoming protons). Therefore, it is useful to define variables which are invariant under Lorentz transformation along that direction. A convenient set of kinematic variables is given by:

$$p_T = \sqrt{p_x^2 + p_y^2} \tag{1.10}$$

$$y = \frac{1}{2}\ln\left(\frac{E + p_z}{E - p_z}\right) \tag{1.11}$$

By choosing the beam direction as the z axis of the coordinate system, the four-momentum of a particle with mass m can be parametrized in the following way:

$$p^\mu = (E, p_x, p_y, p_z) = (E_T \cosh y, p_T \sin\phi, p_T \cos\phi, E_T \sinh y) \tag{1.12}$$

where p_x, p_y and p_z are the cartesian components of the particle spatial momentum $\vec{p}$, ϕ is the azimuthal angle on the $x - y$ plane, which is a Lorentz scalar, and $E_T = \sqrt{m^2 + p_T^2}$.

The rapidity y is not invariant under Lorentz boost along the beam direction, but it transforms according to the law:

$$y \longrightarrow y + \frac{1}{2}\ln(\frac{1+\beta}{1-\beta}) \tag{1.13}$$

where β is the boost velocity. Then, rapidity differences are constant under this kind of Lorentz transformation. Experimentally, it is usually preferred to define the pseudorapidity $\eta = -\ln\tan(\frac{\theta}{2})$, where θ is the polar angle between the particle momentum and the beam direction and it can be directly measured. For ultra-relativistic particles $y \approx \eta$.

Another important variable used to describe the kinematics of a given final state is the missing transverse energy p_T^{miss}. The missing transverse energy is defined as the modulus of the missing transverse momentum $\vec{p}_T^{\mathrm{miss}}$, which is the negative sum of transverse momenta of all reconstructed particle:

$$p_T^{\mathrm{miss}} = |\vec{p}_T^{\mathrm{miss}}| = |-\sum_i \vec{p}_i| \tag{1.14}$$

Since the transverse momentum of the initial state is null, p_T^{miss} distributions are appropriate to study processes that involve the production of weakly interacting particles, such as neutrinos or exotic particles, because they escape from the detectors and their momentum is not reconstructed.

A measure of the angular separation between particles produced in hadron collisions is given by:

$$\Delta\mathrm{R} = \sqrt{\Delta\eta^2 + \Delta\phi^2} \tag{1.15}$$

where $\Delta\eta$ and $\Delta\phi$ are the separations in the η and ϕ coordinates respectively.

1.2.2   Hadronization

Color confinement is the origin of the hadronization mechanism: quarks and gluons produced after a strong scattering process recombine with each other to form hadrons clustered in jets, i.e. collimated group of colorless objects. Jets are composed by hadrons whose energy may range down to values where the pQCD approach fails. In particular, divergent cross sections may arise from pQCD calculations in the limit where the emission of a colored particle occurs either at low momentum (infrared divergence) or at low angle (collinear divergence).

To account for that, it is important to define experimental observables not sensitive to configurations that are difficult to compute theoretically, so that a comparison between data and predictions could be meaningfully done.

As a consequence, any observable $\mathcal{O}$ dependent on the momenta of the jet's particles must satisfy:

- Infrared safe condition: $\mathcal{O}(p_1, ..., p_N) \equiv \mathcal{O}(p_1, ..., p_N, \epsilon)$, where ϵ is the energy of another emitted particle, chosen arbitrarily small;

- Collinear safe condition: $\mathcal{O}(p_1, ..., p_i, ..., p_N) \equiv \mathcal{O}(p_1, ..., p_{i_1}, p_{i_2}, ..., p_N)$, where $p_i = p_{i_1} + p_{i_2}$ and p_{i_1}, p_{i_2} are the momenta of particles emitted at low angle.

For instance, in the CMS experiment, the anti-k_t recursive algorithm [14] is used to group neutral and charged hadron candidates into jets, and it satisfies the above conditions. A more detailed description of jets reconstruction techniques is given in Sec. 3.5.

1.3   VBS phenomenology

The VBS process occurs when quark constituents of colliding protons emit two vector bosons, which further interact among themselves and in turn produce two vector bosons in the final state, as depicted in Fig. 1.4, where the gray blob represents all possible terms that contribute to the overall amplitude.
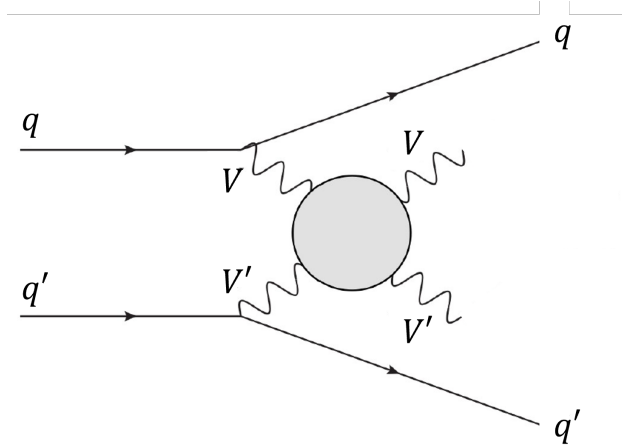

Figure 1.4: Generic VBS diagram at the LHC, the gray blob represents a generic interaction between V and V$'$, that can be either W, Z or γ bosons.

Being a purely EW mechanism, leading order diagrams are of the order $O(\alpha^4)$, where α is the EW coupling costant - $O(\alpha^6)$ when considering subsequent massive vector bosons decays. This makes VBS processes extremely

rare, as their cross sections typically range from about 1 fb to 1 pb, depending on the considered final state. Among all possible amplitudes for the EW production of diboson processes, contributions where the two vector bosons do not interact with each other are also present, and they cannot be neglected, as this would violate the lagrangian gauge invariance.

As far as only leptons are selected from W or Z bosons decays, cross sections are lower (tenths of fb), but the channel can be reconstructed with more precision; on the other hand, hadronic decays from massive gauge bosons are enhanced, but have an overwhelming contamination from QCD events.

At the LHC, VBS always manifests in association with two jets, which are the result of the hadronization of the two incoming partons. Such jets are often referred to as "VBS jets", because their kinematics is one of the distinctive signature used to tag and reconstruct VBS events. Indeed, because there are no α_s couplings at the lowest order in the matrix element calculation, and quark lines are not color-connected, VBS jets are expected to be emitted in the forward-backward region of the detector, i.e., at high absolute values of η, with little or none hadronic activity between them. Eventually, they result having large pseudorapidity gap ($|\Delta\eta_{jj}|$) and invariant mass (m_{jj}), and these observables are exploited to select potential signal candidates among reconstructed events.

The aim of this work is to measure the EW W^+W^- production by selecting events with at least two jets and where each W boson decays into a light lepton, i.e., either an electron or a muon, plus its associated neutrino. This channel ensures a relatively low background contamination, if compared to hadronic or semi-leptonic final states, and an excellent identification efficiency, since the CMS detector is particularly suitable for the reconstruction of charged leptons.

With the ever increasing amount of data collected by the LHC since the Higgs boson discovery in 2012 [8–10], a new era of precision measurements in the realm of EW interactions has started. Among those, VBS plays a key role in understanding the spontaneous symmetry breaking mechanism of the SM, and therefore on how the Higgs boson interacts with other massive gauge bosons. In fact, from a theoretical perspective, the presence of a Higgs boson with mass equal to 125 GeV is what prevents the violation of unitarity in VBS amplitudes [15]. This can be well understood by considering the scattering among longitudinally polarized massive vector bosons without accounting for the Higgs particle. In this scenario, the cross section would increase with the square of the center-of-mass energy of the system, leading to non-physical results in the high energy limit. Adding a particle with the properties of the Higgs boson introduces new amplitudes which interfere with divergent terms, thus providing a finite cross section for VBS processes all over the

energy spectrum. However, because of these delicate cancellations, any little deviation from SM predictions could end up in a dramatic modification of such a curve [16], as illustrated in Fig. 1.5. Since VBS processes are inherently bound to the interplay between the Higgs boson and massive gauge bosons, these mechanisms are also ideal to search for evidence of new physics that might enter the EW sector of the SM.
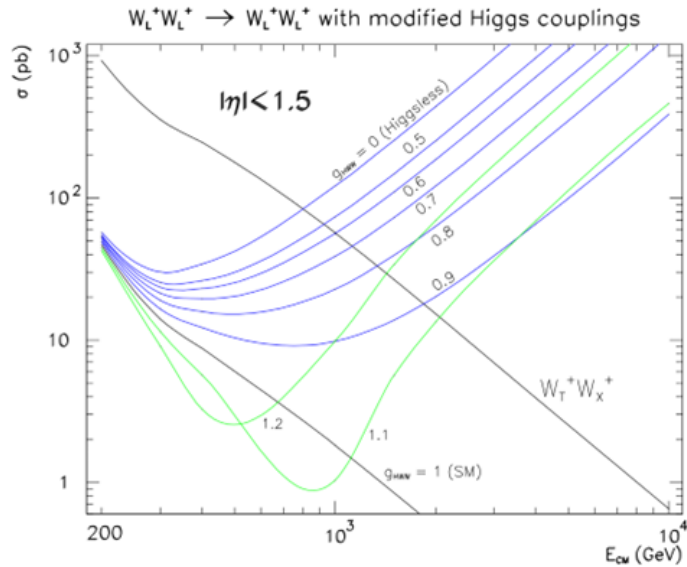
Figure 1.5: Scattering cross section of longitudinally polarized W bosons as a function of the center of mass energy for different values of the Higgs boson coupling to W bosons.

1.4   State of the art

The first observation of a VBS process was performed in the $W^{\pm}W^{\pm}$ channel [17, 18] by the ATLAS and CMS collaborations at the LHC, with data collected in 2016 and focusing on the leptonic decays of W bosons. In fact, this channel - often referred as the "golden" channel of VBS processes - has the great advantage of being scarcely contaminated from background processes, if compared to different EW diboson production mechanisms. Indeed, after applying all kinematic selections, the expected number of signal events, as shown in Table 1.3 from the measurement by the CMS collaboration, is of the same order as the number of total background events. In particular, the QCD-induced $W^{\pm}W^{\pm}$ production is significantly subdominant with respect to the EW contribution, unlike other VBS modes. The largest amount of

background events comes from non-prompt leptons, i.e., leptons originating from decays of heavy hadrons or jets misidentified with leptons, followed by WZ bosons production.

Data	201
Signal + total bkg.	205 ± 13
Signal	66.9 ± 2.4
Total bkg.	138 ± 13
Nonprompt	88 ± 13
WZ	25.1 ± 1.1
QCD WW	4.8 ± 0.4
$W\gamma$	8.3 ± 1.6
Triboson	5.8 ± 0.8
Wrong sign	5.2 ± 1.1

Table 1.3: Estimated signal and background yields after the selection. The statistical and systematic uncertainties are added in quadrature. The processes contributing to less than 1% of the total background are not listed, but included in the total background yield. Table taken from the VBS $W^{\pm}W^{\pm}$ analysis by the CMS collaboration [17].

Because estimating the WZ background in the $W^{\pm}W^{\pm}$ channel is equivalent to measuring its VBS EW production, the CMS collaboration has also exploited the full Run 2 data of the LHC to simultaneously fit these two processes [19] to data. Both $W^{\pm}W^{\pm}$ and WZ EW productions are treated as independent signals and measured differentially in several observables, such as the invariant mass of VBS jets shown in Fig 1.6. The ATLAS collaboration has measured the EW WZ production in a dedicated analysis [20].

One of the main factor limiting the sensitivity to the signal in VBS analyses is the finite size of data samples. This aspect is even more evident in a recent measurement [21] by the CMS collaboration, which still targets the EW $W^{\pm}W^{\pm}$ production in the leptonic final state, but with the goal of determining the polarization components of the two W bosons. In fact, if one considers the impact of each uncertainty source affecting the cross section measurement of polarized $W^{\pm}W^{\pm}$ boson pairs, the statistical contribution almost coincides with the total uncertainty, as it can be noticed in Table 1.4. This observation holds regardless of the combination of polarization states of the two W bosons (L = longitudinal, T = transverse, X = either of L, T).

Cross section measurements in the $W^{\pm}W^{\pm}$ channel have also allowed to put stringent limits on various extensions of the SM which predict alternative couplings between vector bosons, such as models that forsee the production
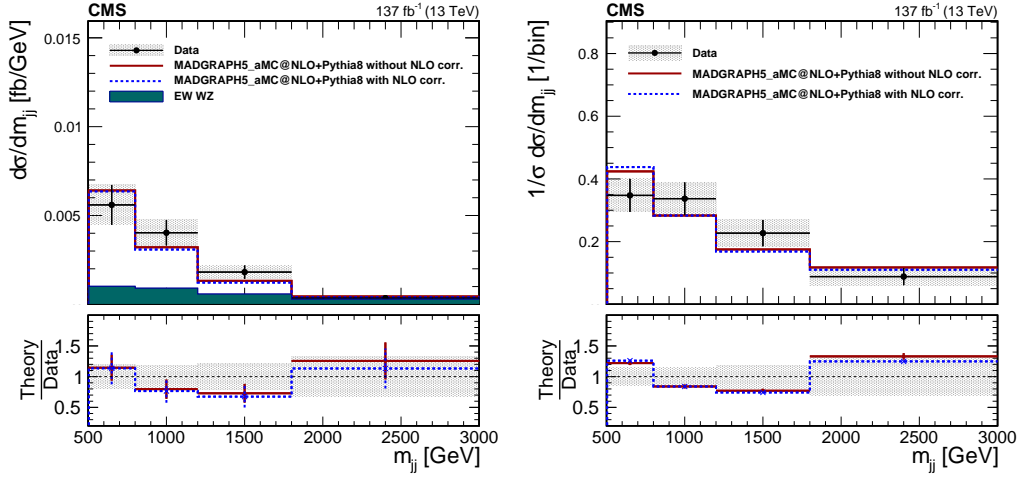
Figure 1.6: The measured absolute (left) and normalized (right) WZ cross section measurements in bins of m_{jj}. The ratios of the predictions to the data are also shown. The measurements are compared with the predictions from MADGRAPH5_aMC@NLO at LO. The shaded bands around the data points correspond to the measurement uncertainty. The error bars around the predictions correspond to the combined statistical, PDF, and scale uncertainties. Predictions with applying the $\mathcal{O}(\alpha_S \alpha^6)$ and $\mathcal{O}(\alpha^7)$ corrections to the MADGRAPH5_aMC@NLO LO cross sections, as described in the text, are shown (dashed blue). The MADGRAPH5_aMC@NLO predictions in the EW total cross sections are also shown (dark cyan). Plots taken from the VBS WZ analysis by the CMS collaboration [19].

Source of uncertainty	$W_L^\pm W_L^\pm$ (%)	$W_X^\pm W_T^\pm$ (%)	$W_X^\pm W_L^\pm$ (%)	$W_T^\pm W_T^\pm$ (%)
Integrated luminosity	3.2	1.8	1.9	1.8
Lepton measurement	3.6	1.9	2.5	1.8
Jet energy scale and resolution	11	2.9	2.5	1.1
Pileup	0.9	0.1	1.0	0.3
b tagging	1.1	1.2	1.4	1.1
Nonprompt lepton rate	17	2.7	9.3	1.6
Trigger	1.9	1.1	1.6	0.9
Limited sample size	38	3.9	14	5.7
Theory	6.8	2.3	4.0	2.3
Total systematic uncertainty	44	6.6	18	7.0
Statistical uncertainty	123	15	42	22
Total uncertainty	130	16	46	23

Table 1.4: Systematic uncertainties of the $W_L^\pm W_L^\pm$ and $W_X^\pm W_T^\pm$, and $W_X^\pm W_L^\pm$ and $W_T^\pm W_T^\pm$ cross section measurements in units of percent. Table taken from the polarized VBS $W^\pm W^\pm$ analysis by the CMS collaboration [21].

of doubly-charged Higgs bosons [22].

Among recent results in the context of VBS mechanisms, the CMS collaboration has claimed the evidence for the EW ZZ production in the fully leptonic final state, using the entire Run 2 data set [23]. Despite the clean experimental signature of the signal, its low cross section makes this process the rarest EW diboson production, and it is therefore necessary to employ multivariate techniques to suppress the background contamination. The ATLAS collaboration has also adopted a similar approach, but they were able to made the observation of this VBS channel by also including the $ZZ \to \ell^+\ell^-\nu\nu$ decay mode [24], as shown in Fig. 1.7.

Noticeable results with data from pp collisions at $\sqrt{s} = 13$ TeV were also published for the EW production of a W (or Z) boson plus a γ photon [25–28] and for the EW diboson production in semi-leptonic final states [29, 30], which have to cope with the challenging QCD background entering the signal selection. In this vast panorama of VBS measurements, the W^+W^- mode has never been observed so far, although it is deeemed a key mechanism to complete the picture of the EW sector of the SM. The reasons for this are several: conversely to other channels, partial Run 2 data had no enough statistical power to reach a good sensitivity to this rare process, therefore this measurement has not been attempted until the entire Run 2 data set was collected. Moreover, even though the leptonic final state is relatively clean, the presence of two neutrinos forbids the reconstruction of the whole event kinematic. Last but not the least, the main limitation is given by the production of top-antitop quarks pair, which only affects the W^+W^- channel
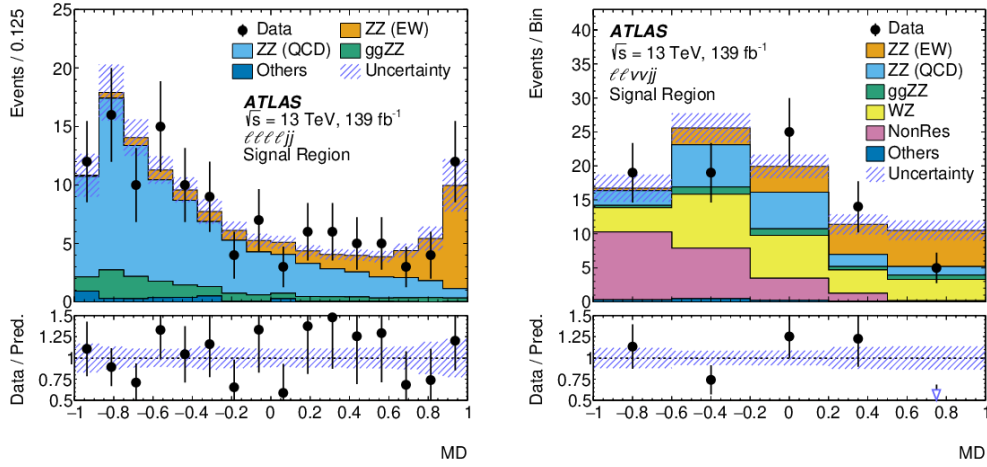
Figure 1.7: Distributions of the multivariate discrimimant (MD) after the statistical fit in the $\ell\ell\ell\ell jj$ (left) and $\ell\ell\nu\nu jj$ signal regions. Plots taken from the VBS ZZ analysis by the ATLAS collaboration [24].

and represents the dominant background of the analysis, because of its large cross section.

In this work, I present the first observation of the EW W^+W^- process in the leptonic final state, discussing the background reduction strategy and signal candidate selection we devised to perform the cross section measurement. Results are based on the full Run 2 data set collected by the CMS experiment from 2016 to 2018, which corresponds to an integrated luminosity of 138 fb^{-1}.

Chapter 2

The CMS experiment at the LHC

In this Chapter, the LHC apparatus is presented in Sec. 2.1, whereas the CMS experiment and the features of its subdetectors are discussed in detail in Sec. 2.2.

2.1   The Large Hadron Collider

The Large Hadron Collider (LHC) [31] is installed in the underground tunnel that has been hosting the Large Electron Positron Collider (LEP) until 2001. LHC extends for 27 km in circumference along the French-Swiss border and it is designed to accelerate and collide protons (or heavy ions) up to an energy of 7 TeV, which corresponds to 14 TeV (2.76 TeV per nucleon) in the center of mass system. Before entering the LHC beam pipe, the protons are accelerated in various steps via an accelerator complex shown in Fig. 2.1.

After being created through ionization of gaseous hydrogen, protons are sent to LINAC2, a linear accelerator that generates a 50 MeV collimated beam using radio frequency quadrupoles. The beam is delivered to a chain of two different synchrotrons (the Proton Synchrotron Booster (PSB) and the Proton Synchrotron (PS)) whose combined action groups the protons in packets with a frequency of 40 MHz and an energy of 25 GeV. Then, the bunches are accelerated up to 450 GeV by the Super Proton Synchrotron (SPS) and finally injected into LHC through two different beam pipes, where they flow in opposite directions, further accelerated by radio frequency cavities. Once the maximum energy is reached, they may collide in four interaction points, where the experiments are located and beam pipes intersecate in a common vacuum chamber:
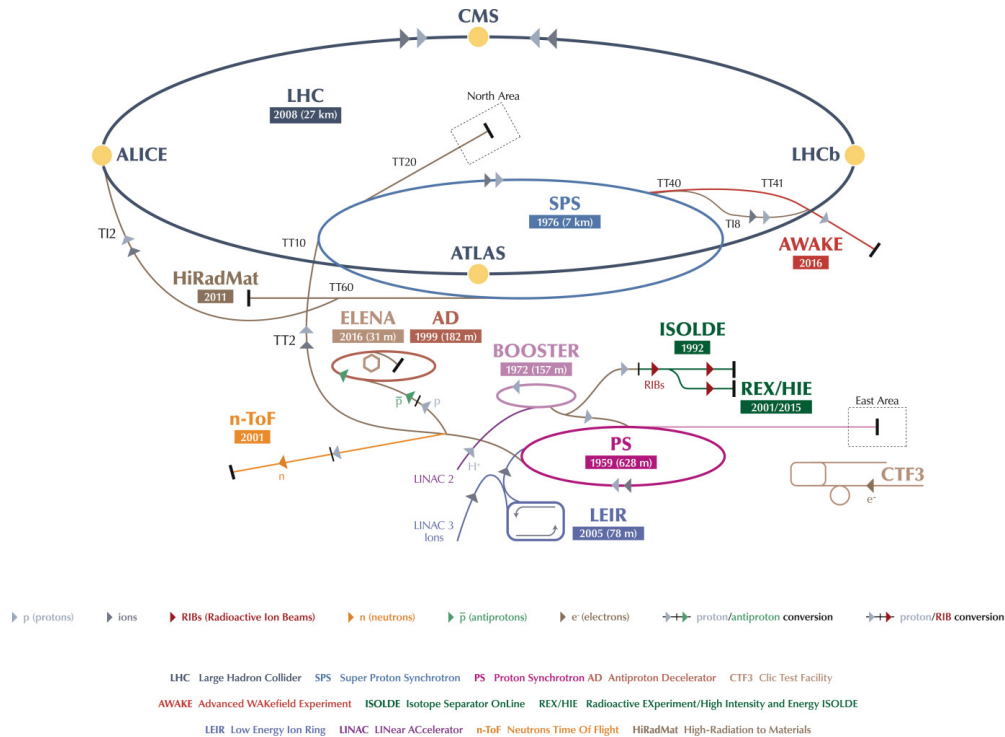
Figure 2.1: LHC accelerator scheme.

- **ATLAS** (A Toroidal LHC ApparatuS) [32] and **CMS** (Compact Muon Solenoid) [33] are multi-purpose detectors, designed to investigate a wide range of physics phenomena. Their main objective was to find the experimental evidence that could prove or exclude the existence of the Higgs boson. In 2012 they announced the discovery of a particle compatible with the predicted Higgs boson and nowadays they focus on the study of its properties as well as on the search of new physics beyond the SM. The presence of two independent detectors pursuing the same goals is fundamental to cross-check the results;

- **LHCb** (LHC-b) [34] is designed to study CP violation in electroweak interaction and the matter-antimatter asymmetry through the analysis of rare decays of hadrons containing the b quark;

- **ALICE** (A Large Ion Collider Experiment) [35] is a detector devoted to the study of quark-gluon plasma in heavy ion collisions.

Protons need to be kept along the circular trajectory described by the LHC ring, therefore the presence of a magnetic system is required. Over

1200 magnets are placed along the accelerator, with their field oriented orthogonally with respect to the ring. For a particle with unitary charge it can be shown that:

$$p[\text{GeV}] = 0.3B[\text{T}]R[\text{m}] \tag{2.1}$$

where p is the particle momentum, B is the magnetic field and R is the radius of the orbit. Since LHC is designed to collide beams of protons, two separate beam pipes have to be installed: same-charged particles travelling in opposite ways need two magnetic fields with equal intensities but opposite orientations in order to obtain the same deflection.

The average magnetic field required to keep protons in motion along a circumference of 27 km is about 5.5 T. However, since LHC is made of both circular and rectilinear sections, the magnets have to produce a 8 T magnetic field along the beam pipes (see Fig. 2.2). The needed currents are provided by dipoles that operate in superconductive regime: at LHC, this condition is reached when dipoles are cooled down to ~ 2 K. Furthermore, over 8000 auxiliary magnets among quadrupoles, sextupoles and octupoles are used to correct and adjust the beam orbit.
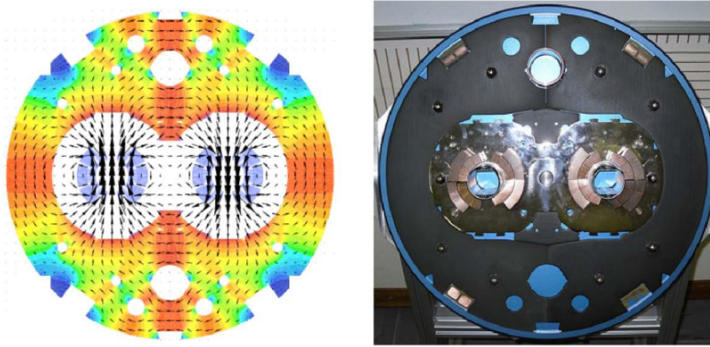
Figure 2.2: On the left: Lines of the magnetic field; on the right: Transversal section of the LHC beam pipe.

One of the most important parameter for a particle accelerator is the instantaneous luminosity $\mathcal{L}$, which is defined by the following equation:

$$N = \sigma\mathcal{L} \tag{2.2}$$

where N is the rate of events for a given process and σ is its expected cross section.

The LHC design instantaneous luminosity is $\mathcal{L} = 10^{34}$ cm^{-2}s^{-1} and, taking into account a total inelastic cross section of about 100 mb, corresponds

roughly to 10^9 proton interactions per second. In terms of the accelerator characteristics, $\mathcal{L}$ can be approximately expressed as:

$$\mathcal{L} = f \frac{n_1 n_2}{4\pi \sigma_x \sigma_y} \qquad (2.3)$$

The two bunches collide at a frequency $f = 40$ MHz, which corresponds to a 25 ns temporal displacement between two successive bunch crossings; n_1 and n_2 are the number of protons within the two bunches, while σ_x and σ_y give a measure of the packet sizes in the plane perpendicular to the beam axis. The integrated luminosity is defined as the time integral of the instantaneous luminosity and it quantifies the size of a dataset:

$$L = \int \mathcal{L} dt \qquad (2.4)$$

Due to the LHC high instantaneous luminosity, the probability of multiple pp interactions per single bunch crossing must be taken into account.
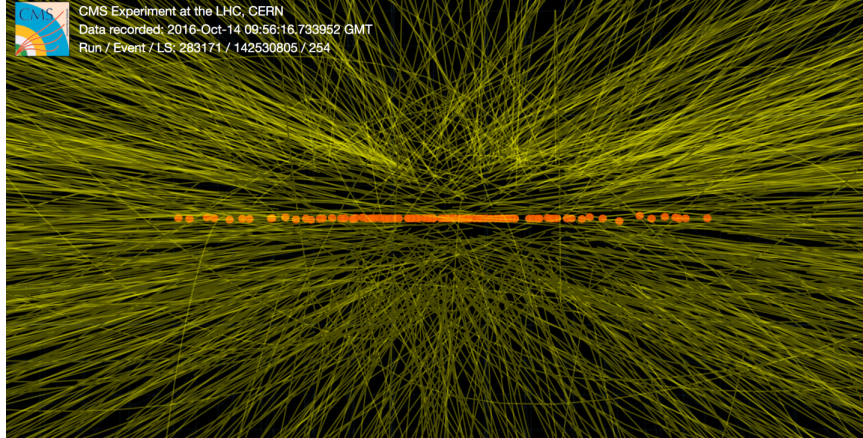
Figure 2.3: Pile up collisions reconstructed by the CMS detectors.

In pp collisions, about 10^9 inelastic interactions per second occur but, since the bunch crossing rate is fixed to $f = 40$ MHz, significantly more than one interaction vertex per bunch crossing is expected. Thus, the total number of pileup events is calculated as:

$$PU = \frac{inelastic\ events\ per\ second}{f} \sim 25$$

However, since we are dealing with rare processes, the creation of more than one interesting vertex per bunch crossing is absolutely negligible. Therefore, LHC detectors must perform good vertices reconstruction in order to reduce pileup contributions, as shown Fig. 2.3.

2.2   The CMS experiment

The Compact Muon Solenoid (CMS) apparatus [33] is a general purpose detector installed around one of the four interaction points in the LHC tunnel, in a 100 m underground cavern close to the village of Cessy, in France. The design of CMS is well suited to investigate the nature of the electroweak symmetry breaking mechanism and the properties of short-scale interactions. Furthermore, it allows to test SM predictions and to search for new physics in the TeV regime.

To achieve these goals, CMS detectors need to be able to accurately reconstruct the final state produced after a pp collision. As the name suggests, the main features of the experiment are:

- The compactness of the detector, for its weight is around 14000 tons while being 28.7 m long with a diameter of 15 m;

- The optimal performance in muon detection;

- A superconducting solenoidal magnet.

CMS has a cylindrical structure made up by several coaxial detecting layers placed around the beam direction (barrel region) and closed at both ends (endcap region) by detecting disks in order to make the apparatus as hermetic as possible. The coordinate system adopted by the CMS collaboration and used throughout this thesis, as shown Fig. 2.4, has the origin fixed in the nominal collision point inside the experiment; the x-axis is oriented radially inward toward the center of LHC, the y-axis points vertically upward and the z-axis coincides with the beam direction, such to form a right-handed cartesian system.

The azimuthal angle ϕ is measured from the x-axis in the x-y plane (or transverse plane), in which the radial coordinate is denoted by r, while the polar angle θ is evaluated from the z-axis.

Schematically, from the inner region outwards, the various CMS components are:

- **The silicon tracker** ($r < 1.2$, $|\eta| < 2.5$): it consists of an inner silicon pixel vertex detector and a surrounding silicon microstrip detector, with a total active area of about 215 m^2. It is used to reconstruct charged particle tracks and vertices;

- **The electromagnetic calorimeter ECAL** ($1.2\,\text{m} < r < 1.8\,\text{m}$, $|\eta| < 3$): it consists of many lead tungstate (PbWO$_4$) scintillating crystals and it measures the trajectory and the energy released by photons and electrons through electromagnetic showers;
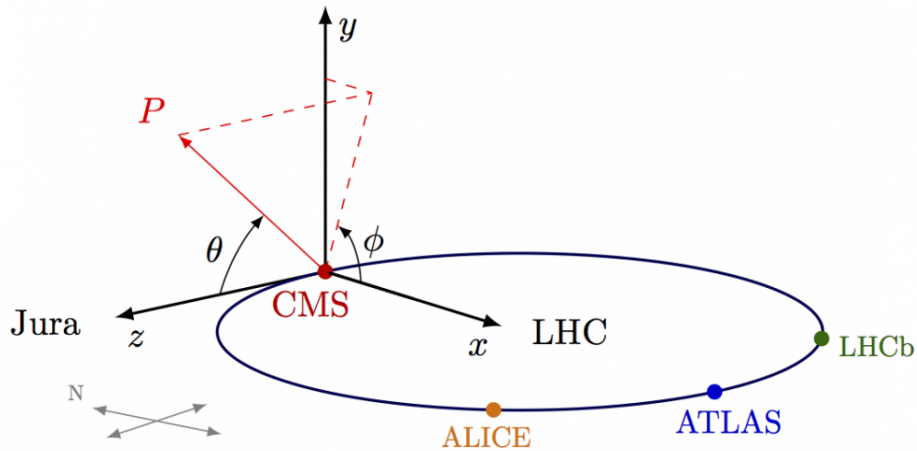
Figure 2.4: CMS coordinate system.

- **The hadronic calorimeter HCAL** (1.8 m $< r <$ 2.9 m, $|\eta| < 5$): it is a sampling calorimeter with brass absorbers and plastic scintillators as active elements. It is used to measure the direction and the energy deposited by hadrons produced after the collision;

- **The superconducting solenoidal magnet** (2.9 m $< r <$ 3.8 m, $|\eta| < 1.5$): it is a superconducting solenoid that produces a uniform magnetic field of 3.8 T in the internal region along the z-axis. The field lines are closed with an iron yoke that holds a residual magnetic field of 1.8 T pointing along the opposite direction with respect to the internal field.

- **The muon system** (4 m $< r <$ 7.4 m, $|\eta| < 2.4$): it is a composite system made of Drift Tubes (DT) in the barrel region, Cathode Strip Chambers (CSC) in the endcaps and Resistive Plate Chambers (RPC) located in both regions. These detectors are located inside the iron structure of the return yoke and are dedicated to muon identification and momentum measurement.

The CMS detectors, shown in Fig. 2.5, are specifically designed to achieve good performances in the following tasks:

- Muon identification and momentum resolution over a wide range of momenta and angles (muon system and silicon tracker);

- Charged-particle momentum resolution and reconstruction efficiency (inner tracker);

CMS DETECTOR
Total weight   : 14,000 tonnes
Overall diameter : 15.0 m
Overall length   : 28.7 m
Magnetic field   : 3.8 T

STEEL RETURN YOKE
12,500 tonnes

SILICON TRACKERS
Pixel (100x150 μm) ~16m² ~66M channels
Microstrips (80x180 μm) ~200m² ~9.6M channels

SUPERCONDUCTING SOLENOID
Niobium titanium coil carrying ~18,000A

MUON CHAMBERS
Barrel: 250 Drift Tube, 480 Resistive Plate Chambers
Endcaps: 468 Cathode Strip, 432 Resistive Plate Chambers

PRESHOWER
Silicon strips ~16m² ~137,000 channels

FORWARD CALORIMETER
Steel + Quartz fibres ~2,000 Channels

CRYSTAL
ELECTROMAGNETIC
CALORIMETER (ECAL)
~76,000 scintillating PbWO₄ crystals

HADRON CALORIMETER (HCAL)
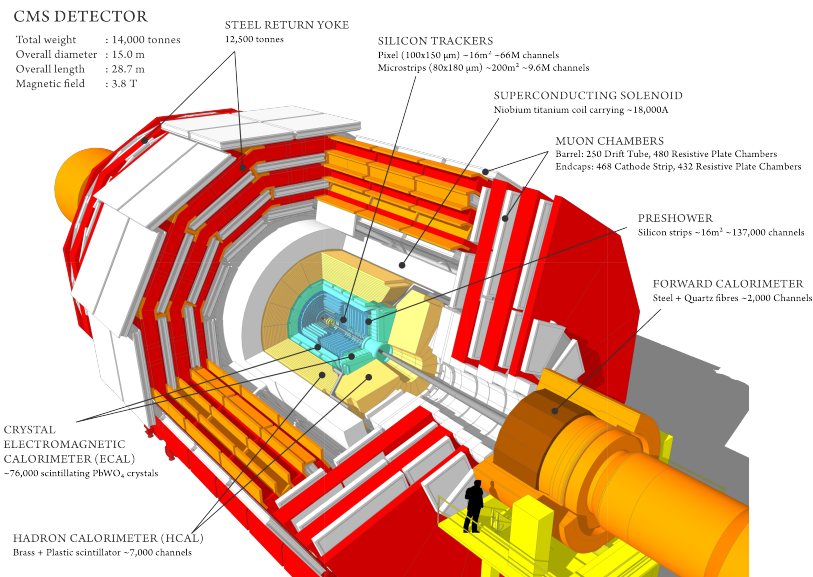Brass + Plastic scintillator ~7,000 channels

Figure 2.5: Schematic view of the CMS experiment.

- Missing transverse energy and jet-momentum resolution (silicon tracker and both electromagnetic and hadron calorimeters).

More details of the various sub-detectors are examined in the following sections.

2.2.1   The superconducting solenoidal magnet

The CMS magnet produces a uniform magnetic field of 3.8 T within the solenoid, which has a diameter of 6 m and is 12.8 m long. The distinctive features of the solenoid are the four Niobium-Titanium coils: due to the extremely high current required, they need to be cooled down to 4 K in order to show superconductor properties. In this regime, the energy stored in the magnet is about 2.6 GJ at full current ($\sim$ 19 kA). The magnet return yoke consists of three sections along the z-axis holding the muon chambers in the gaps and the field is about 1.8 T.

The presence of the solenoid is essential for the detection of charged particles because they are deflected by the magnetic field. Indeed, it is possible to measure the momentum of these particles by measuring the curvature of their trajectories through the tracking system, according to equation (2.1).
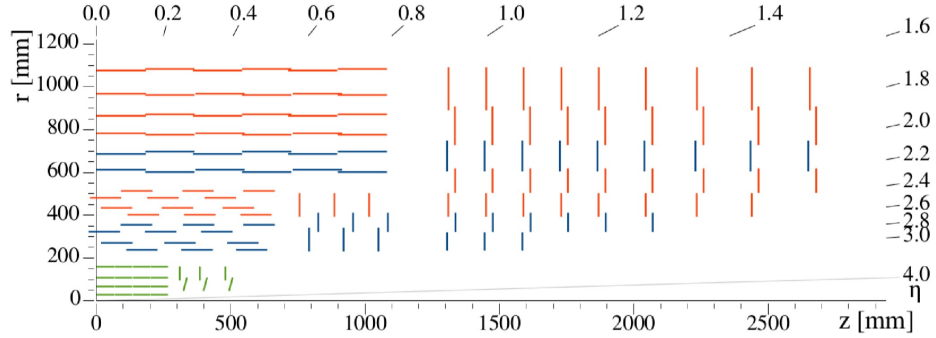
Figure 2.6: Pictorial view of a tracker slice in the $r - z$ plane.

2.2.2   The silicon tracker

The silicon tracker is the detector closest to the beams' collision point and is immersed in the 3.8 T magnetic field generated by the superconducting solenoid. Its goal is to identify the trajectories (or tracks) of charged particles originating either from primary (PV) or secondary vertices (SV), to ensure an optimal event reconstruction. SVs can be found up to a few hundreds of μm away from PVs if produced by long-lived particles, such as hadrons containing a b quark (b-hardons) or τ leptons. As a matter of fact, in order to reconstruct these particles, locating the position of secondary vertices with high precision is among the tracker's main tasks. This is achieved by measuring the impact parameter d, which is the minimum distance between a track and the PV. Vertex identification allows to distinguish particles either coming from pileup events or secondary vertices, and it is ensured by the tracker good spatial resolution, as shown Fig. 2.7 for the impact parameter.

In order to achieve optimal performances, the detector needs to have high granularity and redundancy of measured points (or hits). These are crucial requirements to avoid ambiguity on the assignment of the hits to a given track and to suppress combinatorial background due to the presence of multiple collisions, since, at the nominal instantaneous luminosity of operation, an average of 25 pileup events per bunch crossing are expected.

Another key aspect for the measurement optimization is to keep the amount of material in the tracker as low as possible. This condition is strictly necessary to reduce particle multiple scattering that could compromise the tracker accuracy for low p_{T} values. Indeed, the momentum resolution for a magnetic spectrometer is given by two contributions:

$$\frac{\sigma_{p_{\text{T}}}}{p_{\text{T}}} = \frac{a * p_{\text{T}}}{B} \oplus b \tag{2.5}$$

where a, b are two parameters depending on the tracker geometry and ma-
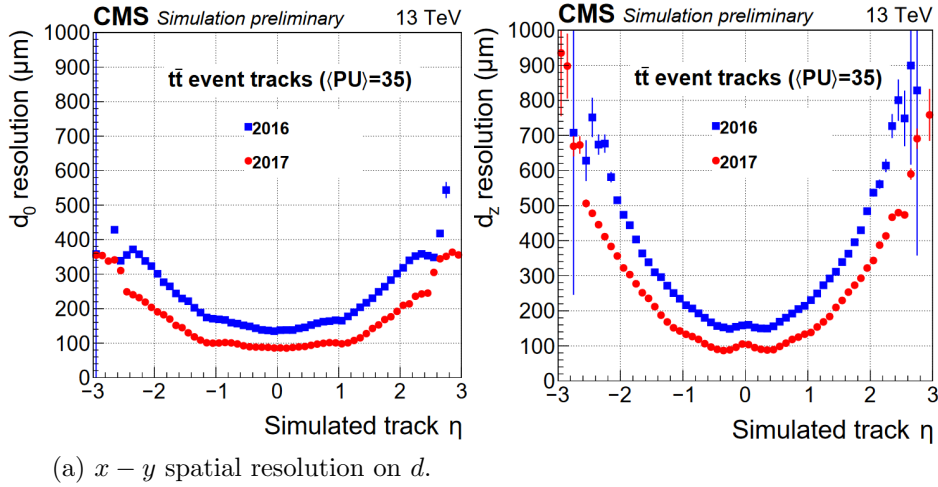
(a) $x - y$ spatial resolution on d.

Figure 2.7: Spatial resolution on the reconstruction of d as a function of η. On the left: $x - y$ spatial resolution; on the right: z spatial resolution. The tracker achieves better performance in 2017 because an extra silicon layer was added; in the central region the spatial resolution goes down to about 100 μm.

terial and B is the magnetic field. The linear term spoils the momentum resolution in the high energy regime, while the constant one is due to multiple scattering and dominates at low p_{T} scale. Furthermore, the lower the tracker's material, the lower is the probability for a photon to interact with the silicon and create an electron-positron pair: this mechanism negatively affect photon reconstruction in the calorimeter.

The silicon pixel detector is the innermost device and it has a fundamental role for the reconstruction of primary and secondary vertices. Due to its proximity to the collision point, it must have both high pixel multiplicity and radiation resistance. It covers the pseudorapidity range $|\eta| < 2.5$ and it consists of four cylindrical layers 53 cm long located at $r = 4.4$ cm, 7.3 cm, 10.2 cm and 16.0 cm, and three pairs of endcap disks placed at $z = \pm\ 34.5,\ \pm\ 46.5$ cm and $\pm\ 51.6$ cm. The detector is composed by 1856 modules and, to ensure the granularity requested, each of them contains a highly segmented silicon sensor (124 million pixels in total) with a thickness of 280 μm. The pixel cell area is $100\ \times\ 150\ \mu$m^2 and the achievable hit reconstruction resolution is about 10 μm in the barrel region and 15 μm in the endcaps.

The microstrip tracker is 540 cm long and it extends around the pixel detector up to $r = 110$ cm. It consists of 15148 silicon modules, covering an area of about 198 m^2 with a total of 9.3 million strips. The microstrip

detector is further divided in four sections, two in the barrel region and two in the endcaps:

- **Tracker Inner Barrel TIB**: 20 cm $< r <$ 55 cm, $|z| <$ 65 cm, 4 cylindrical coaxial layers;

- **Tracker Outer Barrel TOB**: 55 cm $< r <$ 116 cm, $|z| <$ 110 cm, 6 cylindrical coaxial layers;

- **Tracker Inner Disks TID**: 20 cm $< r <$ 55 cm, 65 cm $< |z| <$ 110 cm, 6 disks (3 per side);

- **Tracker EndCaps TEC**: 20 cm $< r <$ 116 cm, 120 cm $< |z| <$ 280 cm, 18 disks (9 per side).

Each section is made of two kind of modules: single sided modules consist of one sensor installed onto a carbon fiber support together with the readout electronics, with the silicon strips laying along the z-axis in the barrel region and along the radial direction in the endcaps. Instead, the stereo-modules are designed with two sensors stuck together back to back and rotated of a relative angle of 100 mrad, in order to obtain the full three-dimensional information about the particle interaction point.

The sensors are realized with a n-type substrate on which $p+$ doped strips are implanted. The pitch between the strips depends on the position of the module in the detector and varies between 80 μm in the inner layers and 205 μm in the outer layers.

2.2.3   The electromagnetic calorimeter ECAL

The main goal of ECAL is to identify electrons and photons and to measure their energy with the best possible precision. Therefore, it contributes for determining the missing transverse energy. ECAL is a cylindrical homogeneous calorimeter, composed of many scintillating crystals of lead tungstate ($PbWO_4$) with truncated pyramidal shape, grouped into 5×5 matrices called towers.

$PbWO_4$ is a suitable material for the calorimeter crystals because of its many properties. For what concerns the particle detection, its high mass density ($\rho = 8.3\text{g/cm}^3$) and short radiation length[1] (X_0) allow all of the electrons and photons to be stopped within the calorimeter, while a 2.2 cm Molière radius ensure a good lateral containment of the electromagnetic shower. This is fundamental to design a compact calorimeter with high granularity.

---

[1]For electrons and photons, the radiation length X_0 is defined as the average distance at which the particle shower energy is a factor e^{-1} of the initial energy.
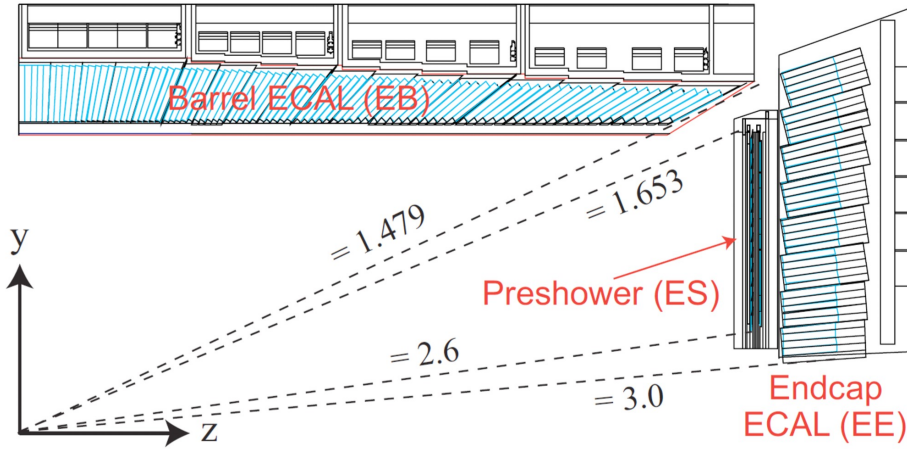
Figure 2.8: $r - z$ view of an ECAL sector.

Other advantages of this material are the radiation hardness and the fast scintillation decay time ($\simeq 10$ ns), which permits to collect about 80% of the light produced by the particle shower within the 25 ns interval between two consecutive bunch crossings. On the other hand, the major drawback of $PbWO_4$ crystals is the low light yield ($\simeq 10$ photoelectron per MeV) which, in turn, requires a signal amplification system.

As all CMS detectos, ECAL is divided into a cylindrical central part (EB) closed at both ends by two endcaps (EE). A preshower system (ES) is installed in front of the ECAL endcaps in order to separate the showers produced by a γ from those produced by forward emitted π^0. A schematic view of ECAL is shown Fig. 2.8.

The barrel covers the region up to $|\eta| < 1.479$, it extends from $r=129$ cm and it is 630 cm long. EB contains 61200 crystals with the following dimensions: the inner surface is 22×22 mm^2 , while the rear face is 26×26 mm^2 and the crystal length is 23 cm, corresponding to 25.8 X_0. The crystals are not exactly radially mounted with respect to the direction pointing to the interaction point. Instead, they are slightly tilted both in η and ϕ coordinates to prevent photons[2] from ending up in the separation zone between two adjacent crystals.

Each endcap covers the pseudorapidity range $1.479 < |\eta| < 3$ and they are both composed of 7324 crystals, whose geometrical characteristics are similar to those mentioned above: the front and the rear faces are 28.62×28.62 mm^2 and 30×30 mm^2, respectively, and they are 22 cm long (24.7

---

[2]Electrons are not influenced by the crystal disposal because their trajectory is bent by the magnetic field.

X_0).

The energy resolution is a fundamental parameter and, for a homogeneous calorimeter, it is given by three terms:

$$\left(\frac{\sigma_E}{E}\right)^2 = \left(\frac{a}{\sqrt{E}}\right)^2 + \left(\frac{b}{E}\right)^2 + c^2 \qquad (2.6)$$

where:

- $\frac{a}{\sqrt{E}}$ is the stochastic term: it dominates at low energies and it takes into account of the contributions given by the statistical fluctuations in the number of generated and collected photoelectrons;

- $\frac{b}{E}$ is the noise term: it includes the uncertainties coming from the reconstruction of pileup events and from the electrical noise, both due to the photodetector and preamplifier;

- c is the constant term: it dominates in the high energy regime and it is the parameter that includes the calorimeter imperfections and other systematic errors.

The EB resolution for electrons was measured, obtaining the following values:

$$\left(\frac{\sigma_E}{E}\right)^2 = \left(\frac{2.8\%\sqrt{\text{GeV}}}{\sqrt{E}}\right)^2 + \left(\frac{12\%\text{GeV}}{E}\right)^2 + (0.3\%)^2 \qquad (2.7)$$

where E is the energy measured in GeV. For a 60 GeV photon it turns out that the energy resolution is about 0.5%.

2.2.4   The hadronic calorimeter HCAL

The hadronic calorimeter HCAL allows to measure the energy and the direction of the hadrons produced after the pp collision. Moreover, along with ECAL, it is essential to reconstruct the energy imbalance in the transverse plane, which is a typical experimental signature of non-interacting particles such as neutrinos.

HCAL is a brass/scintillator sampling calorimeter covering the region within $|\eta| < 5$ and it is divided in four sections, as shown Fig. 2.9:

- **Barrel Hadronic Calorimeter HB**: it is radially restricted between the outer extent of ECAL and the inner part of the magnet coil, covering the pseudorapidity region $|\eta| < 1.3$;
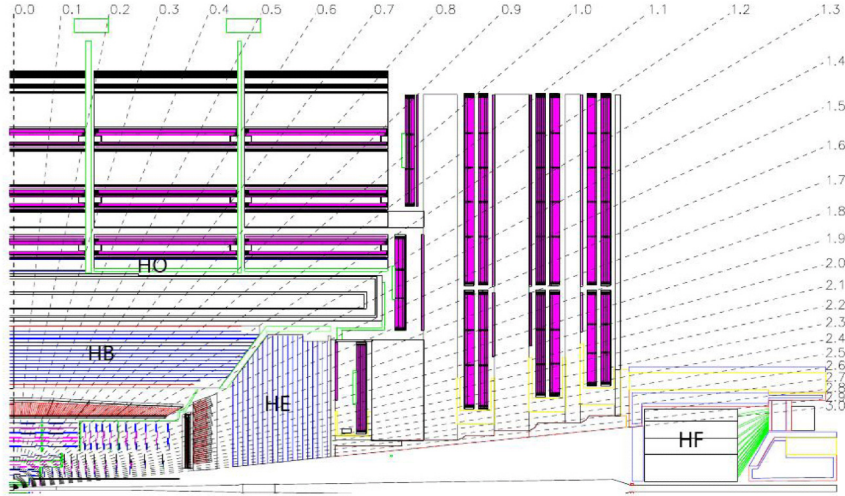
Figure 2.9: $r - z$ view of an HCAL sector.

- **Endcap Hadronic Calorimeter HE**: it covers the interval $1.3 < |\eta| < 3$ and it has the same radial constraints, as well as the same structure and geometry as HB, partially overlapping with it;

- **Outer Hadronic Calorimeter HO**: it is also known as tail catcher and it is placed outside the solenoid, complementing the barrel calorimeter;

- **Forward Hadronic Calorimeter HF**: it is a sampling calorimeter formed by two units located in the very forward region ($3 < |\eta| < 5$) outside the magnetic coil. The sampling is realized with different materials: the absorber is made of iron, while the signal is collected through quartz fibres which emit Cherenkov light with the passage of charged particles.

The light produced by the hadron shower in scintillators is collected by wavelength shifting fibres (WLS) and read-out by hybrid photodiodes and silicon photomultipliers. The calorimeter thickness varies between 7 and 11 interaction lengths[3] λ_I, depending on the η value.

The energy resolution in the different regions of HCAL can be parametrized

---

[3]The interaction length λ_I is a parameter that characterizes the transversal as well as the longitudinal shape of the hadronic shower.

using a stochastic and a constant term, as follows:

$$\left(\frac{\sigma_E}{E}\right)^2 = \left(\frac{90\%\sqrt{GeV}}{\sqrt{E}}\right)^2 + (4.5\%)^2 \qquad \text{barrel/endcap} \qquad (2.8)$$

$$\left(\frac{\sigma_E}{E}\right)^2 = \left(\frac{172\%\sqrt{GeV}}{\sqrt{E}}\right)^2 + (9\%)^2 \qquad \text{HF} \qquad (2.9)$$

2.2.5   The muon system

The muon system is one of the key element of the CMS experiment and it has three fundamental tasks: triggering, measuring charged particles' momentum and identifying muons. The last two goals are carried out along with the silicon tracker, whereas the trigger will be better discussed in Section 2.2.6.

When passing through matter, muons lose little energy and are not easily stopped; thus, the muon system is the last detection layer of CMS and it is placed outside the magnet coil, embedded in the return yoke. The system consists of three different types of gaseous particle detectors, schematically shown Fig. 2.10:
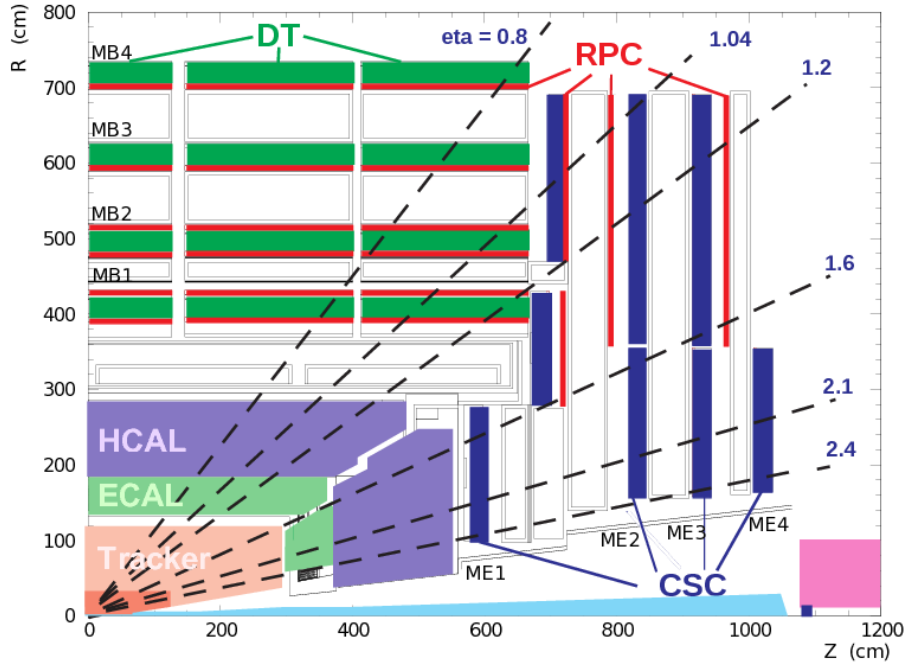

Figure 2.10: $r - z$ view the muon system.

- **Drift Tubes DT**: they are placed in the barrel region $|\eta| < 1.2$, where the particle flow is low ($< 10 \text{ Hz/m}^2$) and the magnetic field is weak. The system is organized in 5 wheels disposed along the z-axis and composed by four concentric stations, each one formed by 12 DT chambers. The basic independent element of the DT system is the superlayer, which is formed by 4 rectangular drift tube cells. Each cell is filled with a gas mixture of Ar (85%) and CO_2 (15%) and have a transverse size of $13 \times 42 \text{ mm}^2$ and a variable length from 2 m to 4 m. In each chamber two superlayers have anode wires parallel to the beam axis and one perpendicular to it, thus providing measurements of r, ϕ and z coordinates of the track hit position, with a spatial resolution of 100 μm;

- **Cathode Strip Chambers CSC**: they are employed in the endcap region $0.8 < |\eta| < 2.4$, because there, the strong and non-uniform magnetic field, combined with the high particle rate ($> 100 \text{ Hz/m}^2$) does not allow the usage of drift tube chambers. CSC are multi-wire proportional chambers filled with a gas mixture of Ar(40%), CO_2 (50%) and CF_4(10%). The cathods are segmented into strips oriented radially and transversally with respect to anodic wires, providing information about the r and ϕ track coordinates, with a spatial resolution of ~ 80 μm;

- **Resistive Plate Chambers RPC:** they are placed both in barrel and endcap regions and they are exploited as auxiliary detectors for DT and CSC systems. They cover the pseudorapidity range $|\eta| < 2.1$ and they are made of 4 bakelite planes, interspaced by a 2 mm gap filled with a gas mixture of $C_2H_2F_4$ (94.5%) and Isobutane (5.5%). RPC are not characterized by a good spatial resolution, nevertheless they provide precise time measurements for the trigger system.

2.2.6   The CMS trigger system

As previously mentioned, at LHC every 25 ns there is a bunch crossing. Since it is not possible to store and process all the data associated with such a high rate, a fast decision criteria is needed to heavily reduce the number of events per second to be saved on disk. Indeed, the speed at which data can be written on mass storage is limited and, on the other hand, hadron collisions typically involve minimum bias events, which are not interesting for most physics analyses. This goal is accomplished by the CMS trigger system, organized in two two stages: **Level 1 Trigger L1** and **High Level Trigger HLT**.

L1 is a hardware based trigger, implemented on programmable electronics, whose task is to bring the rate down to 100 kHz. It collects the information from the calorimetric towers and the muon chambers and it performs event selection within 3.2 μs from the collision. When the event passes the L1 threshold, it is sent to the data acquisition system and then processed.

HLT task is to reduce the L1 output down to a maximum rate of the order of 1 kHz. This trigger is a software system implemented in a filter farm of about one thousand commercial processors. It uses all the information coming from the subdetectors and cuts the minimum bias events using the same algorithms used for offline particle reconstruction.

In order to make a fast rejection of the useless data and, at the same time, to collect all the interesting events, HLT algorithm is split on more levels:

- **Level 2 trigger**: it takes advantage of the information provided by calorimeters and muon chambers with full granularity;

- **Level 2.5 trigger**: it adds the information from the pixel detector;

- **Level 3 trigger**: it uses the data gathered by the all the subdetector systems.

Once the event has passed the HLT selection, it is written on disk and archived in the CMS computing center at CERN, called Tier 0, where offline reconstruction is carried out.

Chapter 3

Physics objects reconstruction and identification

The CMS collaboration has developed dedicated algorithms that aim at the reconstruction and identification of what we call "physics objects". Such objects are defined from the entire collection of tracks, calorimeter deposits, muon chamber hits as recorded by the CMS detector for each pp collision, and are identified with either electrons, photons, jets, charged and neutral hadrons or muons, if they fulfill quality requirements based on measurable quantities. The technique used to reconstruct physics objects relies on the "Particle Flow" (PF) algorithm, which is described in this Chapter. Analysis-specifc selections that are applied on top of PF candidates are also discussed in the following, focusing on physics objects that characterize this work.

3.1 The Particle Flow algorithm

The PF algorithm event reconstruction technique [36] is developed and used by the CMS collaboration to reconstruct and identify stable particle on an event basis, combining and elaborating all the information collected by CMS subdetectors. These particles and their four-momenta constitute building blocks to reconstruct more complex objects and quantities such as jets, τ leptons - identified from their decay into lighter leptons or hadrons -, $p_\mathrm{T}^\mathrm{miss}$, b-jets tagger and so on.

The effectiveness of the PF algorithm relies on the performance achieved by the silicon tracker, ECAL, and the muon system: the first allows for high precision measurements of the charged particle p_T down to 150 MeV for $|\eta| <$ 2.5, thanks to its position resolution and the intense magnetic field generated by the CMS solenoid; the high granularity and energy resolution of ECAL

crystals is what ensures an accurate reconstruction of photons and electrons in such a challenging environment, whereas the muon system is responsible for the muon identification.

Indeed, the first step of the PF technique consists in the reconstruction of basic elements - charged tracks, calorimeter clusters and muon tracks - which are then linked together by a dedicated algorithm, if such raw objects are found to be spatially and kinematically compatible. Different trajectories and energy deposits of reconstructed physics objects are shown in Fig. 3.1. Whenever more elements, as recorded by CMS subdetectors, give rise to a PF candidate, they are removed from the calculation and the algorithm proceeds to the next iteration. PF candidates are identified in the following order:
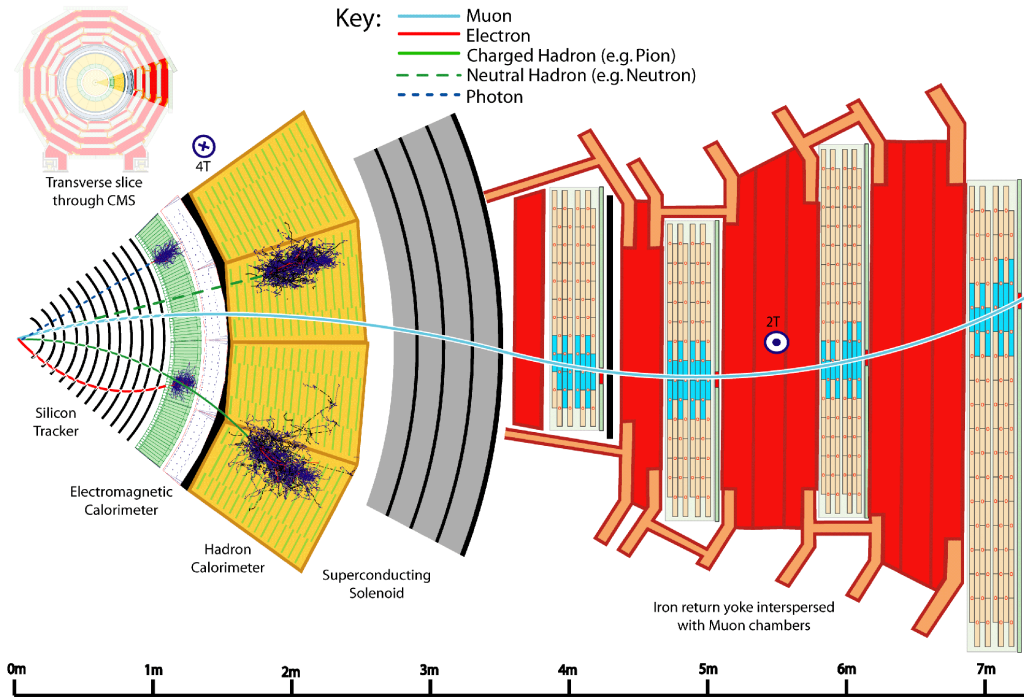
Figure 3.1: Schematic view of the CMS detector transverse section and stable particles' trajectories.

- **Muons**: muons are reconstructed by recursive algorithms that search for a match between tracks in the silicon tracker and in the muon chambers, yielding what is called a "global muon". A more detailed description is given in Sec. 3.2.1. A global muon gives rise to a PF muon if its combined p_{T} measurement is compatible within 3 standard deviations with the one provided by the sole tracker;

- **Electrons**: a PF electron is identified if a charged particle's track is associated with one or more ECAL energy clusters, which are built to account for the energy loss due to bremsstrahlung in the tracker layers;

- **Charged hadrons**: the remaining tracks give rise to PF charged hadrons if they are associated to energy clusters in the ECAL and HCAL. Their momentum is determined entirely by the tracker, owing to its better resolution with respect to the hadronic calorimeter;

- **Neutral hadrons and photons**: unmatched energy deposits in the ECAL are marked as PF photons, while those in the HCAL are assigned to PF neutral hadrons. Only neutral hadrons rely completely on the HCAL.

PF hadron candidates are then used by the anti-k_t algorithm to reconstruct jets. Once all particles have been identified and each track has been associated to a pp interaction point, it is possible to measure the missing transverse energy and to individuate the primary vertex (PV), defined as the one with the largest value of summed physics object p_T^2.

3.2 Muons

3.2.1 Reconstruction and identification

Muons produced at the collision point can travel across the entire detector, losing a negligible amount of energy through ionization with either layers of the inner tracker (*tracker track*) or the muon system (*standalone muon track*). These raw inputs are employed for the muon track reconstruction by applying recursive algorithms: a detailed description of the CMS detector performance in muon reconstruction and identification can be found in Ref. [37].

Standalone muon tracks are built by gathering all the information provided by muon subdetectors (CSCs, DTs and RPCs) along a muon trajectory, using a Kalman-filter technique [38]. Tracker muon tracks are built "inside-out" by propagating tracker tracks with $p_T > 0.5$ GeV and total spatial momentum greater than 2 GeV up to the muon system: if a match is found on a common surface, the tracker track is qualified as a tracker muon track. On the other hand, global muon tracks are built "outside-in", by associating standalone muon tracks with tracker tracks through a combined fit procedure. Including information recorded by both the tracker and muon system significantly improves the resolution of the muon p_T, as illustrated in

Fig. 3.2, which shows the RMS of relative q/p_T residuals as measured from cosmic rays, a quantity that is proportional to the muon trajectory curvature (q is the muon charge).
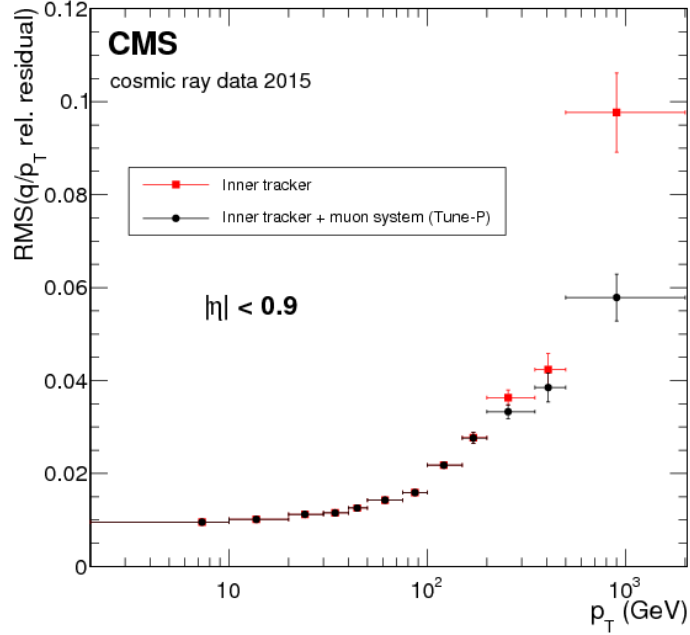

Figure 3.2: Muon p_T resolution measured in cosmic rays data recorded in 2015; when the muon system is used together with the inner tracker, the resolution significantly improves, especially for high energy muons.

In this work, the standard "tight muon" definition has been used to select global muons chosen by the PF algorithm, plus some requirements that were found to increase the signal efficiency for analyses with leptons coming from a W^+W^- bosons pair. The set of criteria applied on tight muons is shown in Table 3.1. The fit of the global track is required to have a $\chi^2/d.o.f. < 10$, use more than 5 tracker layers with valid hits and have at least 1 pixel hit. The transverse impact parameter with respect to the PV is required to be $d_{xy} < 0.2$ cm to reduce the rate of muons coming from in-flight decays, i.e. non-prompt muons that are usually produced by heavy B-hadrons that travel in the detector before decaying; likewise, the longitudinal impact parameter d_z is required to be less than 0.5 cm for tight muons.

As an additional requirement to reduce contributions from non-prompt muons, a multivariate (MVA) discriminator has been developed in the con-

Observable	Selection
Is global muon	True
Is PF muon	True
Tracker layers with valid hits	> 5
Number of valid pixel hits	> 0
Number of matched muon stations	> 1
$\chi^2/d.o.f.$	< 10
$d_{xy}(\mathrm{PV})$	< 0.2 cm
$d_z(\mathrm{PV})$	< 0.5 cm

Table 3.1: Summary of the tight muon identification requirements.

text of the ttH multileptonic analysis [39] ("ttHMVA"), and included in this work as well because of the similar final states considered. It combines together several observables for identifying and isolating muons with respect to other particles and is found to improve the background rejection without losing in signal efficiency: the MVA working point is chosen such that 80% of prompt leptons is selected out of $Z/\gamma^* \to \mu^+\mu^-$ events. A looser working point is used for the study and estimation of the non-prompt leptons background, as discussed in Sec. 5.2.4.

3.2.2   Isolation

What distinguishes a prompt muon, like those produced by either a W or Z boson decay, from a non-prompt one, typically due to in-flight decays of hadrons, is the isolation variable. Prompt muons are indeed expected to be not surrounded by other particles, conversely to what happens for non-prompt muons, that are generally found within jets and therefore characterized by many nearby particles. The muon isolation variable is evaluated as a function of the muon p_T, by summing up the energy within a cone of pre-defined radius ΔR. Tight muons are required to pass isolation requirements that also include pileup mitigation corrections; ultimately, these are needed in order to retain as little as possible sensitivity to pileup effects, which might spoil the isolation measurement by introducing spurious energy deposits from other vertices. The relative isolation variable is defined as follows:

$$I_{\Delta\beta}^{rel} = \Big[\sum_{ChH} p_T + max\Big(0, \sum_{NH} p_T + \sum_{Ph} p_T - 0.5 \sum_{ChHPU} p_T\Big)\Big]/p_T^{muons} \quad (3.1)$$

The sums in Eq. (3.1) are calculated in a cone of radius ΔR < 0.4 around the muon trajectory. The *ChH* subscript refers to charged hadrons coming

from the PV, *NH* to neutral hadrons, *Ph* to photons and *ChHPU* to charged hadrons not arising from the PV. This latter term is a correction factor for neutral hadrons coming from pileup, as their contribution is estimated to be roughly half of that of charged hadrons. The selection applied on the isolation variable is $I_{\Delta\beta}^{rel} < 0.15$ and is analysis dependent.

3.2.3   Identification and isolation efficiency

The muon identification and isolation efficiency is computed on data as a function of the muon p_{T} and η and compared to MC predictions, whose events are weighted in order to account for known sources of inaccuracy in the simulation. Generally speaking, event-by-event weights used to correct differences between MC and data are called "scale factors". In this case, the muon identification and isolation scale factor is derived as the ratio between the efficiency as measured from data and the one measured in the simulation. This efficiency can be broken down in the following contributions:

$$\epsilon_\mu = \epsilon_{\mathrm{trk}} \times \epsilon_{\mathrm{IDtight}} \times \epsilon_{\mathrm{ISOtight}} \times \epsilon_{\mathrm{ttHMVA>0.8}} \qquad (3.2)$$

In Eq. (3.2), ϵ_{trk} is the tracker muon efficiency, $\epsilon_{\mathrm{IDtight}}$ is the tight identification muon working point efficiency under the assumption that the muon passes the tracker selection, $\epsilon_{\mathrm{ISOtight}}$ is the tight isolation muon working point efficiency on top of previous selections and, finally, $\epsilon_{\mathrm{ttHMVA>0.8}}$ is the efficiency of the ttHMVA discriminator for values higher than 0.8, after that all other identification and isolation requirements have been applied to muon candidates.

The ϵ_μ efficiency is measured with the tag-and-probe method [40]. A well known mass resonance, such as the Z boson, is used to select particles of a desired type, and probe the identification and isolation efficiency on those particles. This technique is generic and can be used for calculating the efficiency related to other selections, if physics objects of interest are produced in pair. In this context, the "tag" is given by a tight muon, and "probe" muons are required to pass a much looser identification and isolation selection. Probes are then paired with tags, such that the invariant mass of the combination is consistent with the mass of the chosen resonance. In this way, a very pure sample of probes is selected.

Efficiencies are extracted from data and MC by fitting the invariant mass of the tag-probe pair, to also estimate the background contamination. This method is applied in bins of the muon p_{T} and η: ϵ_{trk} is $\simeq 1$ for muons with $p_{\mathrm{T}} > 20$ GeV, whereas $\epsilon_{\mathrm{IDtight}}$ is around 95–99% in almost all bins of the muon p_{T} and η. Simulated samples are then corrected by applying efficiency scale

factors on an event-basis. As an example, Fig. 3.3 shows the muon efficiency in two bins of the muon p_T as measured from DY events in the 2018 data set.
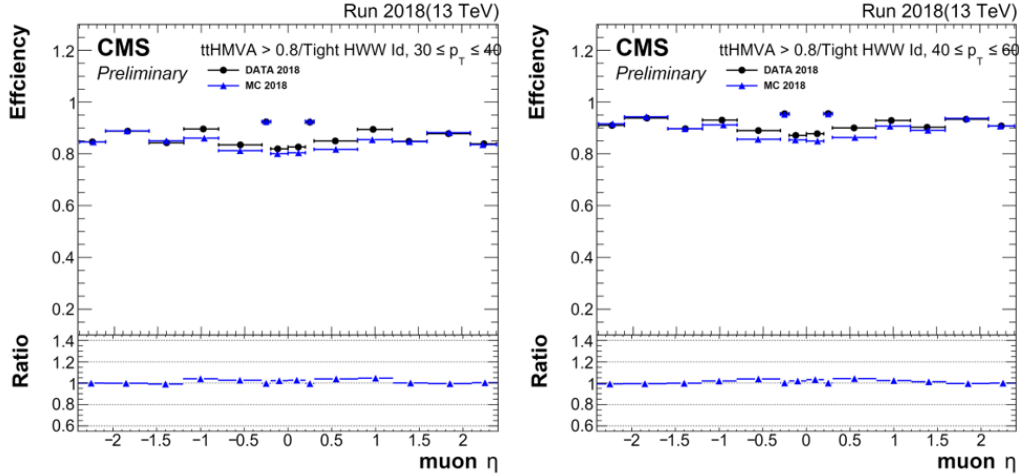

Figure 3.3: Muon identification and isolation efficiency distribution as a function of the muon η as measured in the 2018 data set for two different muon p_T bins: in the 30 GeV $< p_T <$ 40 GeV bin (left), the muon efficiency is about 85%, whereas it is around 90% in the 40 GeV $< p_T <$ 60 GeV bin (right). The muon efficiency is above 95% for $p_T >$ 60 GeV. Bottom panels show the scale factors used to correct simulated samples.

3.2.4 Momentum scale and resolution

The measurement of the muon p_T depends not only on the performance of CMS subdetectors, but also on the knowledge of the magnetic field, material composition and distribution in the detector, and spatial alignment of both tracker and muon system. These effects potentially bias measurements, if not taken into account. For low and intermediate p_T values, i.e., up to $\approx$ 100–200 GeV, the resolution in muon p_T measurements is dominated by the tracker performance. Calibrations and corrections are derived from the mean value of the distribution of $1/p_T$ as measured for tight muons from Z boson decays, and momentum scale corrections are further tuned by measuring the dimuon mass invariant spectrum [41]. Well-known low mass resonances, such as $\Upsilon(1S)$ and J/ψ, are used to improve statistics for the estimation of the momentum scale of muons around $\mathcal{O}(1)$ GeV. The resolution for muons with momentum up to 100 GeV is 1% in the barrel and 3% in the endcap, whereas scale corrections are 0.2% and 0.3%, respectively.

Since many searches for new physics are characterized by experimental signatures involving muons with $p_T > 200$ GeV, cosmic ray muons passing through the CMS detector are used to have a good estimation of the p_T resolution in this regime. Events are selected by requiring each muon to leave at least one hit in the pixel detector and pass through five strip layers, to ensure good quality reconstruction on the one hand, and mimic the trajectory of a muon from a pp collision on the other. As shown in Fig. 3.2, the muon system is crucial to improve the muon p_T resolution, which is about 5% at $p_T = 1$ TeV.

The effect of applying this set of corrections is well visible in Fig. 3.4, where the dimuon mass distribution of data collected in 2017 is compared to the MC prediction in a $Z/\gamma^* \to \mu^+\mu^-$ enriched control region.
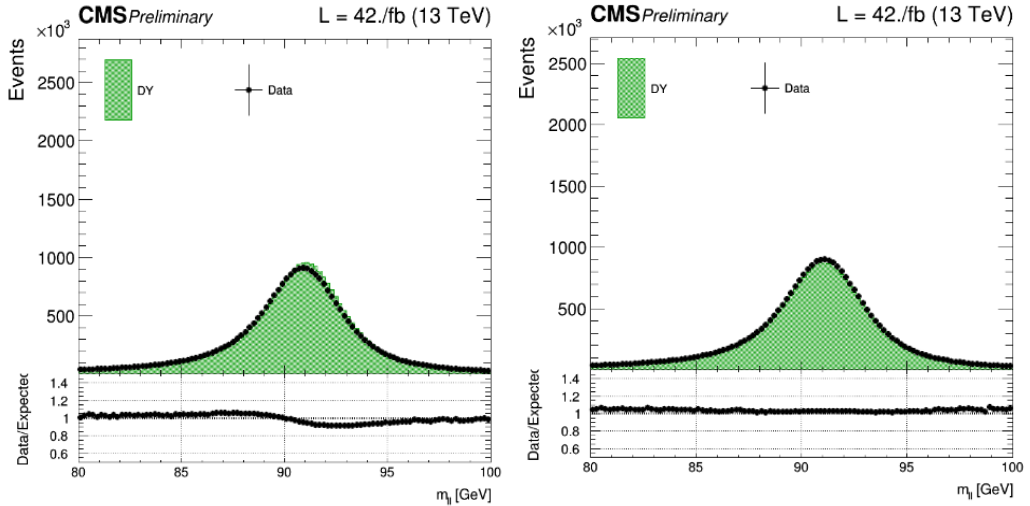
Figure 3.4: Data and MC comparison in a $Z/\gamma^* \to \mu^+\mu^-$ enriched control region before (left) and after (right) muon momentum scale corrections are applied. The wiggle around the Z boson mass peak is flattened when scale factors are included, improving the agreement between data and simulation.

3.3 Electrons

3.3.1 Reconstruction and identification

Electrons lose almost all of their energy in the ECAL and leave multiple hits in the tracker. However, by the time an electron has reached the ECAL, electrons may emit additional photons through bremsstrahlung radiation in

the tracker material, which roughly amounts to 1 X_0. The PF algorithm is capable of reconstructing electrons, starting from signals recorded by ECAL crystals. Whenever a nearby set of ECAL crystals collects an amount of energy much bigger than the expected electronic noise, a supercluster is formed, which covers a surface in the η–ϕ plane. Superclusters are defined to include photon conversion and bremsstrahlung losses, which are emitted along the path traveled by the electron in the tracker; for this reason, superclusters are typically narrow along the η direction and wide along the ϕ one, and are then associated with compatible hits in the pixel detector. Another method is used to test the compatibility of tracks with different electron trajectory hypotheses, as described in Ref. [42].

Similar to what has already been discussed for muons, there are several kinematic variables used to discriminate genuine prompt electrons from background sources, such as those originating from photon conversions, jets misidentified as electrons, or semileptonic heavy hadron decays:

- $\Delta\eta_{\mathrm{trk,SC}}$ and $\Delta\phi_{\mathrm{trk,SC}}$: they represent the spatial matching between the track and the supercluster in the η and ϕ coordinates, respectively;

- $\sigma_{i\eta,i\eta}$: it gives a measure of the electromagnetic shower shape along the η direction and is computed for all 5×5 block of crystals, centered on the highest energy deposit of ECAL superclusters;

- H/E: the ratio between the hadronic energy, deposited in the HCAL in a cone of radius $\Delta R = 0.15$ around the supercluster, and the energy of the electron candidate;

- $|1/E - 1/p|$: the difference between the inverse of the electron energy measured by the ECAL and the inverse of its momentum measured by the tracker;

- $N_{\mathrm{hits}}^{\mathrm{miss}}$: number of missing hits when back-propagating the electron track to the interaction point;

- d_{xy} and d_z: transverse and longitudinal impact parameters with respect to the PV, respectively;

- photon conversion veto: based on the number of missing hits $N_{\mathrm{hits}}^{\mathrm{miss}}$ in the inner tracker and used to suppress electron-positron pair production arising from photon conversions.

In this analysis, the "tight electron" working point is chosen to improve the signal-to-background ratio, and a summary of all selections is presented

in Table 3.2. Furthermore, an MVA discriminator was trained to improve the separation between prompt and non-prompt leptons, and is based on input variables related to the electron object reconstruction and identification. The training procedure was carried out separately in two different $|\eta|$ bins of the ECAL barrel region, and in the endcap region; the MVA working points are chosen to ensure 90% signal efficiency as measured from DY events. The "loose electron" working point definition, which is used for the non-prompt background estimation, does not make use of such a discriminator, but only relies on a cut-based selection.

	Yearly data set			
	2016		2017/2018	
MVA discriminator	`mva_90p_Iso2016` (90%)		`mvaFall17V1Iso` (90%)	
Observable	$|\eta_{SC}| \leq 1.479$	$1.479 < |\eta_{SC}| \leq 2.5$	$|\eta_{SC}| \leq 1.479$	$1.479 < |\eta_{SC}| \leq 2.5$
$\sigma_{i\eta,i\eta}$	< 0.011	< 0.031	< 0.011	< 0.031
$\Delta\eta_{\mathrm{trk,SC}}$	< 0.004	$-$	< 0.004	$-$
$\Delta\phi_{\mathrm{trk,SC}}$	< 0.020	$-$	< 0.020	$-$
H/E	< 0.060	< 0.065	< 0.060	< 0.065
$|1/E - 1/p|$	< 0.013 GeV^{-1}	< 0.013 GeV^{-1}	< 0.013 GeV^{-1}	< 0.013 GeV^{-1}
d_{xy}(PV)	< 0.05 cm	< 0.10 cm	< 0.05 cm	< 0.10 cm
d_z(PV)	< 0.10 cm	< 0.20 cm	< 0.10 cm	< 0.20 cm
Conversion veto	True	True	True	True
Missing inner hits	≤ 1	≤ 1	≤ 1	≤ 1

Table 3.2: Summary of the tight electron identification requirements.

3.3.2   Isolation

Similarly to what has been discussed related to the muon isolation variable, tight electrons, as defined in Table 3.2, are also required to pass isolation thresholds. These are taken into account through the "effective area" (EA)-correction technique described in [43], which further depends on the $|\eta|$ region of the ECAL system. The isolation variable is defined as:

$$I_{EA}^{rel} = \left[\sum_{ChH} p_T + max\left(0, \sum_{NH} p_T + \sum_{Ph} p_T - \rho A\right)\right]/p_T^{electrons} \qquad (3.3)$$

where ρ is the energy density associated to pileup events and A is an effective area. This area represents the size of a cone in which energy coming from pileup interactions has a large probability of being captured by the isolation variabile. In Eq. (3.3), sums are performed over a $\Delta R < 0.3$ radius around the electron flight direction. The selection applied on this variable is $I_{EA}^{rel} < 0.06$ in the 2017 and 2018 data set and $I_{EA}^{rel} < 0.0588$, $I_{EA}^{rel} < 0.0571$ in the 2016 data set for the ECAL barrel and endcap region, respectively. No

isolation requirements are instead applied in the loose electron working point definition.

3.3.3 Identification and isolation efficiency

The electron identification and isolation efficiency is computed in a similar fashion with respect to the method described for muons in Sec. 3.3.3. For instance, Fig. 3.5 shows the electron efficiency of the `mva_90p_Iso2016` discriminator, after applying the minimum selection of identification and isolation requirements, as a function of the electron probe p_{T}, as measured from 2016 data.
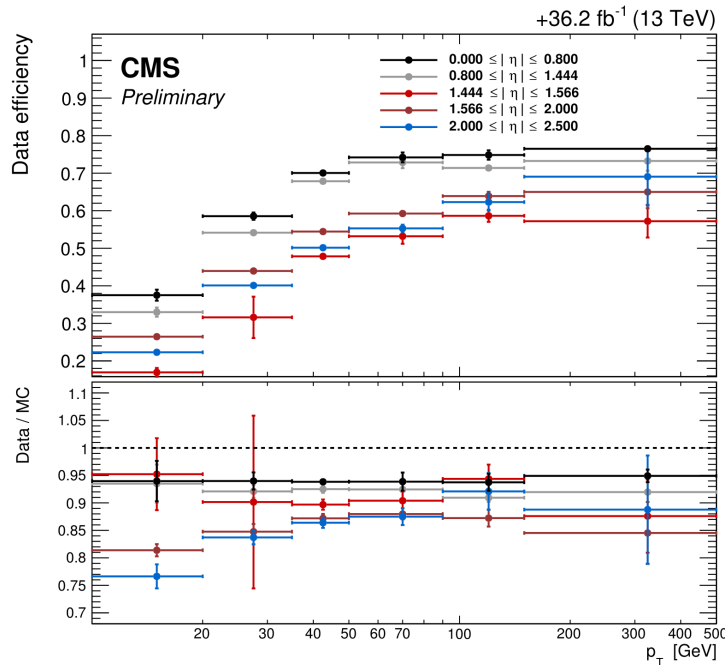
Figure 3.5: Electron identification and isolation efficiency distribution as a function of the electron probe p_{T}, as measured measured from 2016 data. Colored lines represent different bins of the η supercluster, and the bottom panel show the scale factors that are applied to simulated samples.

3.3.4 Momentum scale and resolution

The electron p_{T} is measured by combining the information collected by both the tracker and the ECAL. The electron energy scale has to be corrected to

take into account several losses that might happen when the particle interacts with the detector material: without any corrections, these losses result in a systematic shift that would lead to a degradation of the reconstructed energy.

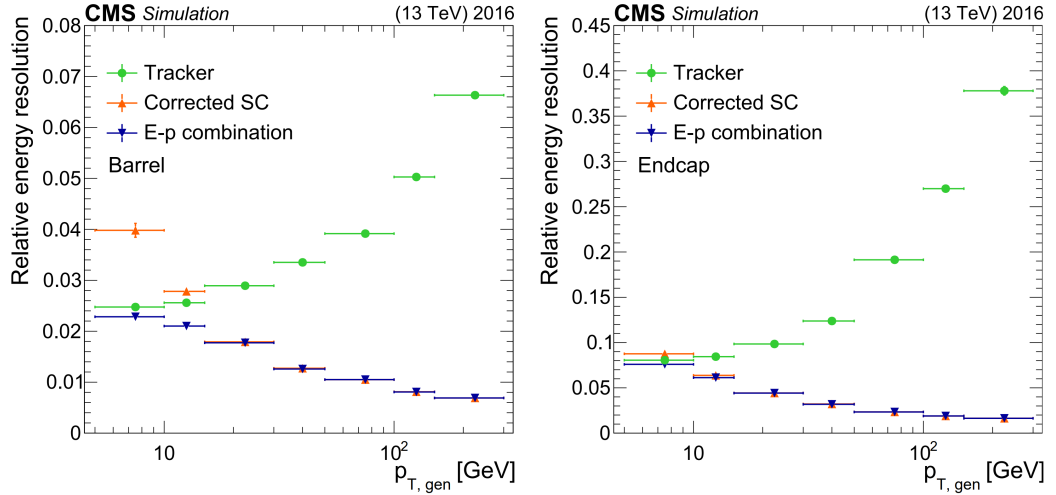Figure 3.6: Relative electron resolution as a function of the electron p_T as measured by the ECAL ("corrected SC"), by the tracker, and after applying the third regression ("E-p combination"). The relative energy resolution is measured in 2016 MC samples for the barrel (left) and the endcap (right) regions.

The ECAL response is calibrated through regression techniques that aim to reconstruct the true electron energy from its reconstructed value as measured in $Z \rightarrow e^+e^-$ events: the first regression provides corrections for the supercluster energy deposit, the second one gives an estimation of the supercluster energy resolution, and the last one combines the supercluster with the electron track information - as far as the reconstructed electron energy is less than 200 GeV. A detailed description of this method can be found in Ref. [42].

After applying energy scale corrections as derived by these regressions, the energy resolution ranges from 2% to 5%, depending whether the electron has been reconstructed in the barrel or in the endcap, respectively - as shown in Fig. 3.6 -, and on how much energy has been lost through bremsstrahlung radiation.

3.4   Lepton trigger efficiency

Analyses involving leptons in the final state usually select events of interest by using lepton triggers. In this work, the VBS signal is sought in the W^+W^- channel, focusing on W bosons leptonic decay. Since the final state can be populated with either electrons or muons, a variety of single and double lepton triggers is employed in the analysis, as described in detail in Sec. 4.1.

Above the trigger p_T threshold, the trigger efficiency, as reconstructed by HLT algorithms, reaches a plateau region. Nevertheless, such a turn-on curve is not an Heaviside function centered on the trigger p_T threshold itself, but rather the efficiency has a steep increase around this value that has to be properly accounted for in the simulation as well. This is done by measuring the trigger efficiency in data and then applying it on MC samples. In the following, the approach and formulas used for this analysis are described. The event efficiency ϵ_ev for an event with two leptons to pass a single lepton trigger (S) is:

$$\epsilon_\mathrm{ev} = 1 - (1 - \epsilon_{S,\ell_1}) \times (1 - \epsilon_{S,\ell_2}), \qquad (3.4)$$

where ϵ_{S,ℓ_1} and ϵ_{S,ℓ_2} are the efficiencies for the lepton with the highest (leading) and second-highest (trailing) p_T in the event, respectively, to pass the single lepton trigger. An event with two reconstructed leptons is then selected if either one of the two leptons passes the single lepton trigger. For double lepton triggers (D), the efficiency is computed separately for each "leg" composing the trigger, i.e, for each trigger object as selected by the HLT algorithm. In this case the formula used to compute ϵ_ev is:

$$\epsilon_\mathrm{ev} = \epsilon_{D,\ell_1}^\mathrm{lead} \times \epsilon_{D,\ell_2}^\mathrm{trail} + (1 - \epsilon_{D,\ell_1}^\mathrm{lead} \times \epsilon_{D,\ell_2}^\mathrm{trail}) \times \epsilon_{D,\ell_1}^\mathrm{trail} \times \epsilon_{D,\ell_2}^\mathrm{lead}, \qquad (3.5)$$

where $\epsilon_{D,\ell_1}^\mathrm{lead(trail)}$ is the efficiency of the leading lepton ℓ_1 in the event to pass the leading (trailing) lepton trigger leg; similarly, $\epsilon_{D,\ell_2}^\mathrm{lead(trail)}$ is the efficiency of the trailing lepton ℓ_2 in the event to pass the leading (trailing) lepton trigger leg. In Eq. (3.5), the two trigger legs are considered uncorrelated with each other, meaning that per-leg efficiencies are assumed to be independent, and this is very well verified.

Ultimately, ϵ_ev is computed in data by taking the boolean OR of the event efficiencies as described in Eqs. (3.4) and (3.5), and MC samples are reweighted by this factor as a function of the lepton p_T and η.

3.5 Jets

Jets are the pyhsics objects associated with quarks and gluons produced in high energy collisions. As introduced in Sec. 1.2.2, they arise from the hadronization of partons from the hard scattering event. In this section, jet reconstruction techniques used by the CMS collaboration are described.

3.5.1 Reconstruction

There are several clustering methods that can be implemented to combine individual momenta of PF candidates until a jet object is formed. To do so, energy deposits from the ECAL and the HCAL are matched to the tracker information, further improving the p_{T} resolution of particles within jets.

Since jets must satisfy both infrared and collinear conditions, the standard clustering algorithm used by the CMS collaboration is the anti-k_{t} one, which proceeds as follows. For each particle i with measured transverse momenta $k_{\mathrm{t},i}$, two definitions of distance are given:

$$d_{i,B} \equiv k_{\mathrm{t},i}^{-2} \tag{3.6}$$

$$d_{i,j} \equiv min(d_{i,B}, d_{j_B}) \frac{\Delta R_{ij}^2}{R^2} \tag{3.7}$$

where $d_{i,B}$ is the distance from the beam, $d_{i,j}$ is the distance from another j-th particles, ΔR_{ij} is defined by equation (1.15) and R is an adimensional parameter, set to 0.4. The smallest distance between $d_{i,B}$ and $d_{i,j}$ is chosen, where $d_{i,j}$ is calculated by varying the j index; if $d_{i,j}$ is smaller than $d_{i,B}$, the i-th and the j-th particles are combined into a new system, summing their four-momentum, and the algorithm restarts from the first step. Otherwise, i is declared as a jet. The procedure is repeated until no particles are left.

The anti-k_{t} algorithm is protected by QCD divergences: the $d_{i,B}$ and $d_{i,j}$ distances are collinear-safe by definition, while the infrared-safety is ensured by requiring a minimum threshold on the jet's momenta. Since the anti-k_{t} algorithm involves a weighted sum of $1/k_{\mathrm{t}}^2$ terms, it favours the merging of high transverse momentum particles, from which the jet starts growing in a circular shape.

When reconstructing PF jet candidates, photons are assumed to be massless and charged hadrons are assigned the charged pion mass. Charged particles coming from pileup vertices are removed from the list of PF candidates before clustering, as described in Ref. [44] (CHS method): in this way, the jet energy and substructure are almost independent of pileup effects.

3.5.2 Identification

As for the leptons, jets are required to pass quality criteria in order to reduce the contamination from sources of fake jets, like noisy calorimetric cells. This set of selections is referred to as "jet ID" working point, and, for this analysis, the tight working point has been chosen; a summary of these requirements is shown in Table 3.2. The η coverage of jet ID selections is limited by the detector acceptance, and, indeed, all quantities related to the identification of charged particles are performed within $|\eta| < 2.4$, which is the range spanned by the tracker system.

Observable	$|\eta|$ range	Selection
p_{T}	$|\eta| < 5.2$	> 15 GeV
Charged hadron fraction	$|\eta| < 2.4$	> 0.0
Charged multiplicity	$|\eta| < 2.4$	> 0
Charged electromagnetic fraction	$|\eta| < 2.4$	< 0.99
Neutral hadron fraction	$|\eta| < 2.7$	< 0.9
Neutral electromagnetic fraction	$|\eta| < 2.7$	< 0.9
Neutral multiplicity	$2.7 < |\eta| < 3$	> 2
	$3 < |\eta| < 5.2$	< 10

Table 3.3: Summary of the tight jet ID working point requirements.

Moreover, tight jets with $p_{\mathrm{T}} < 50$ GeV are required to pass a loose pileup jet identification selection, since pileup jets are expected to be softer than those coming from the PV. The identification of pileup jets relies also on the observation they tend to be broader than jets originating from the hard scattering event, as they come from multiple overlapping particles rather than from a single quark or gluon. An MVA discriminator is trained to identify such jets, and more details are given in Ref. [45].

Scale factors are applied to simulated samples to correct for known discrepancies between simulation and data in terms of mistagging rate and efficiency. In order to discard events in which a lepton can be mistakenly reconstructed as a jet, additional offline selection are applied in this analysis, and will be further discussed in Sec. 5.1.

3.5.3 Energy scale and resolution

The energy response of the detector has to be calibrated to measure a correct value of the jet energy scale (JES). Several uncertainty sources affect this procedure and they have to be taken into account by any analysis involving jets in the final state, as it is the case for VBS searches.

The jet energy response is defined as the ratio between the reconstructed jet p_T and the particle-level jet p_T as clustered from stable and visible final-state particles with decay length greater than 1 cm. The simulated jet response of CMS calorimeters is shown in Fig. 3.7.
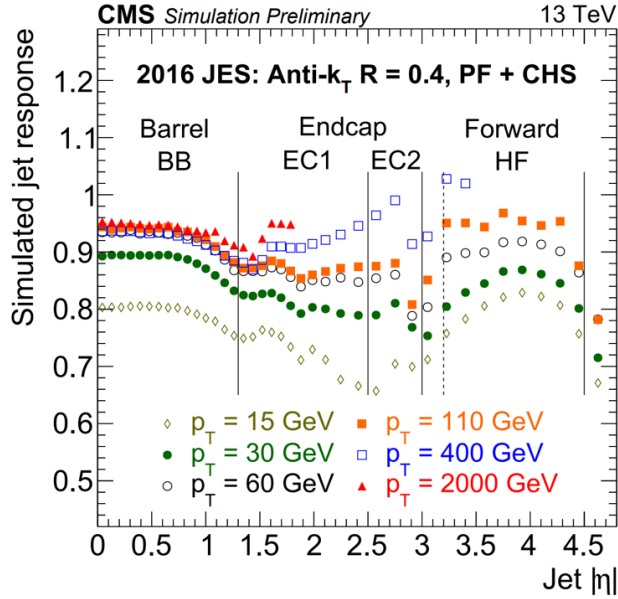

Figure 3.7: Simulated jet response as a function of the jet p_T and $|\eta|$.

Jet energy corrections (JECs) are derived as a function of the jet p_T and η and each contribution is applied in sequence to the "raw" jet four-momentum. A list of all factors included in the JECs is reported below and computed in the same order as presented.

- **Pileup offset:** The contribution from spurious tracks and calorimetric deposits populating each event and originating from secondary pp collisions has to be corrected for. This is the "in-time" pileup component and is strongly reduced by applying the CHS method. However, because of the finite signal decay time in the calorimeters, pp collisions occurring in the previous and subsequent bunch crossings can also create energy deposits ("out-of-time" component). Therefore, this contribution must be taken into account as well in the jet energy response. The two components are estimated on an event-basis and then subtracted per jet with the "jet area method" described in Ref. [43].

- **MC calibration:** The simulated response is corrected in such a way that, on average, the reconstructed jet p_T is equal to one generated at

particle-level. Corrections are extracted from a simulated QCD dijet sample and derived as a function of the jet p_T and η, to make the response uniform over these two variables. MC calibration corrections are applied both in data and simulation.

- **Relative energy scale:** Residual η-dependent corrections to the jet energy response are derived by selecting dijet events from data and applying the tag-and-probe technique. In this context, the tag is given by a jet reconstructed within $|\eta| < 1.3$, whereas the probe is left unconstrained. Corrections of the order of 2% are measured in the barrel, increasing up to 10% in the forward region of the calorimeter.

- **Absolute energy scale:** The jet response as measured in data must be corrected for any p_T dependence as well, that might give rise to small discrepancies between data and simulation. The idea is to calibrate the jet p_T against a reference object, by exploiting the p_T balance at particle-level. This is done in Z + jets and γ + jets as a function of either the Z boson or γ p_T, by using the MPF method described in Ref. [46]. Both the relative and absolute energy scale corrections are only applied to data.

As the jet energy estimation procedure involves several techniques, there are as many uncertainty sources that can contribute to the determination of JECs. In Fig. 3.8, each JES uncertainty component is shown and summed in quadrature to compute the combined uncertainty. At low jet p_T and high jet $|\eta|$, the pileup uncertainty dominates over other sources, whereas in the 20 GeV $< p_T <$ 200 GeV regime, the largest uncertainty is given by the estimation of the QCD flavor composition in terms of jet constituents, which is performed during the MC calibration procedure.

Dijet measurements and the p_T balance method described above are used to extract the jet p_T resolution from data and simulation. Since the jet energy resolution (JER) is found to be worse in data than MC samples, the simulation of reconstructed jet is smeared in order to correct for this difference. JER typically ranges from 15–20% at jet $p_T \simeq 30$ GeV down to 10% (5%) at jet $p_T \simeq 100$ GeV (1 TeV).

3.5.4   b-tagging

Another important aspect of jet reconstruction is the capability to distinguish jets originating from the hadronization of b quarks (b-jets). Although VBS jets come from light quarks, b-jets are found in the largest background contribution to this analysis, as they are produced from the decay of $t\bar{t}$ quark
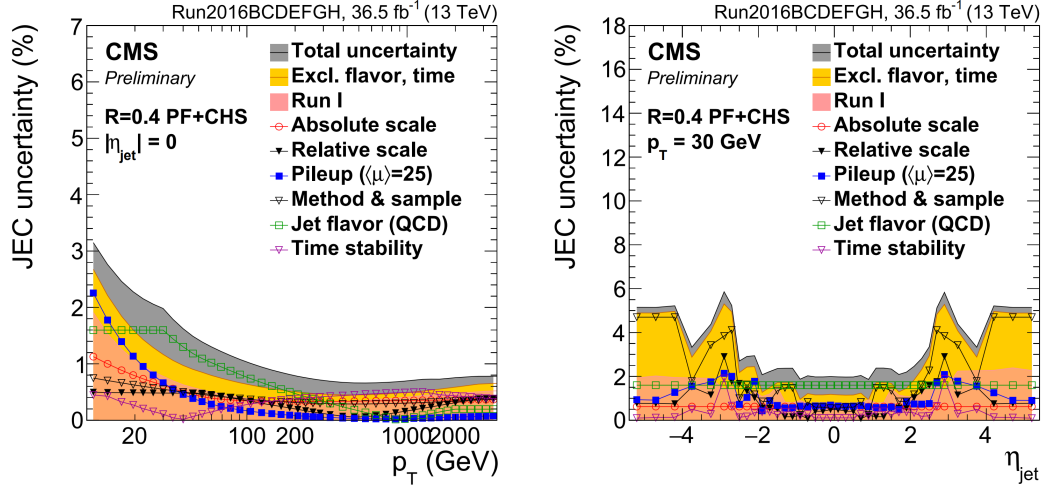
Figure 3.8: JEC uncertainties as a function of the jet p_T (left) for reconstructed jets with $\eta = 0$ and as a function of η (right) for jets with $p_T = 30$ GeV. Jets are reconstructed with the PF algorithm using the anti-k_t clustering technique and applying the CHS method. Results are based on CMS data collected in 2016.

pairs. Therefore, having an efficient algorithm for separating jets induced by light quarks (or gluons) from b-jets is utterly crucial for this analysis. Such algorithms are known as b-tagging algorithms.

The long lifetime of B-hadrons produced within b-jets is one of the most typical signature used to tag b-jets. Eventually, tracks from B-hadrons decay are back-propagated to a displaced position with respect to the PV, because of their non-negligible decay time. This information is one the key input observable employed to build more sophisticated b-tagging techniques.

Indeed, depending on their p_T, B-hadrons can travel from a few mm to 1 cm across the detector, giving rise to a secondary vertex (SV), which is associated with displaced tracks. The distance between the PV and these tracks at their point of closest approach to the PV is called impact parameter (IP), as depicted in Fig. 3.9. A sign is assigned to the IP, depending on whether the azimuthal angle between the track and the jet-axis is less (positive) or greater (negative) than $\pi/2$. Because B-hadrons are produced within a jet, they tend to have positive IP values, whereas prompt tracks equally populate the IP distribution. Furthermore, a B-hadron has a 20% probability to decay into a final state with either an electron or a muon, thus the multiplicity of charged leptons is also exploited to identify b-jets.

Several b-tagging algorithms have been developed by the CMS collaboration [47], but they all feature an output discriminator which quantifies the
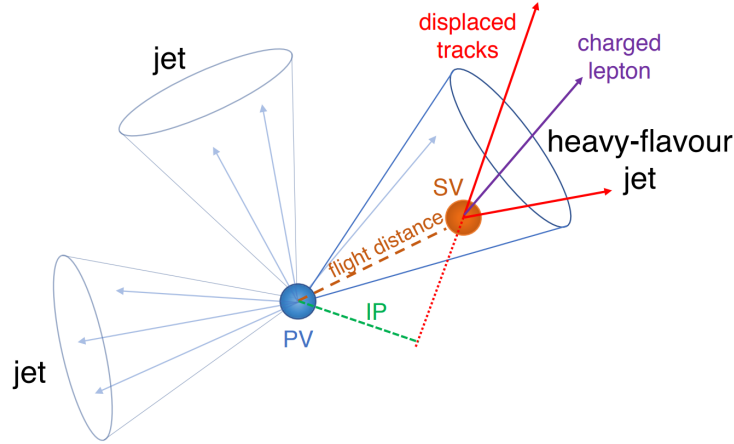
Figure 3.9: Illustraion of a generic heavy-flavor jet with a SV coming from a B-hadron. The IP of the highlighted track is given bt the dashed green line.

probability of a jet to be identified as a b-jet. For each of them, three recommended working points are usually provided - loose, medium and tight -, corresponding to different values of the b-tagging efficiency, as measured in b-quark enriched events, and mis-tagging rate, i.e. the probability for a b-jet to be mis-reconstructed as a light or gluon jet. Mis-tagging probabilities are 10%, 1% and 0.1% for the loose, medium and tight working point, respectively. In this analyisis, the DEEPJET algorithm [48] is used to suppress $t\bar{t}$ and tW background contributions from the signal region. Conversely, the requirement on the DEEPJET discriminator is reverted to select such events in a control region: a loose working point is applied in this case, ensuring a more than 90% b-tagging efficiency over the entire p_{T} spectrum of $t\bar{t}$ events. Fig. 3.10 shows the performance of DEEPJET algorithm against other benchmark algorithms used by the CMS collaboration.

3.6 Missing transverse energy

At hadron colliders, the missing transverse energy $p_{\mathrm{T}}^{\mathrm{miss}}$ is an interesting physics observable to measure, because, before the pp collision occurs, the initial total momentum in the transverse plane with respect to the beam axis is almost zero. Moreover, high $p_{\mathrm{T}}^{\mathrm{miss}}$ events might be typical signatures of new exotic particles, such as dark matter, and therefore it is a quantity that has to be reconstruct with the highest level of possible precision. In this analysis, the $p_{\mathrm{T}}^{\mathrm{miss}}$ variable is mainly due to the two escaping neutrinos arising from W boson decays, but, in general, contributions are also given by detector
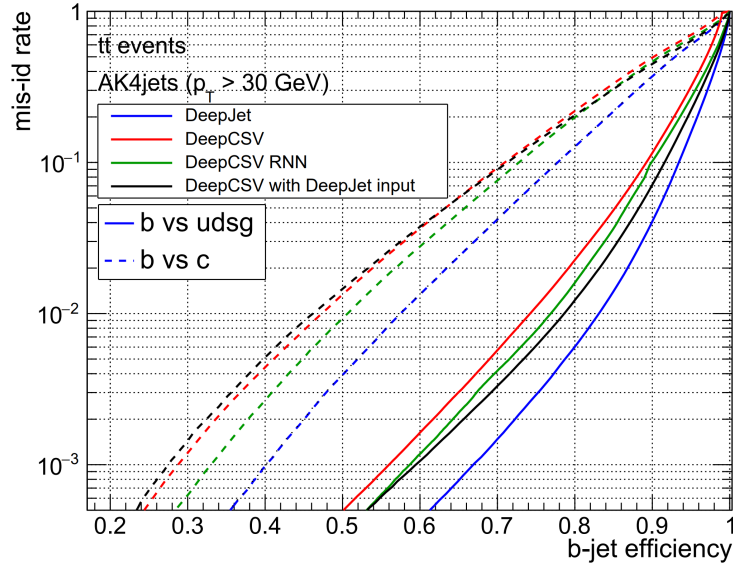
Figure 3.10: Simulated performance of the DEEP JET algorithm against other algorithms commonly used within the CMS collaboration and measured from $t\bar{t}$ events.

inefficencies.

Once all other physics objects are created by the PF algorithm, their transverse momentum is used to build the p_T^{miss} observable, which is defined as the negative vectorial p_T sum of all PF candidates in the event. The PF technique relies on the underlying PUPPI algorithm [49] to reduce the pileup dependence of p_T^{miss}. Its basic idea is to assign a shape variable to each particle which is sensitive to differences between collinear configurations arising from QCD jets and soft pileup radiation [50]. A χ^2 distribution is used to estimate the likelihood that a PF candidate originated from a pileup event, and transformed to a weight that is required to be greater than 0.01.

The p_T^{miss} estimation depends on several factors that can cause an inaccurate reconstruction of this observable, such as the non-linearity of the calorimeter response to hadrons, miminum requirements in energy deposits and track p_T, and all sources of inefficencies that might enter the PF algorithm. Moreover, the p_T^{miss} variable is particularly sensitive to the unclustered energy, i.e., contributions from PF candidates not associated with any physics objects. Therefore, it is important to have a good calibration of the p_T^{miss} response of the detector. To improve the accuracy of this estimation, PF jets with $p_T > 15$ GeV are corrected for all contributions described in Sec. 3.5.3, so that these corrections are propagated to the p_T^{miss} measurement. Only PF jets that have less than 90% of their energy deposited in the ECAL

are considered when applying this correction, in order to avoid any undesired overlap with electrons and photons.

In the very high-p_T^{miss} regime, anomalies can occur because of a variety of reconstruction failures or localized mulfunctioning in some subdetectors. For instance, noisy sensors in the ECAL may generate spurious energy deposits, and similar effects can also happen in the HCAL. Dedicated algorithms have been developed to filter out these events from data.

3.6.1   Energy scale and resolution

As for the JES determination, the p_T^{miss} is calibrated using either Z $(\to \ell^+\ell^-)$ boson and $\gamma + $ jets events. These processes does not involve any genuine p_T^{miss} in the final state because there are no expected neutrinos, therefore they are particularly suitable to calibrate the p_T^{miss} response of the detector. The reconstruction performance is evaluated by comparing the boson transverse momentum $\vec{q}_T$ with that of the recoiling hadronic system in the event $\vec{u}_T$, as depicted in Fig. 3.11. Momentum conservation in the transverse plane implies $\vec{u}_T + \vec{q}_T + p_T^{\text{miss}} = 0$. The p_T^{miss} detector response is defined as $-\langle u_{||}\rangle/\langle \vec{q}_T\rangle$, which is the ratio between the mean of the parallel component of the hadronic momentum and that of $\vec{q}_T$. Fig. 3.12 shows instead the performance of the PUPPI p_T^{miss} variable in Z $\to \ell^+\ell^- + $ jets events as measured in 2016 data, after JEC have been applied.
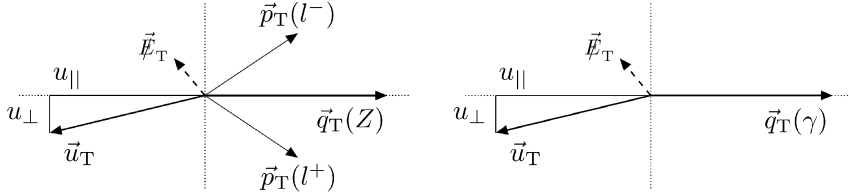

Figure 3.11: Illustration of the Z boson (left) and γ (right) event kinematics as reconstructed in the transverse plane. The $\vec{q}_T$ vector is a given by the vectorial sum of PF candidates except for the two leptons from the Z boson (left) or γ (right).
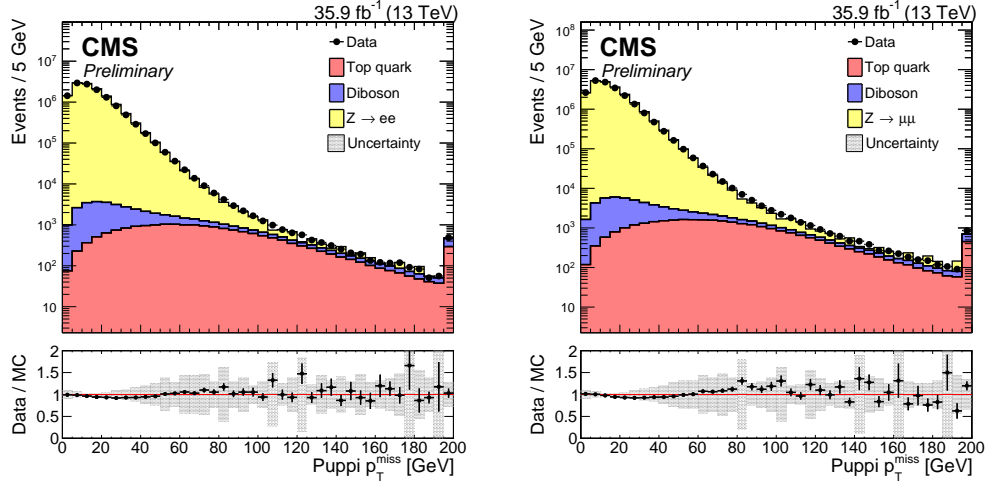
Figure 3.12: Distributions of PUPPI p_T^{miss} in $Z \to e^+e^-$ (left) and $Z \to \mu^+\mu^-$ (right) events.

3.7   Monte Carlo corrections

Any source of discrepancy between data and MC must be taken into account. The adopted solution is to reweight each MC event with several scale factors, aiming to correct any disagreement with data to the best of possible level. The main contributions to scale factors are listed below; for those already presented in this Chapter, no additional description is given:

- **Luminosity**: MC samples are normalized to yearly data integrated luminosity;

- **Lepton identification and isolation**;

- **Lepton trigger efficiency**;

- **Lepton momentum scale**;

- **PU**: it is needed to equalize the pileup distribution between data and simulation, since the LHC instantaneous luminosity may vary during the data taking period. This scale factor is calculated as the ratio between the measured and the estimated number of pileup interaction in data and MC, respectively;

- **Jet PU identification**;

- **b-tagging**;

- **L1 prefiring corrections**: additional trigger efficiency scale factors
  are derived from data and applied in MC simulation to correct for a
  gradual shift in the timing of the ECAL L1 trigger inputs. This was
  observed in the 2016 and 2017 data taking period and have caused a
  specific trigger inefficency at $|\eta| > 2$. The efficiency loss is $\approx$ 10–20%
  for an electron (jet) with p_T larger than 50 (100) GeV in the $2.5 < |\eta| <$
  3 ECAL region.

Another important set of corrections to account for is related to the determination of the JES, but it is not included in MC samples as a scale factor. Indeed, as discussed in detail in Sec. 3.5.3, JECs are applied to the raw measured jet p_T to compensate for the detector response and estimate the true jet four-momentum.

In order to check the level of agreement between data and simulated samples after all corrections are included, I provide an auxiliary set of plots as a closure test. Indeed, for each physics object entering the analysis, a corresponding observable of interest is considered to verify the goodness of scale factors. Data and MC comparisons are drawn for each year of data taking.

For leptons, a 20 GeV window is selected around the Z boson mass peak, and we look at the invariant mass distribution of the lepton pair coming from the Z boson decay. In Fig. 3.13, this observable is plotted separately for electrons and muons in a $Z \to \ell^+\ell^-$ enriched phase space, where leptons are required to pass the same p_T thresholds as those of the analysis (see Sec. 4.1 and 5.1). Since this region is inclusive in terms of other particles that can be produced in association with the Z boson, we also checked the distribution of the number of jets, as these objects play a crucial role in this analysis.
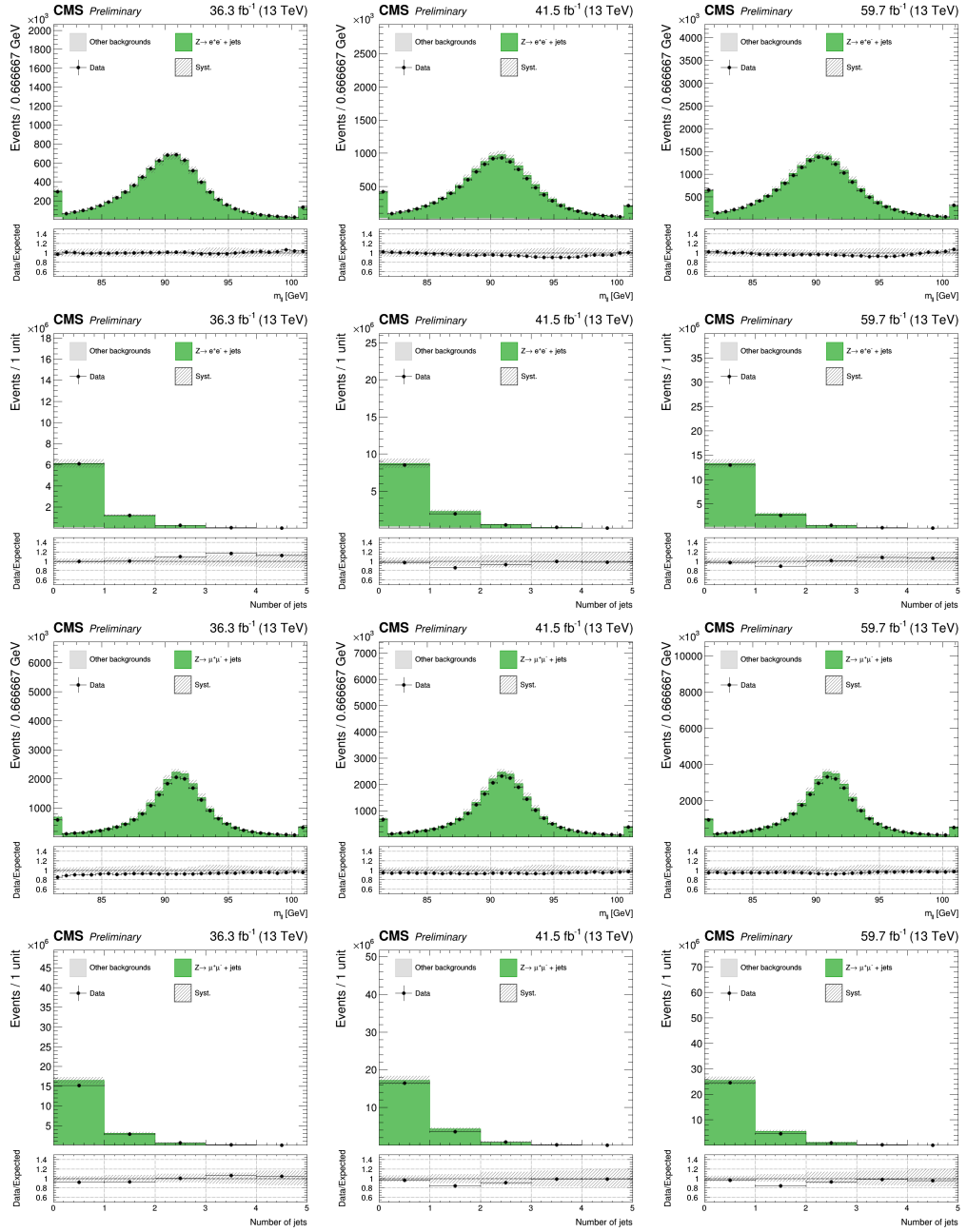
Figure 3.13: Closure test for electrons, muons and jets corrections in a $Z \to \ell^+\ell^-$ + jets enriched phase space. The $m_{\ell\ell}$ and number of jets distributions are shown for the ee ($\mu\mu$) final state in the first and second (third and fourth) row, respectively. Data and MC simulation of 2016 (left), 2017 (center) and 2018 (right) data sets well agree within their uncertainties. Residual normalization discrepancies are corrected by the background estimation procedure adopted in this analysis.

The good modeling of b-jets is verified in a top quark enriched control region, where $t\bar{t}$ and tW production dominate over other processes. In particular, we require the highest p_T jet in the event to pass the loose working point of the DEEPJET algorithm - as we do in the analysis - and we draw the corresponding b-tagging score for the second-highest p_T jet. In a similar fashion to the previous comparison, signal-like leptons are selected, but only eμ leptons pairs are considered for this study, to suppress the $Z \to \ell^+\ell^-$ contribution. As it can be observed from Fig. 3.14, the shape of the b-tagging output distribution is well described by simulated samples after b-tagging scale factors have been applied. This control region is additionally used to check the data-to-MC ratio in the p_T^{miss} observable, which come from real neutrinos emitted along with leptons in the final state.
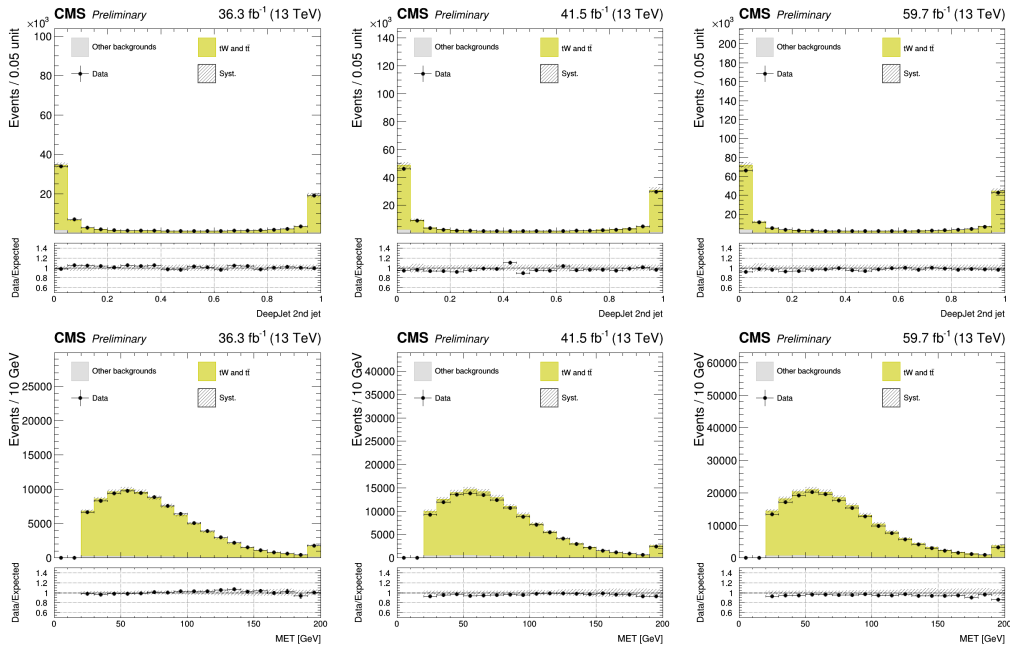
Figure 3.14: Closure test for b-jets and p_T^{miss} corrections in a top quark enriched phase space. The DEEPJET score of the second-highest p_T jet and p_T^{miss} distributions are shown for the eμ final state in the first and second row, respectively. Data and MC simulation of 2016 (left), 2017 (center) and 2018 (right) data sets well agree within their uncertainties. Residual normalization discrepancies are corrected by the background estimation procedure adopted in this analysis.

Chapter 4

Data and Monte Carlo

Precise Monte Carlo simulations provide a consistent way to describe data as acquired from the LHC machine, and represent our best knowledge of fundamental interactions. The aim of this Chapter is to illustrate how data are selected (Sec. 4.1) and how the signal assumption and background processes are modeled (from Sec. 4.2 to 4.4).

4.1 Data sets and triggers

The data samples used in this work were collected during the 2016–2018 CMS data taking of p-p collisions at $\sqrt{s} = 13$ TeV and they correspond to an integrated luminosity of 36.3, 41.5, and 59.7 fb^{-1}, respectively; the overall integrated luminosity is about 138 fb^{-1}.

Events firing either single or double lepton triggers are selected, and their HLT p_{T} thresholds depend on the considered data set and run period. Because of the high LHC instantaneous luminosity, single lepton triggers p_{T} requirements must be increased with respect to those of double lepton triggers, in order to keep a trigger rate sustainable for mass storage. A summary of all triggers used in the analysis, as well as their requirements in lepton p_{T} and η ($|\eta| < 2.5$ unless otherwise stated), is shown in Tables 4.1–4.3 per LHC run period.

A combination of the aforementioned single and double lepton triggers is finally employed to select signal candidates, reaching more than 98% in signal efficiency. However, HLT triggers are not directly applied in MC simulation, rather all simulated samples are weighted event-by-event by the trigger efficiency as measured in data, in bins of lepton p_{T} and η.

Trigger	Run period	Threshold
Electron-Muon	B–F(–278273)	$p_\mathrm{T} > 23$ and 12 GeV
	F(–278273)–H	$p_\mathrm{T} > 23$ and 8 GeV
Muon-Electron	B–F(–278273)	$p_\mathrm{T} > 23$ and 8 GeV
	F(–278273)–H	$p_\mathrm{T} > 23$ and 12 GeV
Single Muon	B–H	$p_\mathrm{T} > 24$ GeV
Single Electron	B–H	$p_\mathrm{T} > 27$ GeV and $2.1 < |\eta| < 2.5$
		$p_\mathrm{T} > 25$ GeV and $|\eta| < 2.1$
Double Muon	B–H	$p_\mathrm{T} > 17$ and 8 GeV
Double Electron	B–H	$p_\mathrm{T} > 23$ and 12 GeV

Table 4.1: HLT triggers and requirements used for selecting signal candidates in 2016 data set. Each letter in the second column corresponds to a different "era", i.e. a collection of data taking periods (runs, labeled by a number) sharing similar LHC and detector conditions.

Trigger	Run period	Threshold
Electron-Muon	B	$p_\mathrm{T} > 23$ and 12 GeV
	C–F	$p_\mathrm{T} > 23$ and 12 GeV
Muon-Electron	B	$p_\mathrm{T} > 23$ and 12 GeV
	C–F	$p_\mathrm{T} > 23$ and 12 GeV
Single Muon	B–F	$p_\mathrm{T} > 27$ GeV
Single Electron	B–F	$p_\mathrm{T} > 35$ GeV
Double Muon	B	$p_\mathrm{T} > 17$ and 8 GeV
	C–F	$p_\mathrm{T} > 17$ and 8 GeV, $m_{\ell\ell} > 8$ GeV
Double Electron	B–H	$p_\mathrm{T} > 32$ and 12 GeV

Table 4.2: HLT triggers and requirements used for selecting signal candidates in 2017 data set.

Trigger	Run period	Threshold
Electron-Muon	A–D	$p_\mathrm{T} > 23$ and 12 GeV
Muon-Electron		$p_\mathrm{T} > 23$ and 12 GeV
Single Muon	A–D	$p_\mathrm{T} > 24$ GeV
Single Electron	A–D	$p_\mathrm{T} > 32$ GeV
Double Muon	A–D	$p_\mathrm{T} > 23$ and 12 GeV
Double Electron	A–D	$p_\mathrm{T} > 32$ and 12 GeV

Table 4.3: HLT triggers and requirements used for selecting signal candidates in 2018 data set.

4.2   Monte Carlo samples

Several MC event generators are used to simulate signal and background processes, except for the non-prompt lepton contribution which is entirely estimated from data, as it will be discussed in Sec. 5.2.4. All samples are reweighted to account for known discrepancies between data and simulated events, the full list of corrections is given in Sec. 3.7. Table 4.4 summarizes what MC tools were used to simulate signal and background samples, along with their cross section and QCD accuracy. All matrix element generators listed below are interfaced to PYTHIA 8 [51] to simulate the effects of parton showering, multiple parton interactions and hadronization; generated events are processed through a detailed simulation of the CMS detector based on the GEANT4 package [52], and are then reconstructed with the same algorithms as used for data. The chosen set of PDF and underlying event tune are common to all simulated events for a given data set. The former is provided by the NNPDF collaboration and corresponds to version 3.0 [53,54] (3.1 [55]), the latter is included in the PYTHIA 8 simulation and is CUETP8M1 [56] (CP5 [57]) for the 2016 (2017–2018) MC data set.

Process	MC event generator	$\sigma \times$BR [pb]	QCD order
EW $W^+W^- \to 2\ell2\nu$ (signal)	MadGraph5_aMC@NLO	0.08875	LO
QCD-induced $W^+W^- \to 2\ell2\nu$	POWHEG v2	11.95	NNLO
Gluon-induced $W^+W^- \to 2\ell2\nu$	MCFM	0.57483	NLO
$t\bar{t}$ ($\to b\bar{b}\ 2\ell2\nu$)	POWHEG v2	87.310	NLO
tW	POWHEG v2	35.60	NLO
Single top quark t-channel	POWHEG v2	44.33	NLO
Single anti-top quark t-channel	POWHEG v2	23.38	NLO
Single top quark s-channel	MadGraph5_aMC@NLO	3.360	NLO
$Z/\gamma^* \to \tau^+\tau^-$ + jets ($\tau^+\tau^- \to e^\pm\mu^\mp4\nu\ m_{\ell\ell} > 50$ GeV)	MadGraph5_aMC@NLO	255.63	NLO
EW Z + 2 jets (Z $\to \ell^+\ell^-$, $m_{\ell\ell} > 50$ GeV)	MadGraph5_aMC@NLO	4.321	LO
Wγ	MadGraph5_aMC@NLO	405.271	LO
Zγ (Z $\to \ell^+\ell^-$)	MadGraph5_aMC@NLO	58.83	NLO
WZ (2ℓ2q)	MadGraph5_aMC@NLO	5.5950	NLO
WZ/γ^* (3$\ell\nu$, $m_{\ell\ell} > 0.01$ GeV)	POWHEG v2	58.59	NLO
ZZ (2ℓ2ν)	POWHEG v2	0.564	NLO
ZZ (2ℓ2q) (2016)	POWHEG v2	3.220	NLO
ZZ (2ℓ2q) (2017,2018)	MadGraph5_aMC@NLO	3.220	NLO
ZZ (4ℓ)	POWHEG v2	1.212	NLO
ZZZ	MadGraph5_aMC@NLO	0.01398	NLO
WZZ	MadGraph5_aMC@NLO	0.05565	NLO
WWZ	MadGraph5_aMC@NLO	0.16510	NLO
WWW	MadGraph5_aMC@NLO	0.18331	NLO
ggF H $\to W^+W^- \to 2\ell2\nu$	POWHEG v2 + JHUGen	1.0315	NLO
ggF H $\to W^+W^- \to 2\ell2\nu$ + 2 jets	POWHEG v2 + JHUGen	0.8962	MiNLO
VBF H $\to W^+W^- \to 2\ell2\nu$	POWHEG v2 + JHUGen	0.0896	NLO
ZH (H $\to W^+W^-$) + jet	POWHEG v2 + JHUGen	0.187	NLO
W^+H (H $\to W^+W^-$) + jet	POWHEG v2 + JHUGen	0.1810	NLO
W^-H (H $\to W^+W^-$) + jet	POWHEG v2 + JHUGen	0.1160	NLO
Gluon-gluon fusion (ggF) ZH (H $\to W^+W^- \to 2\ell2\nu$)	POWHEG v2	0.00275257	NLO
ttH (no H $\to b\bar{b}$)	POWHEG v2	0.2120	NLO
ggF H $\to \tau^+\tau^-$	POWHEG v2	2.7757	NLO
Vector boson fusion (VBF) H $\to \tau^+\tau^-$	POWHEG v2	0.2370	NLO
ZH (H $\to \tau^+\tau^-$) + jet	POWHEG v2	0.0550	NLO
W^+H (H $\to \tau^+\tau^-$) + jet	POWHEG v2	0.0532	NLO
W^-H (H $\to \tau^+\tau^-$) + jet	POWHEG v2	0.0341	NLO

Table 4.4: Signal and background MC samples; the third column shows the cross section (σ) times the branching ratio (BR) of the corresponding decay channel.

4.3   Signal modeling

The signal sample is simulated with MadGraph5_aMC@NLO [58] (v. 2.4.2) at LO in QCD perturbative expansion, requiring two quarks and two leptonically decaying W bosons in the final state; contributions from τ decays to lighter leptons are also considered and included in the simulation. Fig. 4.1 shows some typical diagrams at the lowest order in the EW coupling that contribute to the signal process. Among contributions to the EW W^+W^- production, there are some, as the one depicted on the right side of Fig. 4.1, which are not strict VBS diagrams. Nevertheless, in order to preserve the amplitude gauge invariance, they cannot be discarded and, therefore, they are part of the signal definition as well.
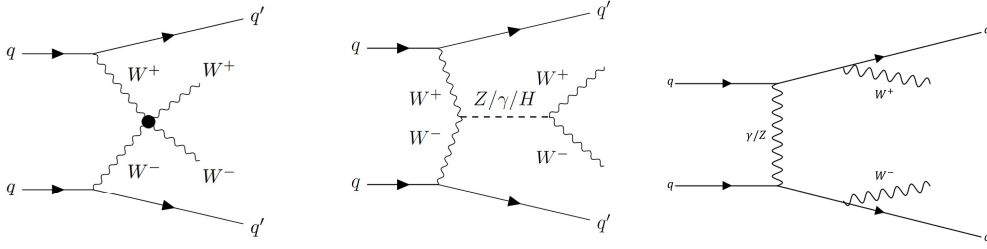
Figure 4.1: Examples of Feynman diagrams for the EW production of W^+W^- bosons in association with two quarks.

Diagrams containing a top quark contribution are not included in the signal matrix element, since EW top quark production is taken into account by the $t\bar{t}$ and single top quark (tW) background samples. W bosons are generated within 15 decay widths from their on-shell mass. The dipole approach is used to model the initial-state radiation, rather than the one used by default in the PYTHIA 8 parton shower algorithm, which was found to not properly describe extra QCD emissions in vector boson fusion (VBF) and VBS processes [59]. More details are given in Sec. 4.3.2.

On-shell VBF Higgs boson production is negligible when simulating two on-shell W bosons, as is done for the signal sample. Accordingly, this contribution is removed from our signal definition, whereas off-shell effects are retained. Furthermore, the signal region phase space is tailored to enhance the EW W^+W^- production occurring without a Higgs boson exchange, which is suppressed by the tight selection on the dilepton invariant mass, as discussed in Sec. 5.1. A dedicated analysis has been designed to target the on-shell VBF Higgs boson production [60], where, conversely, our signal sample is regarded as a background source.

As far as the signal reconstruction is concerned, the CMS detector deeply relies on the kinematic topology of VBS jets. Quarks taking part to VBS diagrams carry away a large fraction of the energy of their mother-proton and are not connected by any color-charge exchange. Because of this, final state jets are typically emitted with high p_T and are well separated in the detector. In this section, these key features are investigated at the level of MC event generators.

4.3.1   Sherpa and MadGraph comparison

In order to verify the validity and robustness of our MC signal sample, I have generated an alternative VBS sample by employing SHERPA 2.2.10 [61]. SHERPA is a general purpose generator software designed for simulating

events in high energy experiments, such as the LHC. The SHERPA framework is a modular event generator, which comprises several packages to describe all components of a scattering event, from the matrix element calculation, to the parton showering, down to the hadronization process. Although being not commonly used within the CMS collaboration, the ATLAS collaboration extensively relies on it, thus representing a perfect validation tool in our case.

The SHERPA event generator produces VBS W^+W^- diagrams at LO in QCD, therefore no α_S couplings are involved, as it also happens to the nominal MADGRAPH sample. The two p_{T}-leading jets are described by the matrix element, jets beyond the second one are instead generated through the SHERPA built-in parton shower CSSHOWER++ [62].

A preliminary generator-level study was performed to quantify the relative contribution of the signal component with respect to the QCD-induced W^+W^- background. To do so, I developed a dedicated analysis routine by using the Rivet package (v. 3.1.2) [63], a library which facilitates comparisons between theoretical predictions and experimental results. In Fig. 4.2, the m_{jj} distribution is shown for the two W^+W^- contributions, including their interference term: the EW W^+W^- production peaks around 1 TeV and then slowly decreases, whereas the QCD background rapidly falls along the m_{jj} spectrum. Besides, the interference term is two orders of magnitude less than the signal sample, hence it will not be considered throughout the following discussion. A summary of the the kinematic requirements used for this and the following studies is presented in Tab 4.5.

In a similar fashion, I compared the SHERPA sample to the nominal one provided by the CMS collaboration. The selection I implemented is described in Sec. 5.1, but replicated with generator-level information. As it can be seen from Fig. 4.3, simulations are in good agreement with each other in the m_{jj} distribution; some discrepancy is visible at high $|\Delta\eta_{\mathrm{jj}}|$ values, which, however, is covered by theoretical uncertainties (not shown in the plot).

4.3.2   Parton shower studies

When looking at kinematic variables related to extra QCD emissions, some undesired behavior is observed. In VBS-like topologies, we expect that the emission of a third jet occurs in the proximity of one of the two VBS jets. The reason of this lies in the purely EW nature of the signal process, which disadvantages the production of hadronic activity between the VBS jets, as they are not connected via any color-charge exchange. This characteristic can be quantified by the Zeppenfeld variable (normalized to $|\Delta\eta_{\mathrm{jj}}|$), which
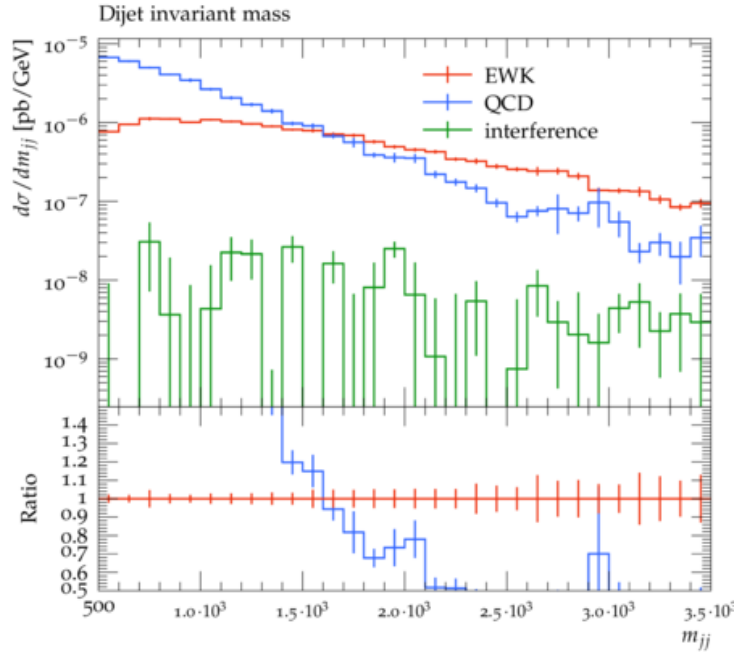
Figure 4.2: m_{jj} distribution as simulated by SHERPA for the EW signal (red line), QCD-induced background (blue line) and their interference (green line). Only eμ final state is taken into account.
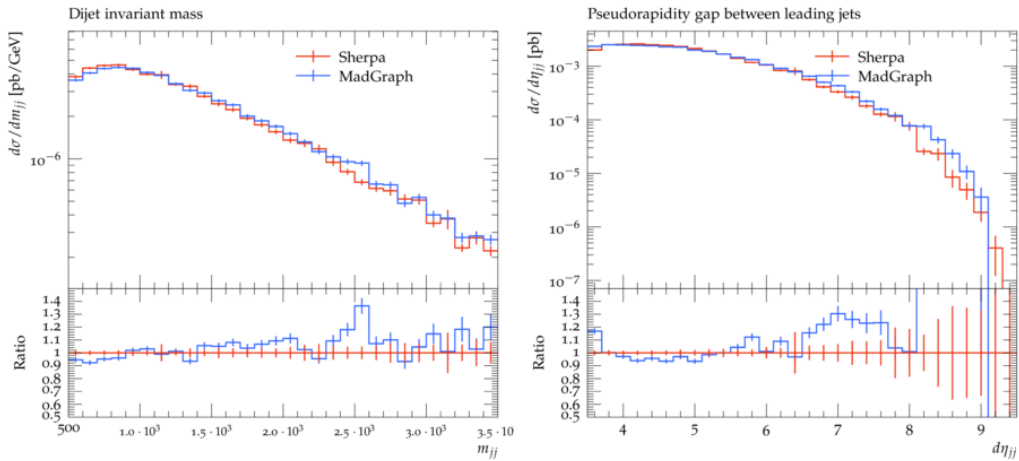

Figure 4.3: m_{jj} (on the left) and $|\Delta\eta_{jj}|$ (on the right) distributions as simulated by SHERPA and MADGRAPH5 event generators for the VBS signal. A good agreement is observed between the two MC event generators in the m_{jj} distribution. All final states are selected in this comparison.

Objects	Requirements
Leptons	eμ (not from τ decay), opposite charge (Figs. 4.2, 4.5)
	eμ, ee, $\mu\mu$ (not from τ decay), opposite charge (Figs. 4.3, 4.4)
	$p_\mathrm{T}^{\mathrm{dressed}\,\ell} = p_\mathrm{T}^\ell + \sum_i p_\mathrm{T}^{\gamma_i}$ if $\Delta\mathrm{R}(\ell, \gamma_i) < 0.1$
	$p_\mathrm{T}^{\ell_1} > 25$ GeV, $p_\mathrm{T}^{\ell_2} > 13$ GeV, $p_\mathrm{T}^{\ell_3} < 10$ GeV
	$\|\eta\| < 2.5$
	$p_\mathrm{T}^{\ell\ell} > 30$ GeV, $m_{\ell\ell} > 50$ GeV
Jets	$p_\mathrm{T}^{j} > 30$ GeV
	$\Delta\mathrm{R}(j, \ell) > 0.4$
	At least 2 jets, no b jets
	$\|\eta\| < 4.7$
	$m_\mathrm{jj} > 500$ GeV, $\|\Delta\eta_\mathrm{jj}\| > 3.5$
$p_\mathrm{T}^{\mathrm{miss}}$	$p_\mathrm{T}^{\mathrm{miss}} > 20$ GeV

Table 4.5: Definition of the generator-level phase space.

can be defined as $Z_{j_3} = \frac{\eta_{j_3} - \frac{1}{2}(\eta_{j_1} + \eta_{j_2})}{|\Delta\eta_\mathrm{jj}|}$. This observable is expected to be close to 0.5, meaning that the third jet tends to be emitted near VBS jets. Fig. 4.4 shows that the Z_{j_3} region between 0 and 0.5 is overly populated for both MC event generators, for different reasons.

For SHERPA, an issue related to the color-connection scheme was found to be there in 2.2.X releases: this feature poorly described third-jet kinematics, and it was corrected since version 3 - only available for test purposes[1]. Similarly, the MADGRAPH signal sample was interfaced to the standard PYTHIA 8 parton shower algorithm, which, whenever a parton branching occurs, assigns the p_T recoil to all final state particles. This approach is not valid anymore when considering VBS processes, where this "global" recoil would introduce unphysical color-flow between incoming partons. An alternative implementation, called "dipole" recoil scheme, was developed to correct for this effect. The impact of these corrections is shown separately in both MC event generators in Fig. 4.5, where the Z_{j_3} observable is now depleted. Even though the choice of parton showering description can deeply modify distributions of extra QCD emissions, this has little effect on inclusive

---

[1]At the time this study was performed. The color-connection issue has been solved since version 2.2.12.
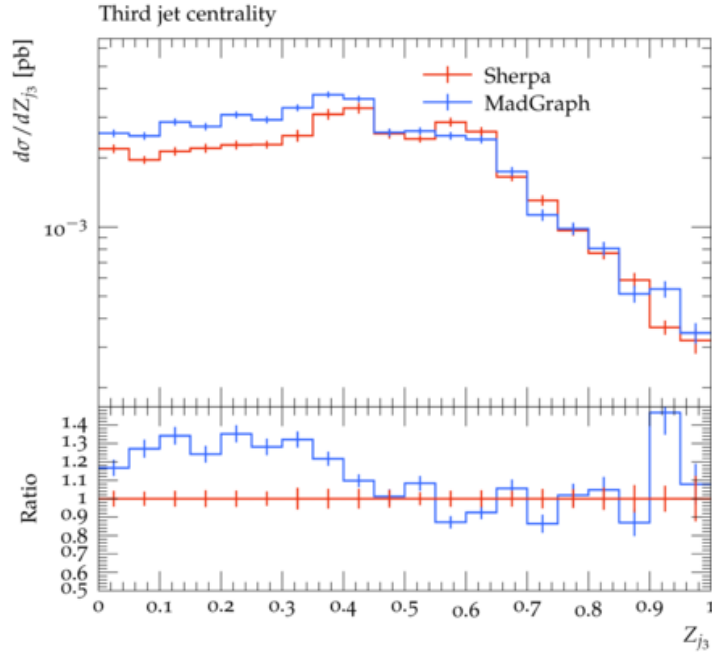
Figure 4.4: Z_{j_3} distribution as simulated by SHERPA and MADGRAPH5 event generators for the VBS signal.

dijet variables, as it is demonstrated in Fig. 4.5 for the m_{jj} observable.

Ultimately, we resorted using the MADGRAPH sample interfaced to the dipole recoil parton shower. This configuration was extensively validated and ensures a good description of the VBS kinematic topology, as discussed in this section. The two different parton shower settings were also compared to each other by looking at detector-level observables, selecting events from potential signal candidates (see Sec. 5.1). As shown in Fig. 4.6, dijet inclusive observables (first and second row) are slightly affected by the dipole approach and are almost uncorrelated with respect to third-jet related variables (third row), which instead are those most sensitive to the parton shower event evolution. All plots include the overflow bin, whereas the underflow bin is only populated when a third jet is not found in the event.
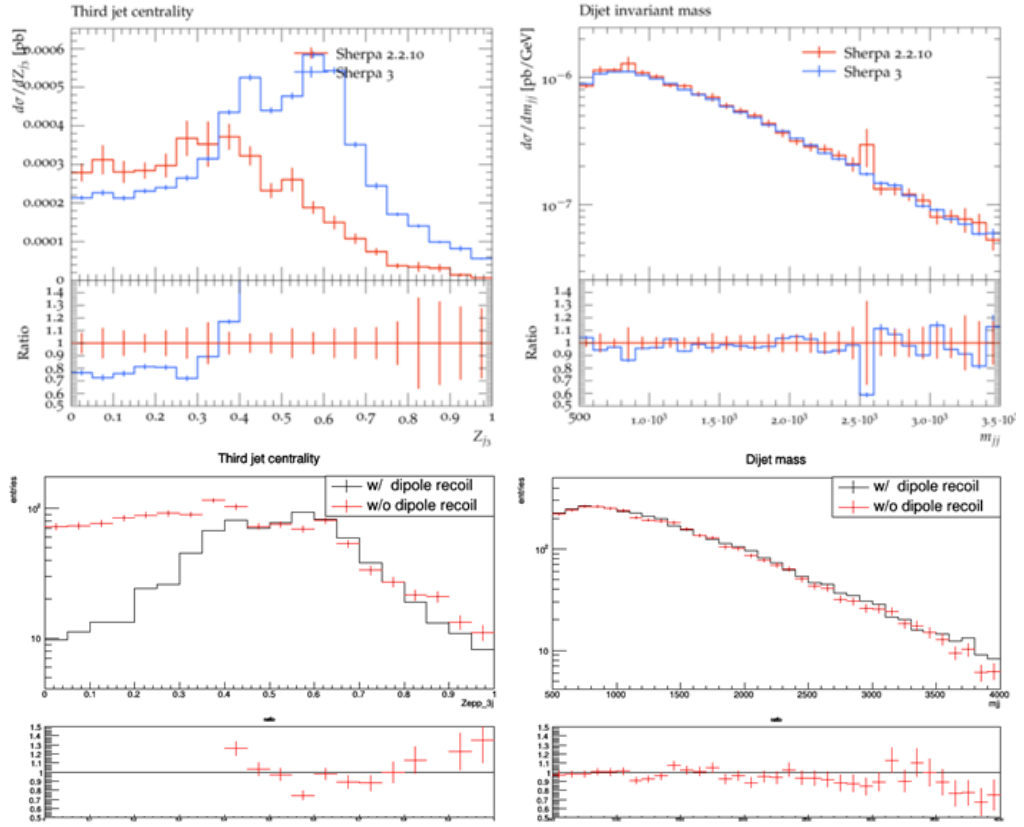
Figure 4.5: Z_{j_3} distribution as simulated by SHERPA (top left) and MAD-GRAPH5 (bottom left) event generators for the VBS signal. In both figures, the effect of parton shower correction is clearly visible. Likewise, the m_{jj} distribution is also shown for SHERPA (top right) and MADGRAPH5 (bottom right), where the effect of parton shower correction has almost no impact.
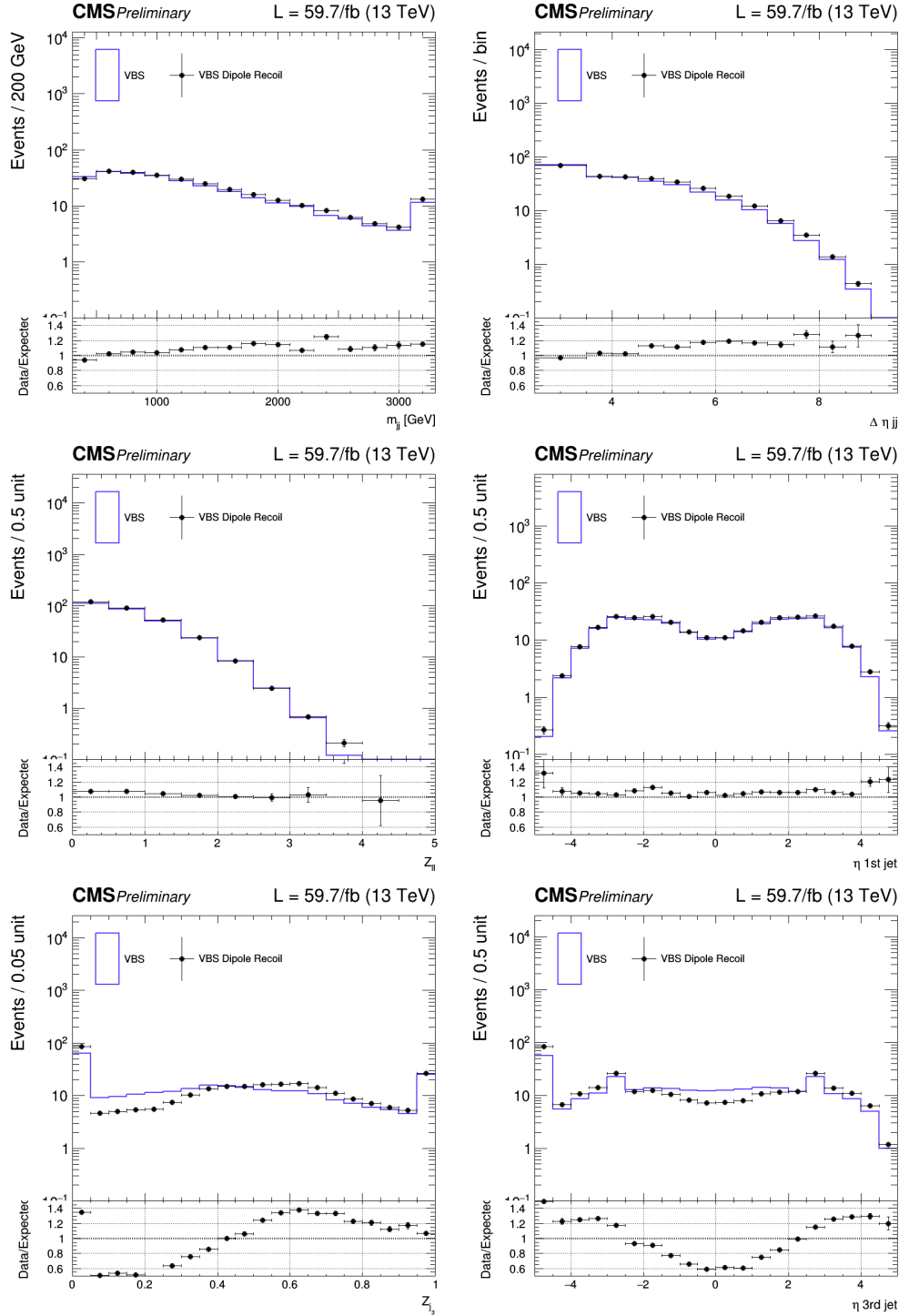
Figure 4.6: Comparison between different parton shower algorithms applied to MADGRAPH signal samples as taken from 2018 MC simulation; first row: dijet mass of the two VBS jets, pseudorapidity gap of the two tagging jets; second row: η of the first jet and $Z_{\ell\ell}$; third row: Z_{j_3} and η of the third jet. The second panel in each plot shows the ratio between dipole recoil and standard signal samples.

4.4   Background modeling

Background processes either share the exact same final state as the VBS signal (irreducible backgrounds), or give rise to configurations that may be misidentified as events of interest (reducible backgrounds). Reducible backgrounds are due to multiple causes, such as particles produced out of the CMS detector acceptance, misassignment in the physics object definition by identification algorithms and finite detector resolution. In this analysis, several background sources have been considered and will be presented in this Section.

4.4.1   Top quark production

The largest background contribution to this analysis is given by top quark production, in particular from $t\bar{t}$ diagrams, schematically depicted in Fig. 4.7. Top quarks immediately decay through weak interactions by emtting a b quark and a W boson with almost 100% probability; b quarks hadronize in b jets, and W bosons can decay leptonically, thus giving a similar final state to the VBS signal. Although this process does not constitute an irreducible background, because of the presence of two b jets, b tagging algorithms leave some room for a b jet to be misidentified as a jet coming from a light quark, and vice versa. This, combined with the huge $t\bar{t}$ production cross section, is what makes this process so difficult to suppress and it must be determined with uttermost precision.
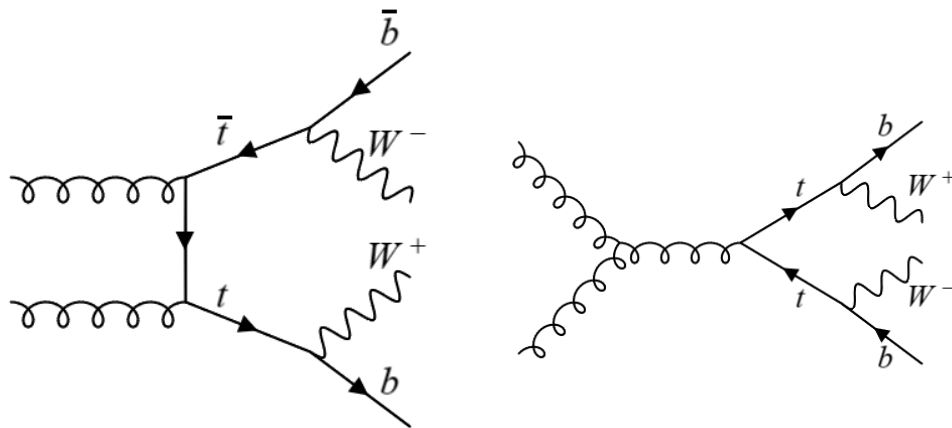

Figure 4.7: Feynman diagrams for $t\bar{t}$ production with two jets coming from b quarks.

$t\bar{t}$ and tW productions are both simulated with POWHEG v2 at NLO precision, and the p_T distribution of the $t\bar{t}$ component, which also represents the dominant background source of the analysis, is further reweighted to better match data, where this spectrum is found to be softer than what predicted by most of the event generators [64].

4.4.2 QCD-induced W^+W^-

The QCD-induced W^+W^- bosons production constitutes an irreducible background for this analysis, in case the two W bosons each decay into a lepton and a neutrino, and two jets come from initial state radiation, as illustrated in Fig. 4.8. Nevertheless, the m_{jj} distribution greatly helps in distinguishing this contribution from the EW signal, as preliminary shown in Fig. 4.2,

QCD-induced W^+W^- background is modeled with POHWEG v2 [65], and the production of the second parton is described at LO accuracy in QCD. The interference between this term and the signal was evaluated, and it results in a negligible effect; some studies of W^+W^- production in association with two jets are presented in Sec. 5.2.2. The gluon-induced component of the W^+W^- background is simulated with the MCFM [66] event generator at NLO precision. Henceforth, both processes will be referred to as QCD-induced W^+W^- background, and no distinction will be made between the two, unless otherwise stated.
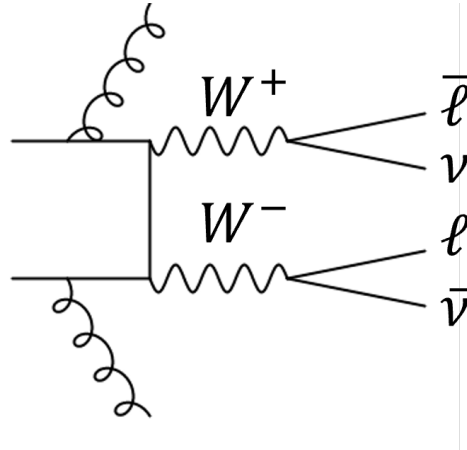

Figure 4.8: Feynman diagrams for QCD-induced W^+W^- production with two jets coming from initial state radiation.

Since a reliable MC simulation is needed for this critical background sample, I compared different MC event generators for the study of QCD production of two W bosons in association with two jets - the gluon-induced W^+W^-

component is not considered for this purpose. To do so, a LO W^+W^- plus exactly two emitted partons MadGraph sample and an inclusive NNLO W^+W^- POWHEG sample were considered. In both cases, the radiated parton with the second-highest p_T in the event is simulated at LO in QCD perturbative calculation, therefore this represents a fair comparison. However, the MadGraph sample lacks of genuine 0- and 1-jets contributions: these events may indeed only enter the signal selection at the reconstruction-level if either the jet-clustering algorithm is not capable of finding two jets above the required p_T-threshold or detector smearing effects cause bin-migration to low jet-multiplicity bins. In Fig. 4.9, the m_{jj} distribution is drawn for the two samples.
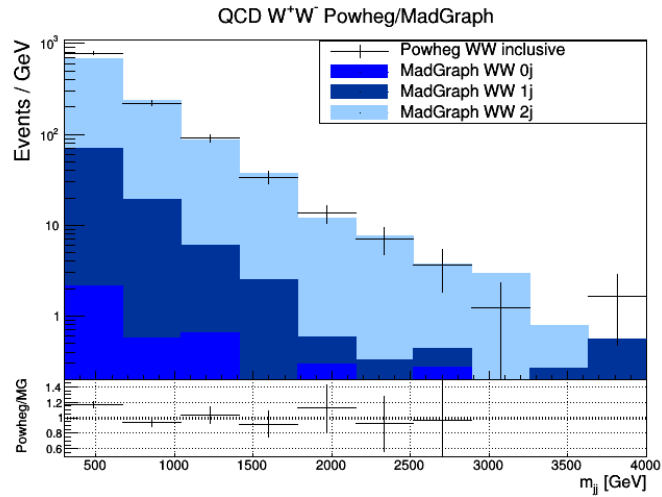

Figure 4.9: Comparison between POWHEG (data points) and MadGraph (stacked blue histograms) W^+W^- samples. The MadGraph sample is shown as a function of the number of generated jets, whereas the POWHEG sample is shown inclusively. A mild disagreement is observed in the very first bin of the m_{jj} distribution.

Although they do not differ much within their statistical uncertainties, a mild discrepancy is observed in the very first bin. To investage the origin of such a disagreement, I have separated 0-, 1- and 2-or-more jets contributions at generator-level, as illustrated in Fig. 4.10. While m_{jj} distributions are in excellent agreement with each other in the 2-jets bin, it is evident how the discrepancy comes indeed from events generated with either 0 or 1 jet at generator-level. For this reason, we resorted employing the POWHEG sample.
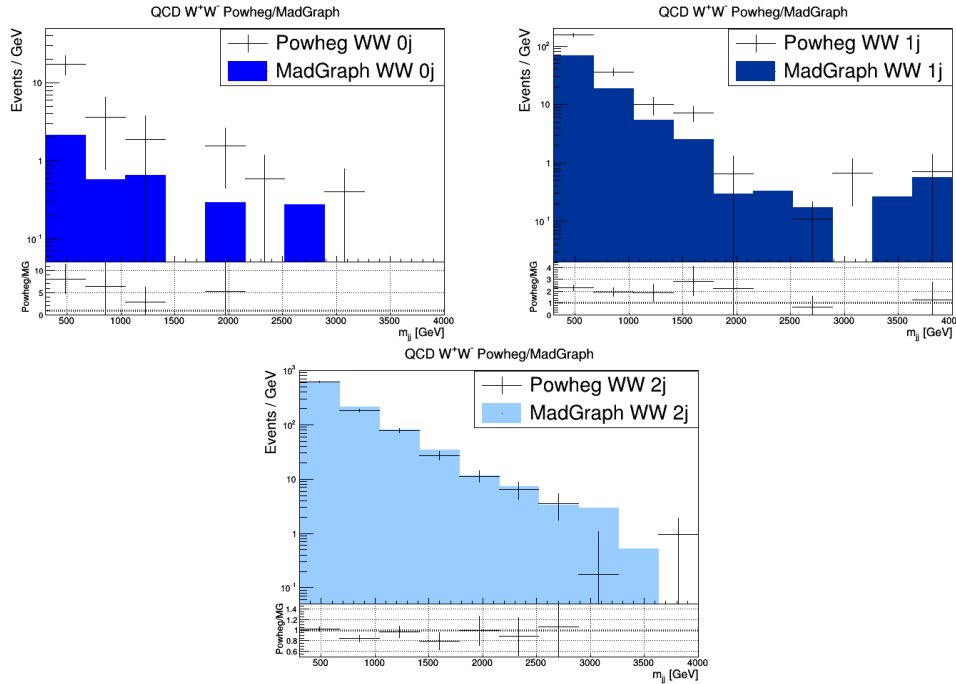
Figure 4.10: Comparison between POWHEG (data points) and MAD-GRAPH (blue histograms) W^+W^- samples, as a function of the number of generated jets. In the exclusive 0-jet (top left) and 1-jet (to right) bins, the POWHEG sample is more populated, meaning that these events are not negligible in the SR. m_{jj} distributions nicely agree with each other when selecting two or more jets in the final state (bottom).

4.4.3   DY

Another background source is given by Drell-Yan (DY) events, occurring when a $q\bar{q}$ pair annihilates into a γ or Z boson, which then decays into two oppositely-charged same flavor leptons. As for the QCD-induced W^+W^- background, the two final state jets come from initial state radiation. Two distinct set of samples are employed to simulate this process, depending on the considered channel.

In the $e\mu$ final state, tha sole DY contribution comes from $Z/\gamma^* \to \tau^+\tau^-$ events, because of the possible subsequent τ leptons decay into a different-flavor lepton pair, along with their corresponding neutrinos. The associated typical Feynamn diagram is shown in Fig. 4.11. This process is estimated with a data-driven method called "embedding" technique [67], which will be discussed in Sec. 5.2.3. Since the "τ-embedded" sample contains all processes which may have $\tau^+\tau^-$ leptons decaying into an electron-muon pair as a final
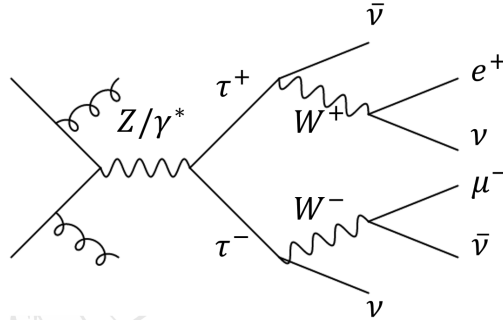
Figure 4.11: Feynman diagrams for $Z/\gamma^* \to \tau^+\tau^-$ production with two jets coming from initial state radiation.

state, this contribution is removed from other background samples to avoid double counting. In order to consider DY events that might fail electron-muon triggers but still pass single-lepton triggers, $\tau^+\tau^-$ leptons pair selected in this way are instead simulated by MadGraph5_aMC@NLO with up to two extra jets at NLO QCD precision, where the FxFx scheme [68] is used to merge exclusive jet multiplicities. Such residual events constitutes about $\approx 13\%$ of the total DY contribution to the eμ channel.
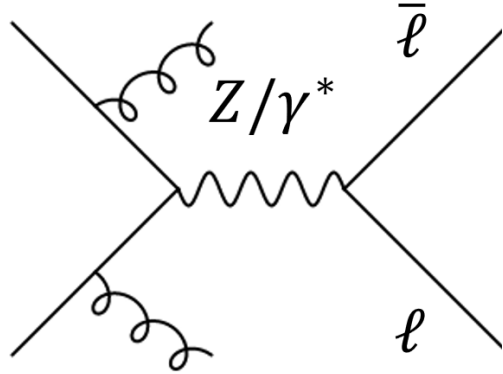
Figure 4.12: Feynman diagrams for $Z/\gamma^* \to \ell^+\ell^-$ production with two jets coming from initial state radiation, where ℓ represents a light lepton (either e or μ).

In ee and $\mu\mu$ final states, a dedicated ensemble of MC simulation is used to model the DY background. The finite detector resolution and acceptance may indeed cause to reconstruct these events with $p_T^{\mathrm{miss}} \neq 0$, faking the presence of neutrinos. Indeed, this is what makes a difference between the $Z/\gamma^* \to \ell^+\ell^-$ diagram in Fig. 4.12 and that of Fig. 4.11. Since the fraction of DY events with at least two jets and passing the tight selection applied in

signal region is small, HT-binned samples are used instead of an individual inclusive sample, which would not have the necessary MC event statistics. The HT observable is defined as the scalar sum of all partons p_T as generated by the matrix element calculation. Therefore, high HT values are strongly correlated with high jet multiplicities in the final state, which are those mainly entering the analysis selection. These samples are simulated with MadGraph5_aMC@NLO at LO precision and their cross section is weighted to match the NLO prediction. The full set of DY samples included in ee and $\mu\mu$ categories is listed in Table 4.6, which integrates Table 4.4. The lower limit in the HT binning is either 70 GeV or 100 GeV, depending on the selected dilepton mass window: below this value, inclusive NLO (LO) DY samples are employed in the $m_{\ell\ell} > 50$ GeV (10 GeV $< m_{\ell\ell} < 50$ GeV) phase space at generator-level.

Process	MC event generator	$\sigma \times$BR [pb]	QCD order
DY inclusive background samples			
Z/$\gamma^* \to \ell^+\ell^-$ + jets (10 GeV $< m_{\ell\ell} < 50$ GeV)	MadGraph5_aMC@NLO	18610.0	LO
Z/$\gamma^* \to \ell^+\ell^-$ + jets ($m_{\ell\ell} > 50$ GeV)	MadGraph5_aMC@NLO	6189.39	NLO
DY HT-binned background samples, 4 GeV $< m_{\ell\ell} < 50$ GeV			
Z/$\gamma^* \to \ell^+\ell^-$ + jets (100 GeV $<$ HT < 200 GeV)	MadGraph5_aMC@NLO	204.00	LO
Z/$\gamma^* \to \ell^+\ell^-$ + jets (200 GeV $<$ HT < 400 GeV)	MadGraph5_aMC@NLO	54.39	LO
Z/$\gamma^* \to \ell^+\ell^-$ + jets (400 GeV $<$ HT < 600 GeV)	MadGraph5_aMC@NLO	5.697	LO
Z/$\gamma^* \to \ell^+\ell^-$ + jets (HT > 600 GeV)	MadGraph5_aMC@NLO	1.85	LO
DY HT-binned background samples, $m_{\ell\ell} > 50$ GeV			
Z/$\gamma^* \to \ell^+\ell^-$ + jets (70 GeV $<$ HT < 100 GeV)	MadGraph5_aMC@NLO	208.98	LO
Z/$\gamma^* \to \ell^+\ell^-$ + jets (100 GeV $<$ HT < 200 GeV)	MadGraph5_aMC@NLO	181.30	LO
Z/$\gamma^* \to \ell^+\ell^-$ + jets (200 GeV $<$ HT < 400 GeV)	MadGraph5_aMC@NLO	50.42	LO
Z/$\gamma^* \to \ell^+\ell^-$ + jets (400 GeV $<$ HT < 600 GeV)	MadGraph5_aMC@NLO	6.984	LO
Z/$\gamma^* \to \ell^+\ell^-$ + jets (600 GeV $<$ HT < 800 GeV)	MadGraph5_aMC@NLO	2.704	LO
Z/$\gamma^* \to \ell^+\ell^-$ + jets (800 GeV $<$ HT < 1200 GeV)	MadGraph5_aMC@NLO	1.681	LO
Z/$\gamma^* \to \ell^+\ell^-$ + jets (1200 GeV $<$ HT < 2500 GeV)	MadGraph5_aMC@NLO	0.775	LO
Z/$\gamma^* \to \ell^+\ell^-$ + jets (HT > 2500 GeV)	MadGraph5_aMC@NLO	0.186	LO

Table 4.6: List of DY samples used in ee and $\mu\mu$ categories: for each of those, the third column shows the cross section (σ) times the branching ratio (BR) of the decay channel, expressed in pb.

4.4.4 Other backgrounds

Higgs boson production mechanisms are included in the analysis and treated as a background source: all production modes are simulated with POWHEG v2 at NLO accuracy in QCD. Gluon-gluon fusion (ggF) events are further reweighted to match NNLO accuracy, according to the NNLOPS scheme [69]. The Higgs boson decay into two W bosons and subsequently into leptons is simulated with the JHUGen generator [70], whereas its decay into two

τ leptons is simulated with PYTHIA 8; other minor Higgs boson decay channels have been neglected.

Other minor background processes are included in the analysis, such as EW Z boson production in association with two jets, Wγ, Zγ, diboson and multiboson channels; all of them are simulated at NLO precision in QCD calculation, except for the EW Z boson production plus two jets and the Wγ background.

Chapter 5

Analysis strategy

This Chapter describes in detail the analysis strategy I used to select signal candidates and measure the cross section of the VBS process in $W^+W^- \to 2\ell2\nu$ final state. Kinematic selections, background estimation, systematic uncertainties and signal extraction procedure will be presented in here.

5.1 Event selection

Before any categorization, candidate signal events are selected if they fulfill the following VBS-like criteria:

- **Lepton preselection:** Two oppositely-charged and isolated leptons (electrons or muons), reconstructed as described in Secs. 3.2 and 3.3. The thresholds for the leading and trailing leptons are 25 and 13 GeV, respectively. The acceptance region for electrons is given by the $|\eta| <$ 2.5 requirement, whereas for muons is $|\eta| < 2.4$;

- **Extra lepton veto:** No additional leptons with $p_T > 10$ GeV beyond the second one must be found in the event;

- **Dilepton selection:** Specific kinematic requirements are applied to the two-lepton system selected in the event. The dilepton invariant mass $m_{\ell\ell}$ must satisfy $m_{\ell\ell} > 50$ GeV to reduce contributions from on-shell Higgs boson production, and this threshold is raised up to 120 GeV when selecting same-flavor leptons, in order to further suppress the DY background contribution. Moreover, the candidate leptons pair must have a transverse momentum $p_T^{\ell\ell} > 30$ GeV to discard $Z/\gamma^* \to \tau^+\tau^-$ and W+jets background events.

- **Missing transverse momentum:** $p_T^{miss} > 20$ GeV to select a final state with neutrinos. As for the $m_{\ell\ell}$ selection, this requirement is increased up to 60 GeV to reject DY events when two same-flavor leptons are selected;

- **Jet selection:** Signal candidates are selected from events with at least two jets having $p_T > 30$ GeV and passing the tight jet ID working point;

- **VBS-like selection:** The two leading jets in the event, i.e., those with the highest p_T, must also pass VBS-like selections to enhance the signal contribution and reduce other backgrounds. In particular, they are required to have $m_{jj} > 300$ GeV and $|\Delta\eta_{jj}| > 2.5$; this was found to be a good compromise between signal efficiency and background rejection.

Events passing these selctions are still dominated by $t\bar{t}$ pair production, where the two W bosons produced by top quark decays emit two charged leptons and two neutrinos, thus mimicking the VBS signal. The two b quarks generated in this decay chain can be misidentified as VBS jets. To increase the signal purity, the kinematic phase space is then divided in signal (SRs) and control regions (CRs), which are all included in the maximum-likelihood template fit procedure performed to extract the signal cross section (see Sec. 5.6). SRs are defined in order to enhance the signal component and suppress as much as possible background contributions. Conversely, CRs are used to check the agreement between data and simulation and estimate and constrain the normalization of the main background processes, i.e., $t\bar{t}$ + tW and DY production. Each region is further categorized according to the charged lepton flavor composition: two electrons (ee), two muons ($\mu\mu$), or one electron and one muon (eμ).

The SR is defined by requiring that no b jets, defined with the loose working point of the DeepJet algorithm [48], are present. The transverse mass m_T is defined as $m_T = \sqrt{2p_T^{\ell\ell}p_T^{miss}\left[1 - \cos\Delta\phi(\vec{p_T}^{\ell\ell}, \vec{p_T}^{miss})\right]}$, where ϕ is the azimuthal angle in radians; m_T is required to be above 60 GeV in the eμ SR, where only a residual DY contribution (from $\tau^+\tau^- \to$ eμ events) remains. Additionally, the SR is split into two regions to optimize the signal significance. Such a splitting is based on the centrality of the dilepton system with respect to the VBS jets, quantified by the so-called Zeppenfeld variable [71] $Z_{\ell\ell} = \frac{1}{2}|Z_{\ell_1} + Z_{\ell_2}|$, where $Z_\ell = \eta_\ell - \frac{1}{2}(\eta_{j_1} + \eta_{j_2})$ with η_ℓ, η_{j_1}, and η_{j_2} being the pseudorapidities of the lepton and the two jets, respectively. SRs are separated around $Z_{\ell\ell} = 1$: indeed, most of the signal events falls in the $Z_{\ell\ell} < 1$ category ($\approx 70\%$), whereas background events evenly populate

the two regions. Ultimately, the analysis sensitivity is driven by the former category.

Top CRs ($t\bar{t}$ + tW) are defined by inverting the b jet veto, thus requiring the presence of at least one b jet with $p_T > 20$ GeV in the final state, and dropping the m_T selection; in DY CRs, the b veto requirement is the same as that in the SR. In the DY eμ category, the m_T requirement is reversed with respect to the SR and a 50 GeV $< m_{\ell\ell} < 80$ GeV window is selected. In DY ee and $\mu\mu$ categories, the dilepton mass is chosen to be close to the Z boson mass peak, $|m_{\ell\ell} - m_Z| < 15$GeV. Moreover, the DY ee and $\mu\mu$ CRs are divided in two $|\Delta\eta_{jj}|$ bins, as explained in Sec. 5.2.3. A summary of the full event categorization is given in Table 5.1.

Region	Final state	Requirements	Subregion
SR	eμ/μe	$m_T > 60$GeV	$Z_{\ell\ell} < 1$
		$m_{\ell\ell} > 50$GeV	$Z_{\ell\ell} > 1$
		no b jet with $p_T > 20$GeV	
	ee		$Z_{\ell\ell} < 1$
		$m_{\ell\ell} > 120$GeV	$Z_{\ell\ell} > 1$
		$p_T^{miss} > 60$GeV	
	$\mu\mu$	no b jet with $p_T > 20$GeV	$Z_{\ell\ell} < 1$
			$Z_{\ell\ell} > 1$
top CR	eμ/μe	$m_{\ell\ell} > 50$GeV	
		at least one b jet with $p_T > 20$GeV	
	ee	$m_{\ell\ell} > 120$GeV	
		$p_T^{miss} > 60$GeV	
	$\mu\mu$	at least one b jet with $p_T > 20$GeV	
DY CR	eμ/μe	$m_T < 60$GeV	
		50GeV $< m_{\ell\ell} < 80$GeV	
		no b jet with $p_T > 20$GeV	
	ee		$|\Delta\eta_{jj}| < 5$
		$|m_{\ell\ell} - m_Z| < 15$GeV	$|\Delta\eta_{jj}| > 5$
		$p_T^{miss} > 60$GeV	
	$\mu\mu$	no b jet with $p_T > 20$GeV	$|\Delta\eta_{jj}| < 5$
			$|\Delta\eta_{jj}| > 5$

Table 5.1: Summary of the event categorization on top of signal candidates preselection. In each region, same-flavor final states share the same kinematic requirements.
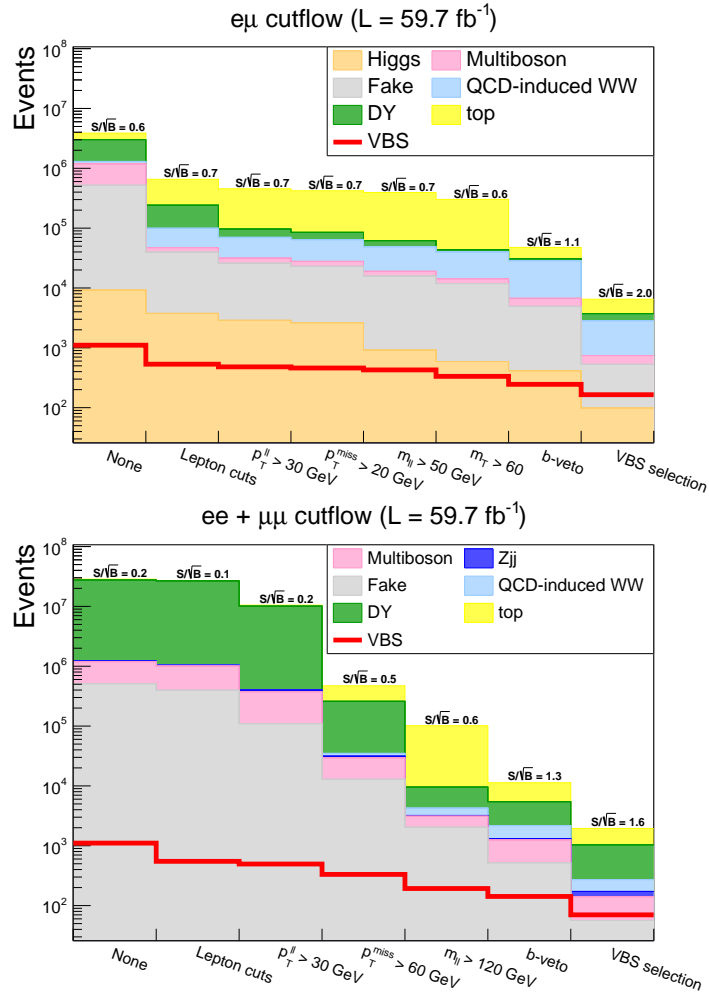
Figure 5.1: Effect of kinematic requirements on signal candidates taken from MC samples, corresponding to the simulation of the data-taking year 2018 (59.74 fb^{-1}). On the top (bottom), the different (same) flavor category is shown. The signal is represented by a superimposed red line, whereas background samples are stacked on top of each other. As expected, the eμ final state has a greater sensitivity with respect to same-flavor channels.

Fig. 5.1 shows the expected statistical significance for a counting experiment, as a function of the kinematic selection applied to signal candidates, evaluated as the number of signal events over the square root of total background events. The two plots are drawn separately for different and same flavor final states, and obtained from the 2018 simulated MC samples, corresponding to an integrated luminosity of 59.74 fb^{-1}. In the first bin, labeled as "None", only two tight leptons with $p_{\mathrm{T}} > 10$ GeV are required and no

other selection is applied. Moving towards the right along the x-axis, the effect of each selection is sequentially illustrated, and the highest sensitivity is reached in the last bin of the eμ category. None of the uncertainties included in the analysis is taken into account here, a more precise calculation of the expected significance will be shown in Chap. 6.

5.2 Background estimation

The normalizations of the main background processes are not taken from simulated samples, but rather they are measured when performing the signal extraction by a simultaneous fit of both SRs and CRs to data. In this section, data-driven methods used to estimate such background sources are presented. Minor background contributions not mentioned in this section are estimated through MC simulation, as they have little impact in the signal extraction procedure.

5.2.1 Top quark production

The top background normalization is scaled by a parameter which is left to float freely during the fit procedure, whereas the shape of the corresponding MC histogram is taken from the POWHEG simulation [72]. Therefore, this parameter is constrained by data measured in the top CR, enriched in contributions from top quarks. Since the top CR is kinematically indentical to the SR, except for the reversed condition of the b jet veto requirement, this method ensures a good estimation of the top quark contribution entering the SR.

5.2.2 QCD-induced W$^+$W$^-$

Conversely to the strategy for measuring the normalization of t$\bar{\text{t}}$ and DY backgrounds, it is very difficult to tailor a CR enriched in QCD-induced W$^+$W$^-$ events. In this analysis, the production of two W bosons through diagrams involving QCD couplings consitutes one of the main backgrounds, if two additional jets are emitted along with them. This mechanism is an irreducible background, but it has a much smaller cross section if compared to t$\bar{\text{t}}$ pair production. Therefore, defining a CR by just reverting the m_{jj} requirement of the SR would not be enough to select a pure W$^+$W$^-$ sample, since such a phase space would still be dominated by t$\bar{\text{t}}$ contribution. The normalization of QCD-induced W$^+$W$^-$ background is then measured "by difference" in the very SR: given that both t$\bar{\text{t}}$ and DY contributions are

essentially constrained in their respective CRs, only two degrees of freedom are left, one for the VBS signal and another one for the W^+W^- background. As it will be discussed in Sec. 5.3, the variables we choose to extract the VBS cross section have a powerful discriminating power between signal and backgrounds, thus there is no degeneracy in the determination of these two independent parameters. An alternative approach would have been taking the QCD-induced W^+W^- background normalization directly from MC simulation, but this was found to not improve the accuracy of background estimation, when adding the corresponding theoretical uncertainty necessary for this method.

5.2.3   DY

In the ee and $\mu\mu$ categories, DY production is one of the leading background sources, typically arising when a lepton pair is reconstructed with significative p_T^{miss} due to instrumental effects, faking the presence of neutrinos in the final state. Therefore, tight $m_{\ell\ell}$ and p_T^{miss} selections are applied in SRs to suppress this background, as described in Table 5.1. However, with this configuration, a large fraction of DY events ($\approx 50\%$) comes from cases where at least one of the two jets originates from a pileup vertex; the remaining DY contribution is instead associated with the "hard" interaction, in which the two highest p_T jets are radiated by initial-state partons. Given their diverse nature, we decide to treat these backgrounds as two independent processes, and measure them with different parameters when performing the maximum-likelihood fit. Hence, the normalization of the DY background is determined from separated CRs with $|\Delta\eta_{jj}| < 5$, dominated by events where jets originate from initial-state QCD radiation, and $|\Delta\eta_{jj}| > 5$, dominated by events where at least one of the two highest p_T jets comes from a pileup interaction.

   The reason of this splitting also lies in a mild discrepancy observed when looking at the $|\Delta\eta_{jj}|$ distribution in the inclusive DY CRs, where ee and $\mu\mu$ categories are merged, which is ultimately reflected in some disagreement between data and MC in the m_{jj} observable. The idea is then correcting this mismodeling by fitting pileup and hard jets as two independent contributions, in order to readjust the inclusive m_{jj} observable. Pre-fit plots of individual yearly data set are shown in Fig. 5.2 for the $|\Delta\eta_{jj}|$ and m_{jj} observables, respectively, whereas full Run 2 distributions are reported in Fig. 5.3.

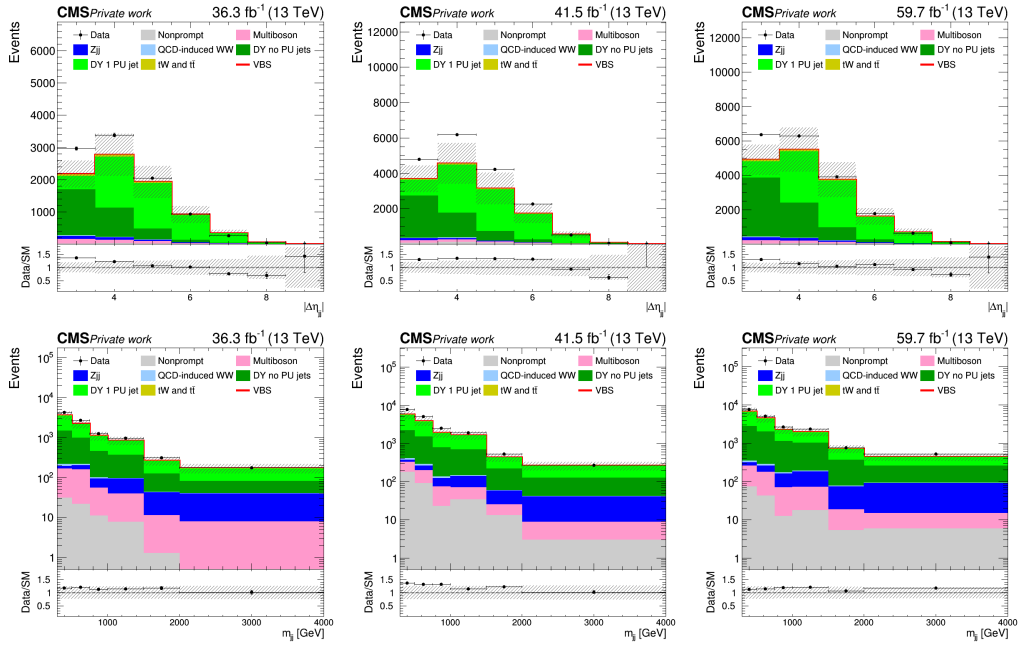Figure 5.2: Pre-fit m_{jj} (top) and $|\Delta\eta_{\mathrm{jj}}|$ (bottom) distribution in the inclusive DY CR from the 2016 (left), 2017 (center) and 2018 (right) data sets, respectively.
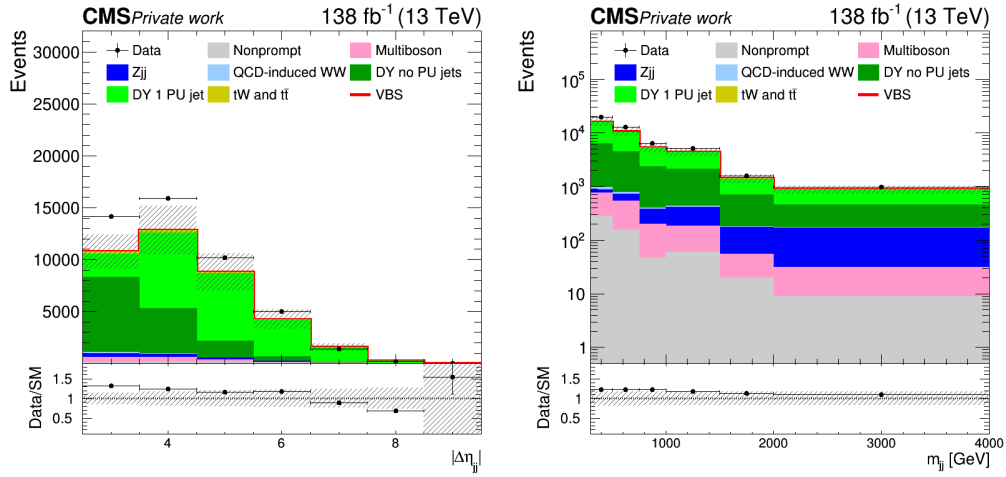

Figure 5.3: Comparison of observation and prediction in the inclusive DY CR from the full Run 2 data set of pre-fit $|\Delta\eta_{\mathrm{jj}}|$ (left) and m_{jj} (right) distributions.

In this context, a pileup jet is defined as a reconstructed jet which is not matched to any corresponding jet having $p_T > 25$ GeV and belonging to the generator-level objects collection. The correlation between high p_T^{miss} and number of pileup jets in DY events can be clearly seen in Fig. 5.4: plots show the pileup contribution for primary background processes as a function of the p_T^{miss} threshold in the ee and $\mu\mu$ SRs combined, where all other selections are fixed. Because the DY background is the only one without neutrinos in this final state, the non-zero p_T^{miss} observable is mainly due to pileup jets that pass the signal selection and constitute an increasing fraction of DY events. On the other hand, QCD-induced W^+W^- and $t\bar{t}$ backgrounds, as well as the signal process, come with real neutrinos, therefore, in this case, such a contribution is much smaller and independent of the p_T^{miss} threshold.
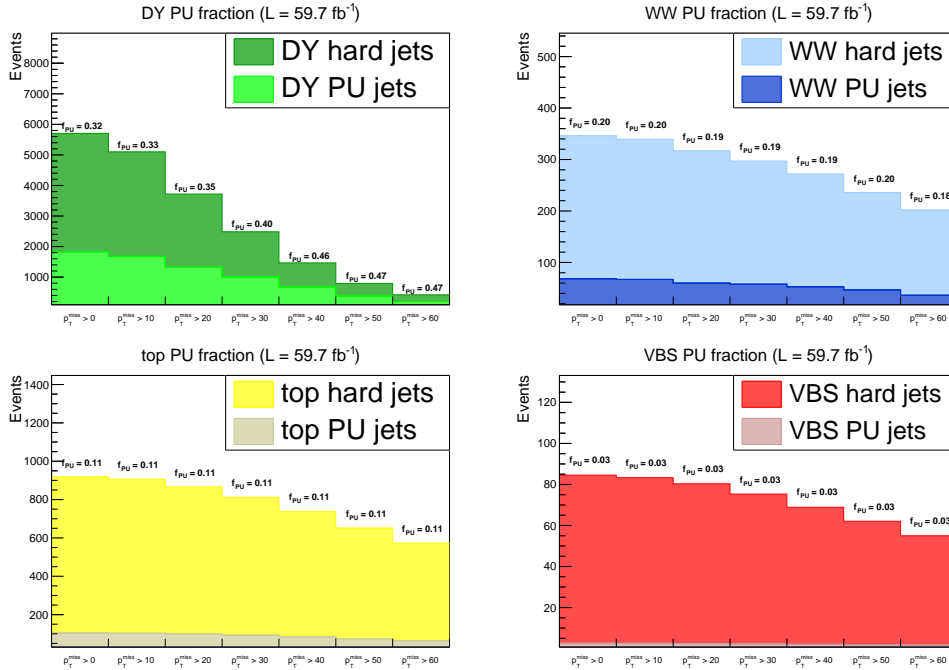
Figure 5.4: Fraction of pileup jets as a function of the p_T^{miss} threshold. This number strongly depends on the p_T^{miss} selection in the ee and $\mu\mu$ categories when considering the DY background (top left), whereas this is not the case for QCD-induced W^+W^- (top right) and top (bottom left) backgrounds and it is completely negligible in the VBS signal (bottom right).

A similar trend is visible in MC simulations of 2016 and 2017 data sets: although the average number of pileup vertices is less than that recorded in 2018, the fraction of pileup jets in DY events heavily relies on detector reconstruction performances, which are year-dependent. Indeed, as illustrated

in Fig. 5.5, these fractions are even higher if compared to the 2018 data set.

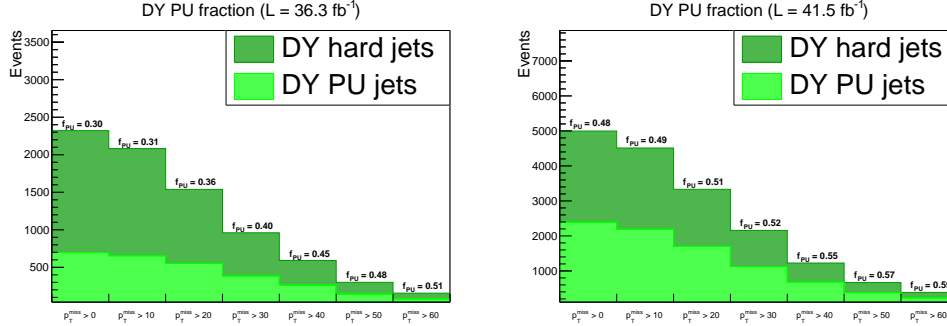
Figure 5.5: Fraction of pileup jets as a function of the p_T^{miss} threshold for DY events in 2016 (left) and 2017 (right) MC simulations.

Another minor source of DY contribution is due to $Z/\gamma^* \to \tau^+\tau^-$ events, whose MC prediction is obtained through the procedure discussed below. In this case, genuine p_T^{miss} arises from neutrinos, because of τ leptons decays. Therefore, there is no need to make such a distinction as it is done in ee and $\mu\mu$ categories. This process is estimated with a data-driven method called embedding technique [67]. A subset of well-identified $\mu^+\mu^-$ events are selected from data using electron-muon triggers and replaced with simulated τ leptons, keeping their kinematics unchanged: this τ-embedded sample is further corrected to take into account discrepancies with data due to τ lepton simulation. This method is advantegeous because, on the one hand, it provides a better description of the observables that are sensitive to detector calibration, such as p_T^{miss}, and, on the other, it overcomes the limitation due to the finite size of MC sample statistics in simulating DY to $\tau^+\tau^- \to e^\pm \mu^\mp 4\nu$ final state, which would otherwise require a huge amount of events to be generated. A third parameter is then used to determine the normalization of this background, which only enter $e\mu$ categories. DY events that fail electron-muon triggers but pass single-lepton triggers are instead estimated entirely from MC simulation.

5.2.4   Non-prompt leptons

Events in which a single W boson is produced in association with jets may populate the SR when one of these jets is misidentified as a lepton. Furthermore, leptons originating from a displaced vertex are typically given by B-hadrons decays within a jet, or in case a pion is misreconstructed as a lepton. As mentioned in Secs. 3.2.2 and 3.3.2, these processes constitute a

background source that might enter the SR, and are generally referred to as non-prompt leptons. The capability of correctly describing these events heavily relies on detector performances, thus it is not feasible to accurately simulate them through standard MC techniques. A more valid and trustworthy approach is to extract non-prompt leptons estimation from data, as it will be discussed in this section.

The basic idea to evaluate the amount of non-prompt leptons entering the SR is to compute a suitable transfer function from a sample known to be almost entirely populated by these events. This function is then applied to a CR where one of the two leptons must fail tight requirements used in the SR, but still passes loose identification and isolation working points. The CR is tailored to select W + jets events, which ultimately represents one of the main non-prompt leptons source.

A QCD-enriched control sample is used to measure the rate of objects f satisfying loose lepton criteria that also pass tight lepton criteria, as defined for the SR. The control sample is selected with triggers requiring either one electron and one jet or a single muon. In both cases, the lepton must be well separated from the highest p_T jet and a $p_T^{miss} < 20$ GeV threshold is set to suppress prompt leptons originating from a W boson decay. A minor prompt leptons contribution is given by the EW production of a Z boson, which is estimated from MC simulation and removed from the control sample.

Finally, the transfer function is an event-by-event weight and calculated as $\frac{1}{1-f}$, where the probability of a prompt lepton to not pass the tight working point is also taken into account. The transfer function is derived as a function of the object's p_T and η, and data entering the W + jets CR are then weighted to give the prediction of non-prompt leptons in the SR.

The estimation of the non-prompt lepton background is cross-checked in an auxiliary validation region, where two leptons with the same charge are required. In fact, this region is expected to be mainly populated by events where either the electric charge is misassigned to leptons or jet are misidentified as leptons. Fig. 5.6 shows the distribution of the lepton with the second-highest p_T in the event, i.e., the one having the greatest probability to be faked by a jet, for each possible flavor composition. Validation regions are not kinematically close to SRs, since they lack of VBS-like selections, which dramatically reduce the non-prompt lepton contribution. Uncertainties arise mainly from the different flavor composition of the jets faking the leptons in the region used to estimate the non-prompt leptons rate and the application regions, and they are included in the uncertainty band in Fig. 5.6. A detailed description of these sources is presented in Sec. 5.5.1. Data and MC simulation reasonably agree within their uncertainties.
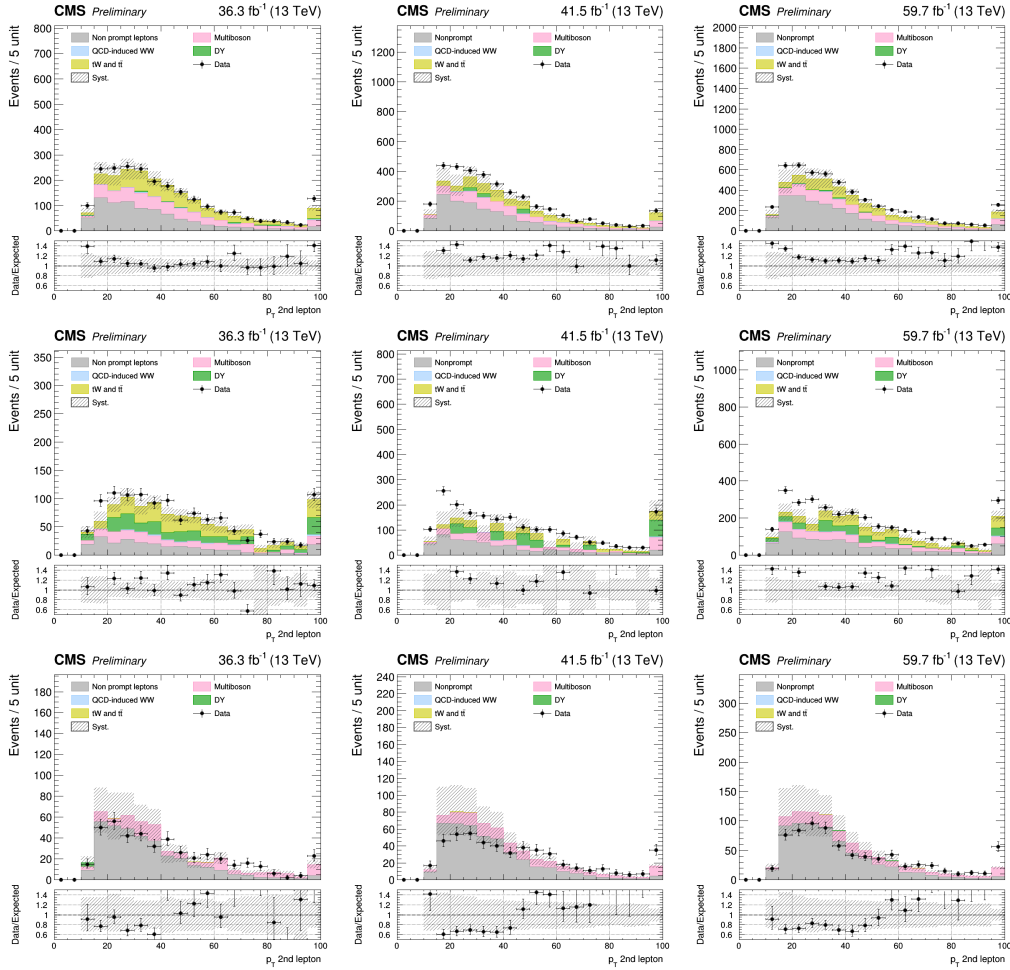
Figure 5.6: Closure test for non-prompt leptons in a control region where two leptons with the same charge are required. The p_T distribution of the lepton with the second-highest p_T in the event is shown for the eμ, ee and $\mu\mu$ final states in the first, second and third row, respectively. From left to right: 2016 (left), 2017 (center) and 2018 (right) data sets.

5.3   Discriminating variables

The goal of this work is to take advantage of the full Run 2 data set to perform the measurement of the EW W^+W^- production cross section. To do so, it is crucial to design kinematic observables that are able to clearly distinguish between the signal process and all other background contributions.

The path we walked to reach the observation of this rare process started with a close scrutiny of the eμ category, which was expected to have enough

potential to achieve this purpose. As a matter of fact, the good signal-to-background ratio of the eμ channel, combined with the large amount of data collected from 2016 to 2018 by the CMS collaboration, is what drives the sensitivity of the VBS cross section measurement. Studies in Sec. 4.3 demonstrate how the m_{jj} observable is a good candidate to isolate signal events from background ones: indeed, the QCD-induced W^+W^- sample, together with $t\bar{t}$ pair production and other backgrounds, shows a rapidly falling distribution, whereas the VBS signal peaks around 1 TeV and then slowly decreases. Bins at high m_{jj} values are dominated by signal contributions, giving a desirable histogram for the likelihood function.

To further improve our strategy, we opted for a different approach, based on the usage of a Deep Neural Network (DNN). A DNN is a machine learning (ML) algorithm that takes several variables as inputs and operate non-linear transformations on them, finally resulting in a scalar output. This output is a floating point number spanning a range between 0 and 1, and can be interpreted as the probability of each event to belong to a given category. Since in our case we fed the DNN with signal and background events, the DNN score is the probability of each event to be signal. The DNN training procedure works in an iterative way, until it converges: starting from a random guess, weights defining non-linear transformations are readjusted to better match the expected output - 1 for signal events and 0 for background events. A cost function - often called as "loss" function - is minimized with respect to such set of weights at each iteration step in order to get closer to the true predicted value. The advantage of employing a DNN score rather than a standard kinematic variable is that the former can learn hidden correlations among inputs, and thus exploit all the available information to generate a more powerful discriminating variable.

For optimization purposes, different DNN models were built in the sub-regions with low ($Z_{\ell\ell} < 1$) and high ($Z_{\ell\ell} > 1$) values of the Zeppenfeld variable. The two models share the same architecture and input variables, listed in Table 5.2. The DNN implementation comprises five fully connected hidden layers, the first two (last three) having 128 (64) nodes each, that are trained with the stochastic gradient descent technique of the "Adam" optimizer tool [73] to achieve a good separation of signal and backgrounds. A binary cross-entropy loss function [74, 75] is minimized in both models.

In the eμ SR, the m_{jj} distribution is then replaced with a DNN output, obtained from the training procedure described above. Therefore, bins with high DNN values will be enriched in VBS-like events, whereas background samples will mostly populate the low DNN spectrum. Statistically independent set of MC simulations are used to train and validate the DNN machinery, which aims at distinguishing the VBS signal from $t\bar{t}$ pair production

Variable	Description
m_{jj}	Invariant mass of the two tagging jets pair
$p_T^{j_1}$	p_T of the highest p_T jet
$|\Delta\eta_{jj}|$	Pseudorapidity separation between the two tagging jets
$p_T^{j_2}$	p_T of the second-highest p_T jet
Z_{ℓ_2}	Zeppenfeld variable of the second-highest p_T lepton
$p_T^{\ell\ell}$	p_T of the lepton pair
$\Delta\phi_{\ell\ell}$	Azimuthal angle between the two leptons
Z_{ℓ_1}	Zeppenfeld variable of the highest p_T lepton
$m_T^{\ell_1}$	Transverse mass of the ($p_T^{\ell_1}$, p_T^{miss}) system

Table 5.2: Set of variables used as inputs to the DNN for both $Z_{\ell\ell} < 1$ and $Z_{\ell\ell} > 1$ models. The order in the table corresponds to the discriminating importance of the variable for the $Z_{\ell\ell} < 1$ model.

and QCD-induced W^+W^- background processes. Normalized distributions of input variables are shown in Figs. 5.7 and 5.8 for the $Z_{\ell\ell} < 1$ and $Z_{\ell\ell} > 1$ categories, respectively, and the DNN output distribution is shown in Fig. 5.9.

In order to exploit the full potential of the VBS final state, ee and $\mu\mu$ SRs are included as well in this analysis. In doing this, one must tackle the large DY background contamination entering such a phase space and devise a suitable strategy to cope with it. As discussed in Sec. 5.1, ee and $\mu\mu$ categories are tailored to suppress as much as possible contributions from DY events. To achieve a good separation between signal and background events in same-flavor categories, a finer distinction is made. We identify a "loose" and a "tight" VBS SR: the former, dominated by background samples, is divided into three bins for each flavor composition (ee and $\mu\mu$) and $Z_{\ell\ell}$ category ($Z_{\ell\ell} < 1$ and $Z_{\ell\ell} > 1$), the number of events in each region being the discriminating variable. The bins are defined as follows:

- $300 < m_{jj} < 500\text{GeV}$ and $2.5 < |\Delta\eta_{jj}| < 3.5$;

- $m_{jj} > 500\text{GeV}$ and $2.5 < |\Delta\eta_{jj}| < 3.5$;

- $300 < m_{jj} < 500\text{GeV}$ and $|\Delta\eta_{jj}| > 3.5$.

In the latter, where the signal-to-background ratio is the largest, the m_{jj} distribution is used instead as fitting variable. In fact, the strict signal selection of ee and $\mu\mu$ categories make backgrounds more difficult to model with
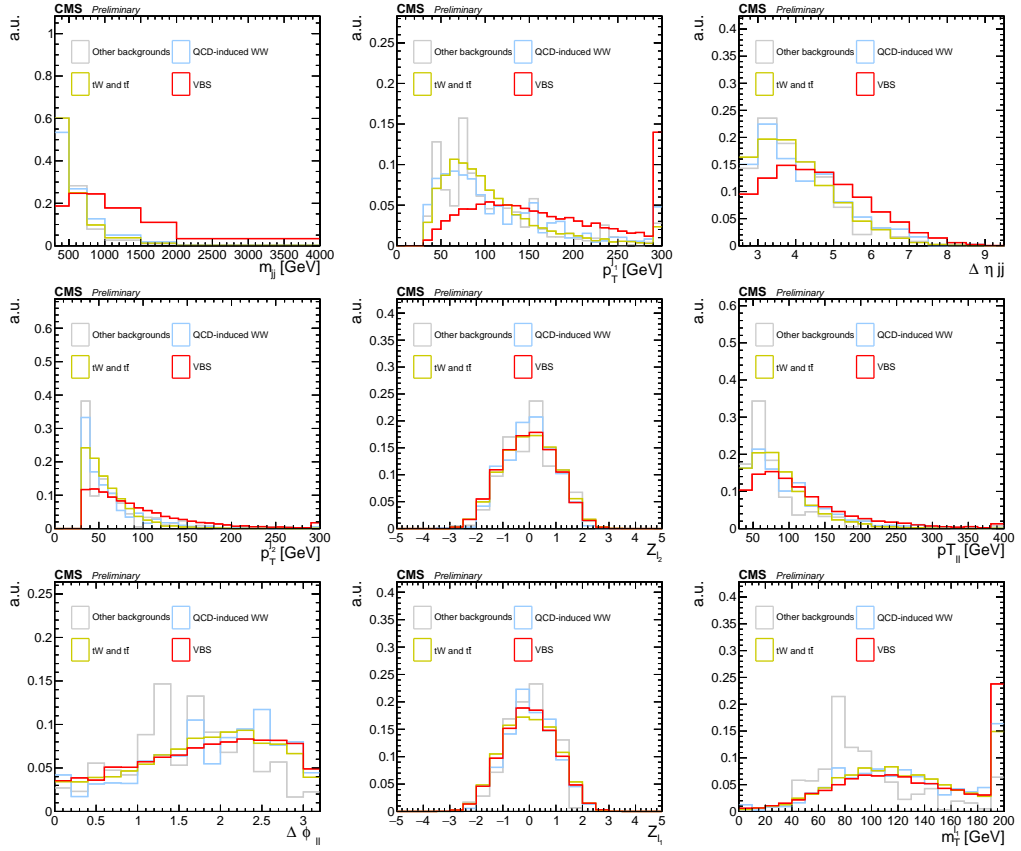
Figure 5.7: Normalized distributions of input variables in the $Z_{\ell\ell} < 1$ category.

respect to those in eμ categories, especially the $Z/\gamma^* \to \ell^+\ell^-$ contribution because of the high p_T^{miss} and $m_{\ell\ell}$ thresholds, as discussed in Sec 5.2.3. For this reason, we rely on simple kinematic distributions, such as the number of events and the m_{jj} observable, to extract the signal in this phase space, rather than using a multivariate approach that could enhance discrepancies in background modeling from input variables to the output score. Ultimately, the methodology described in Sec 5.2.3 is not ensured to correct for possible disagreements between data and MC in complex observables that depend on multiple kinematic features, and this is why we decided to not extend the DNN to same flavor categories.

The binning choice of the DNN (m_{jj}) distribution is optimized category-wise and per data taking year, such that at least two (one) signal events - if present - and a total of five (four) background events are found in each bin of the histograms in eμ (ee and $\mu\mu$) categories. Moreover, the MC statistical
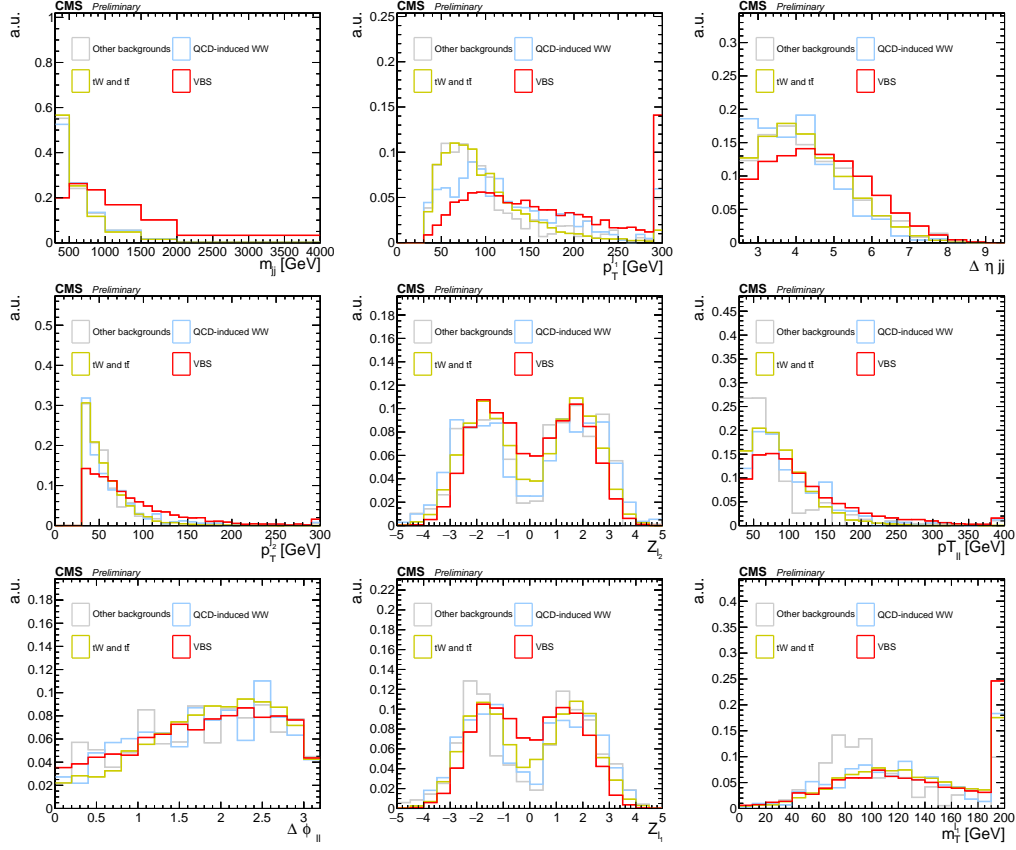
Figure 5.8: Normalized distributions of input variables in the $Z_{\ell\ell} > 1$ category.

uncertainty in background samples is required to be at most 30% of the total background yield in each bin: assuming a Poissonian distribution (see Sec 5.6), this is equivalent to require at least 9 generated background events per bin. Combining individual bins from the loose VBS SR and the m_{jj} distribution from the tight VBS SR, together with the DNN output outlined in eμ categories, gives enough statistical power to make the first observation of EW W^+W^- production. Pre-fit SRs are presented in Fig. 5.10 and 5.11, where the DNN output and m_{jj} distributions are shown, respectively. For the sake of simplicity, loose VBS SRs are embedded in the left-most bin of the m_{jj} histogram in each corresponding flavor and $Z_{\ell\ell}$ category. Uncertainty bands include pre-fit contributions described in Sec 5.5. Full Run 2 pre-fit distributions are shown in Fig. 5.12 and 5.13, and Table 5.3 shows their corresponding yields and uncertainties.
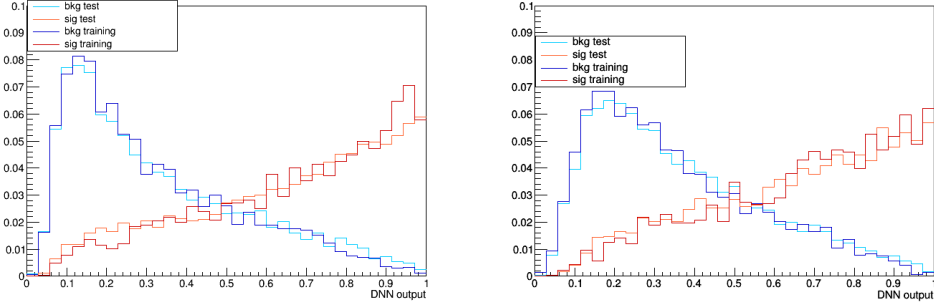
Figure 5.9: DNN output distributions for training (dark colors) and validation (light colors) data set in the $Z_{\ell\ell} < 1$ (on the left) and $Z_{\ell\ell} > 1$ (on the right) categories.
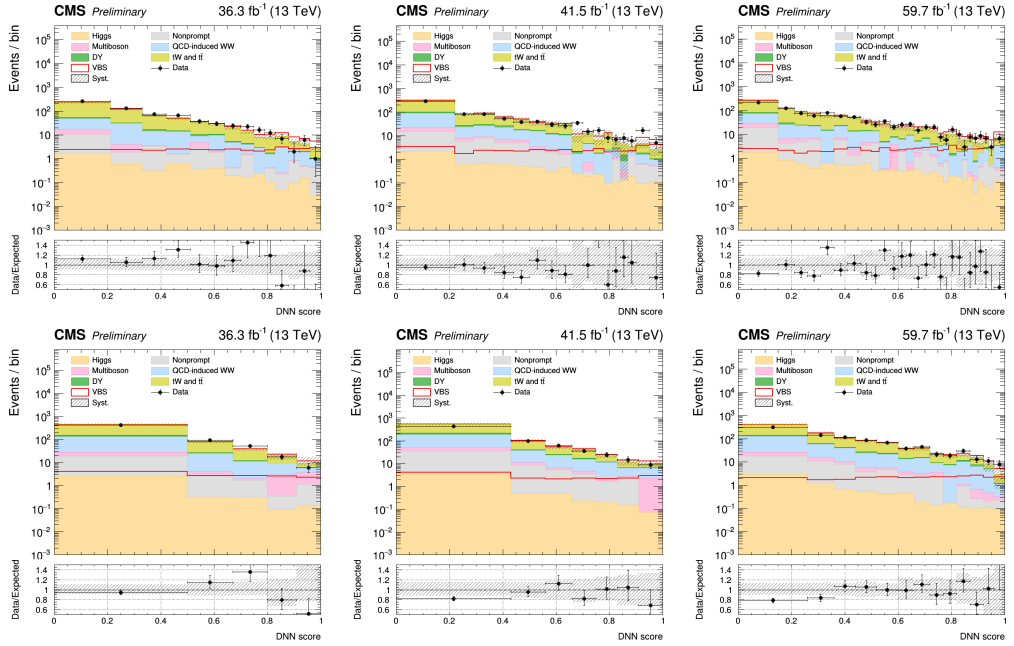
Figure 5.10: Observation and prediction in eμ SRs of 2016 (left), 2017 (center) and 2018 (right) data sets. The DNN output distribution is shown in the $Z_{\ell\ell} < 1$ ($Z_{\ell\ell} > 1$) category in the first (second) row.
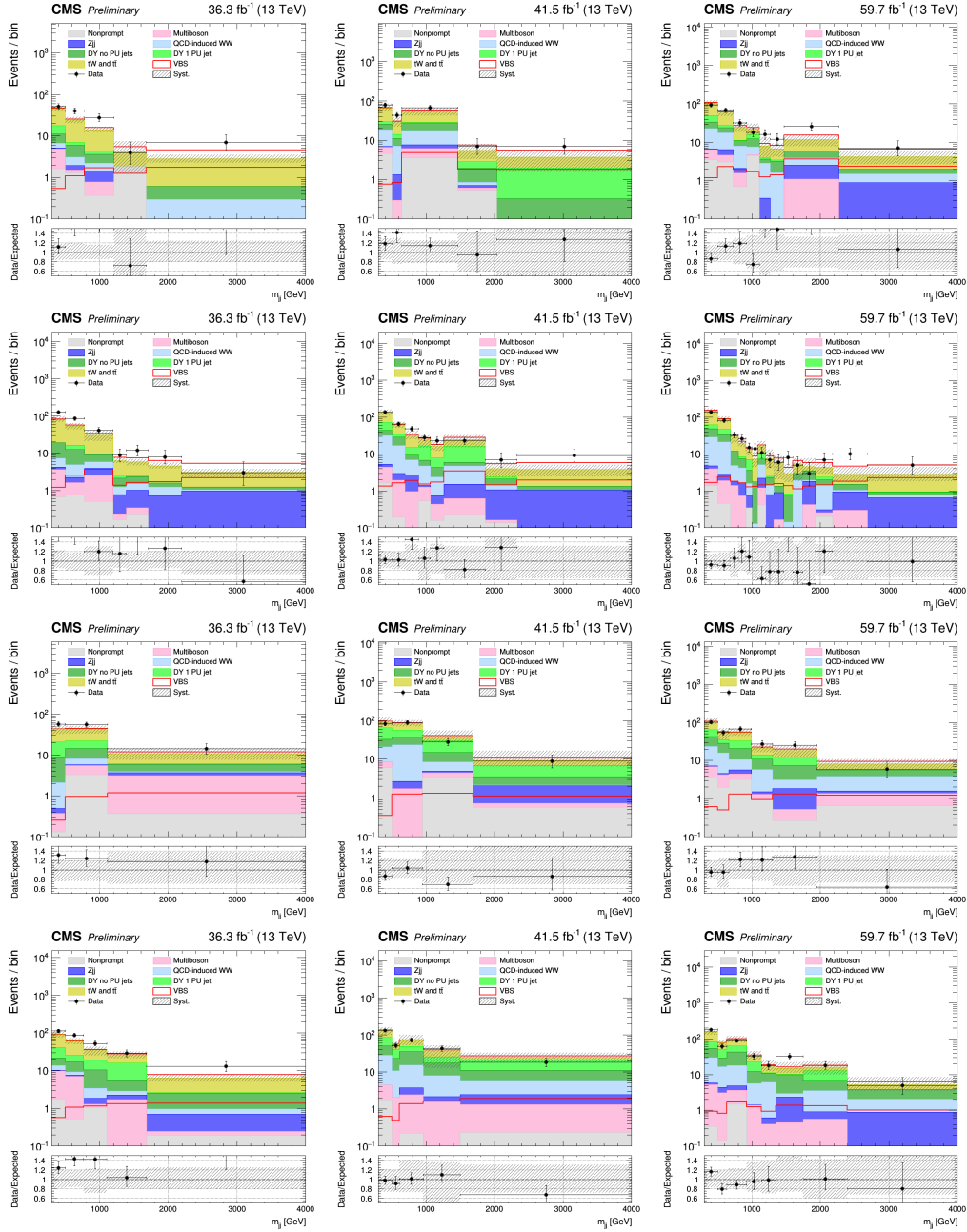
Figure 5.11: Observation and prediction in ee and $\mu\mu$ SRs of 2016 (left), 2017 (center) and 2018 (right) data sets. The m_{jj} distribution is shown in the $Z_{\ell\ell} < 1$ ($Z_{\ell\ell} > 1$) category in the first and second (third and fourth) rows for the ee and $\mu\mu$ final states, respectively. The left-most bin of each histogram embeds all loose VBS SRs together for that specific category.

| Process	SR eμ $Z_{\ell\ell} < 1$	SR eμ $Z_{\ell\ell} > 1$	SR ee/$\mu\mu$ $Z_{\ell\ell} < 1$	SR ee/$\mu\mu$ $Z_{\ell\ell} > 1$
DATA	2441	2192	1606	1667
Signal + background	2499.4 ± 151.8	2418.3 ± 148.5	1475.0 ± 114.3	1632.7 ± 87.5
Signal	148.0 ± 5.0	61.1 ± 2.1	85.5 ± 2.0	33.2 ± 0.9
Background	2351.4 ± 151.7	2357.2 ± 148.5	1389.5 ± 114.3	1599.5 ± 87.5
$t\bar{t}$ + tW	1578.5 ± 135.0	1419.5 ± 132.8	728.6 ± 27.1	589.3 ± 24.3
QCD-induced W$^+$W$^-$	481.8 ± 62.6	605.0 ± 63.3	230.3 ± 17.8	251.3 ± 20.8
Nonprompt	119.6 ± 26.1	122.9 ± 17.9	32.6 ± 6.2	37.3 ± 5.6
DY no PU jets	–	–	173.1 ± 33.5	281.8 ± 23.0
DY + 1 PU jets	–	–	149.3 ± 103.9	361.3 ± 77.6
Z/$\gamma^* \to \tau^+\tau^-$	79.3 ± 4.5	116.6 ± 4.3	–	–
Multiboson	66.3 ± 13.0	74.7 ± 9.2	41.8 ± 4.2	59.8 ± 6.7
EWK Z + 2j	0.9 ± 0.3	0.3 ± 0.0	33.8 ± 6.3	18.8 ± 2.0
Higgs	24.9 ± 2.6	18.2 ± 1.2	–	–

Table 5.3: Pre-fit process yields and uncertainties in each SR (ee and $\mu\mu$ final states combined).
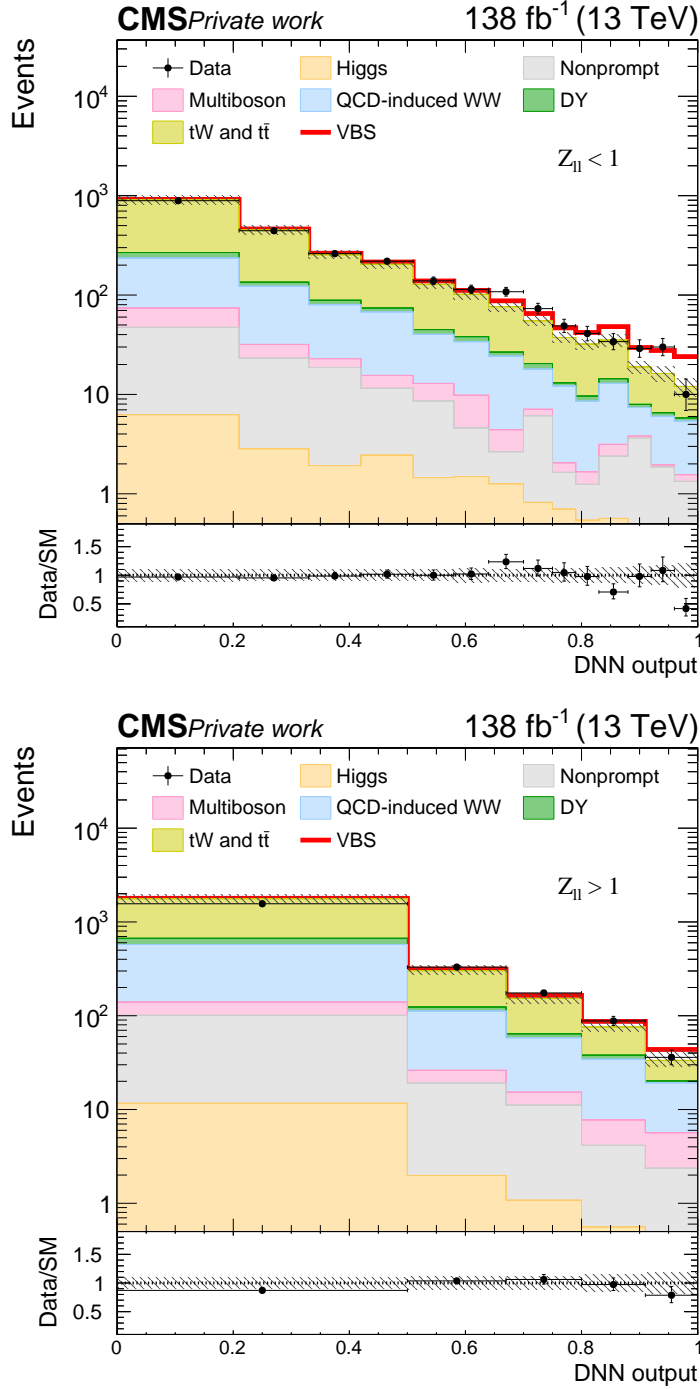
Figure 5.12: Pre-fit DNN output distribution in different-flavor SRs for $Z_{\ell\ell} < 1$ (top) and $Z_{\ell\ell} > 1$ (bottom) categories. This variable quantifies how likely each event is signal. The contributions from background and signal (red line) processes are shown as stacked histograms; systematic uncertainties are plotted as dashed gray bands.
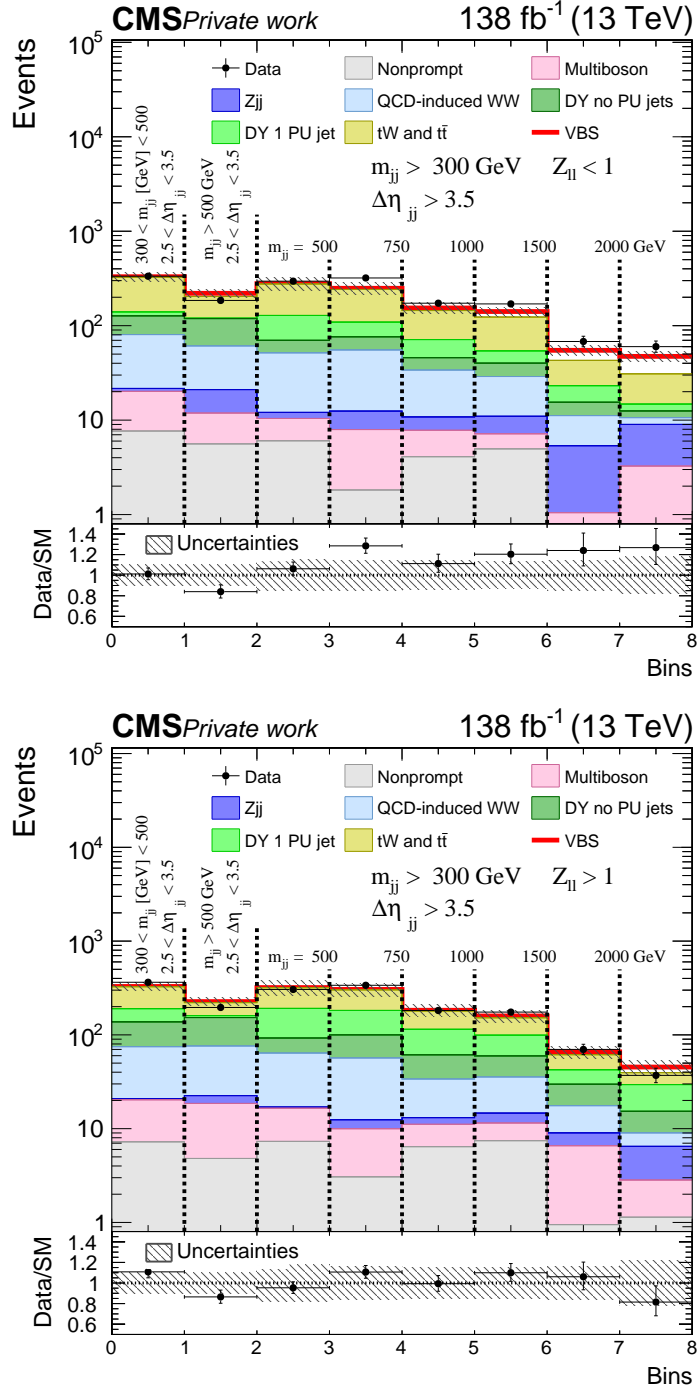
Figure 5.13: Pre-fit m_{jj} distribution and number of events in ee and $\mu\mu$ combined SRs for $Z_{\ell\ell} < 1$ (top) and $Z_{\ell\ell} > 1$ (bottom) categories. The first two bins contain the number of events in the selected region (as reported in the plots themselves). The third bin contains the number of events in the $300 < m_{jj}$ [GeV] < 500 and $|\Delta\eta_{jj}| > 3.5$ regions and, for display purposes, is included in the m_{jj} distribution, shown in the last five bins. The contributions from background and signal (red line) processes are shown as stacked histograms; systematic uncertainties are plotted as dashed gray bands.

5.4   Control regions

As anticipated in Sec 5.1, CRs are introduced to check the agreement of MC simulation with data and, most importantly, measure the normalization of main background processes entering the SR. To the former end, distributions of discriminating variables are shown for both simulated samples and data in all CRs before looking at data in SRs. This is part of a blinding procedure, which allows one to correct for any mismodeling in the background description without being biased by distributions in SRs. When the procedure is validated, data are "unblinded" in SRs too, and the full-analysis fit is performed. The number of events in all CRs are included in the maximum-likelihood fit as individual bins to constrain the corresponding background yield to data: in this way, a reliable estimation of their contributions to the SR is achieved. Figs. 5.14 and 5.15 show pre-fit distributions of some relevant kinematic variables in the eμ, ee and $\mu\mu$ top CRs, respectively. The ratio of data over MC predictions is compatible with 1 within systematic uncertainties for several variables of interest across the three data sets. Uncertainty bands include pre-fit contributions described in Sec 5.5. Similarly, Figs. 5.16, 5.17 and 5.18 include the same set of plots, with the additional splitting over the $|\Delta\eta_{jj}|$ variable in ee and $\mu\mu$ DY CRs. The discrepancy between data and MC mentioned in Sec. 5.2.3 is more visible here, because the DY contribution from pileup jets is separated from hard scattering events. Inclusive post-fit distributions will be presentend in Chap. 6, where the agreement between data and MC simulations is finally restored. Full Run 2 pre-fit number of events in CRs are shown in Fig. 5.19 in eμ (top plot) and ee and $\mu\mu$ combined categories (bottom plot).
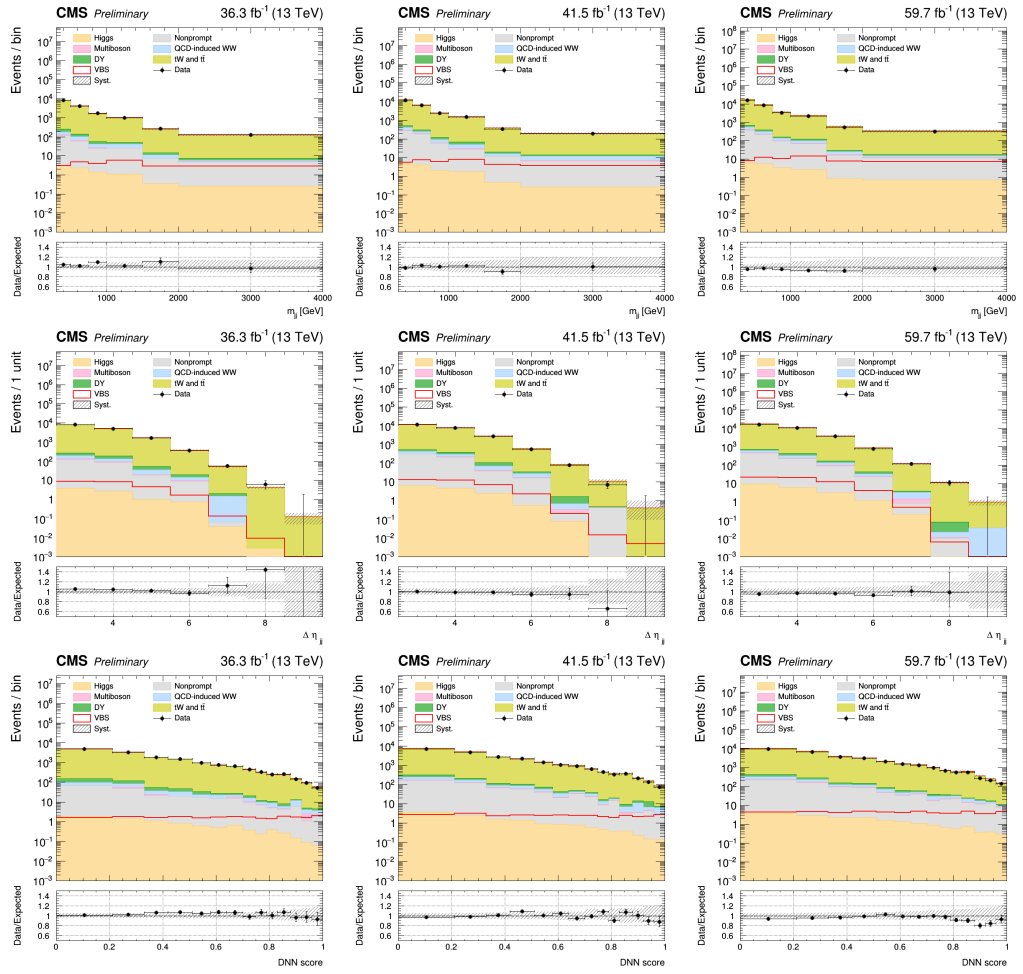
Figure 5.14: Observation and prediction in top eμ CRs of 2016 (left), 2017 (center) and 2018 (right) data sets for m_{jj} (first row), $|\Delta\eta_{\text{jj}}|$ (second row) and DNN output (third row) distributions, respectively.
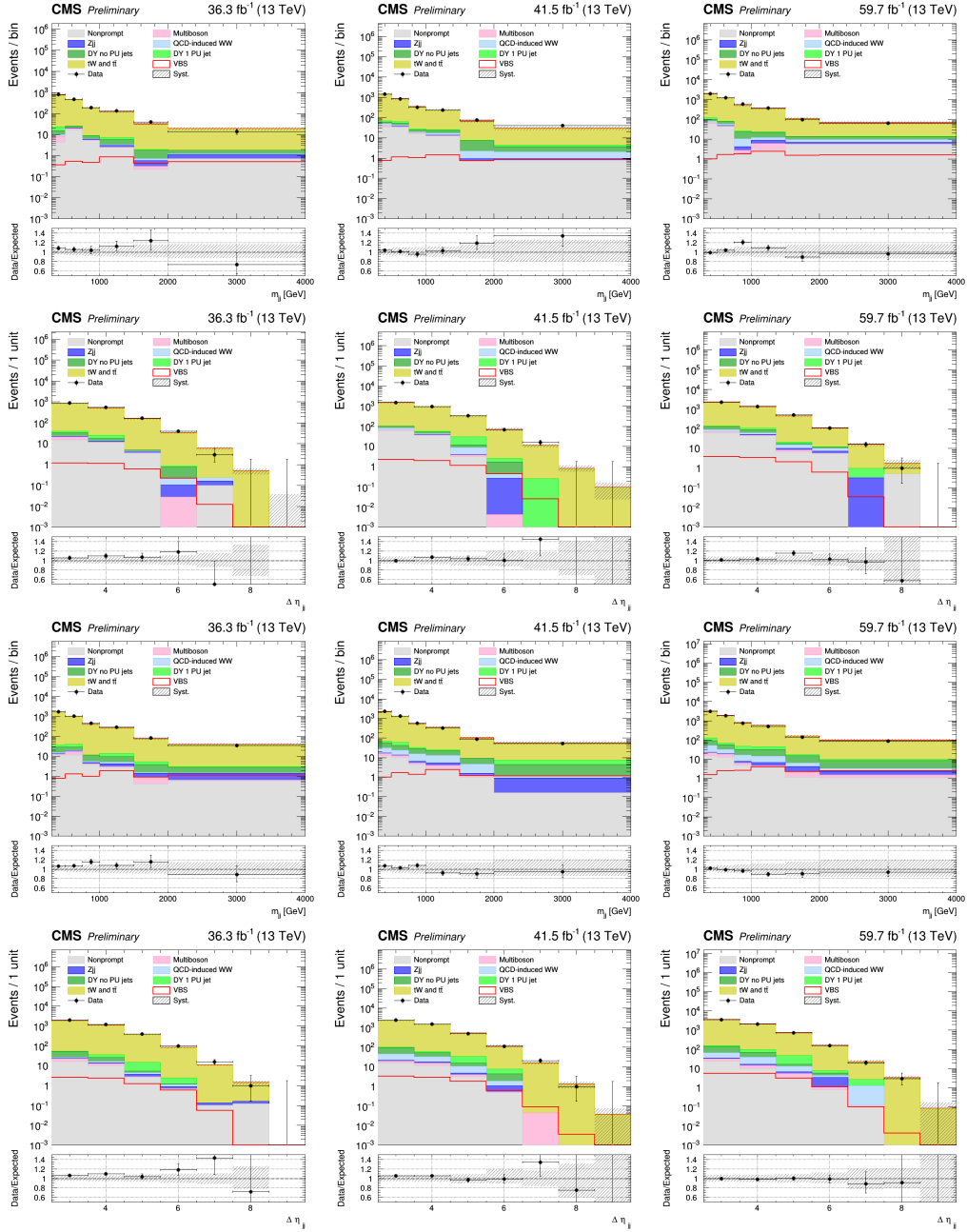
Figure 5.15: Observation and prediction in top ee and $\mu\mu$ CRs of 2016 (left), 2017 (center) and 2018 (right) data sets. The m_{jj} and $|\Delta\eta_{jj}|$ distributions are shown in the first (third) and second (fourth) row for the ee ($\mu\mu$) category, respectively.
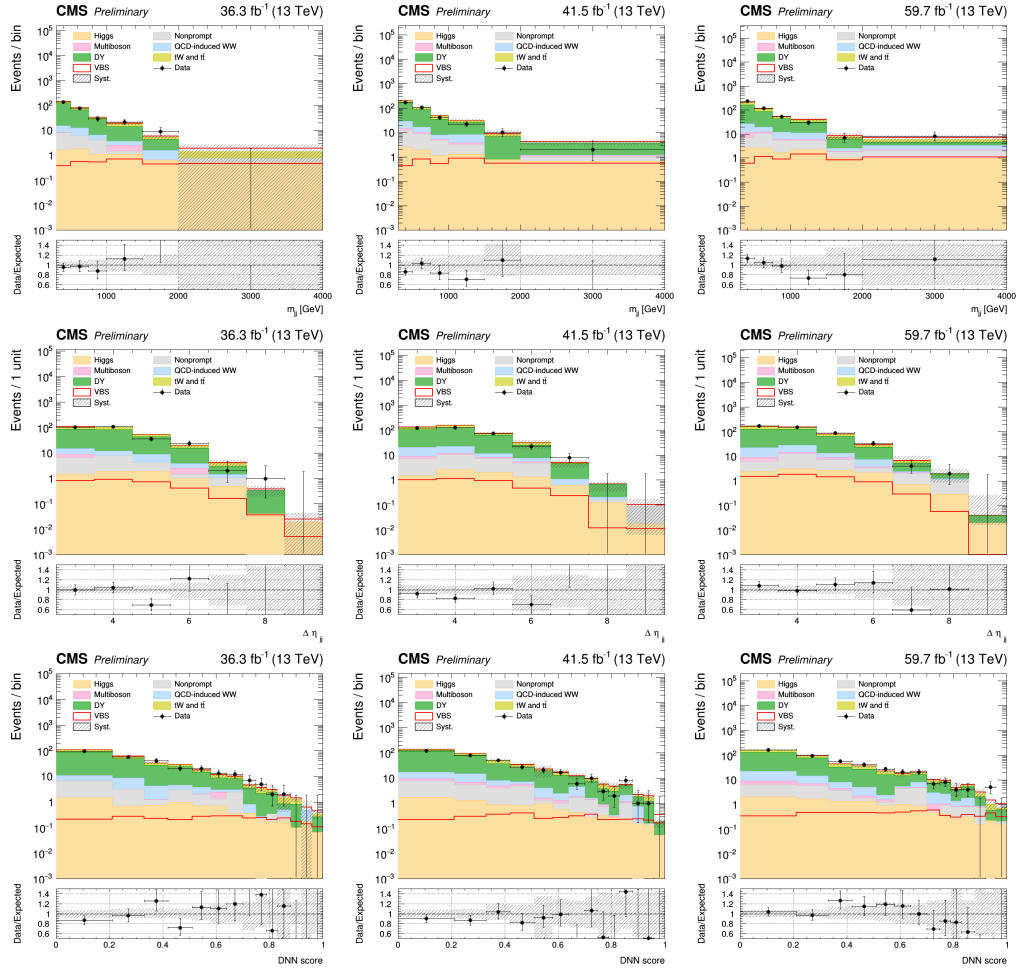
Figure 5.16: Observation and prediction in DY eμ CRs of 2016 (left), 2017 (center) and 2018 (right) data sets for m_{jj} (first row), $|\Delta\eta_{jj}|$ (second row) and DNN output (third row) distributions, respectively.
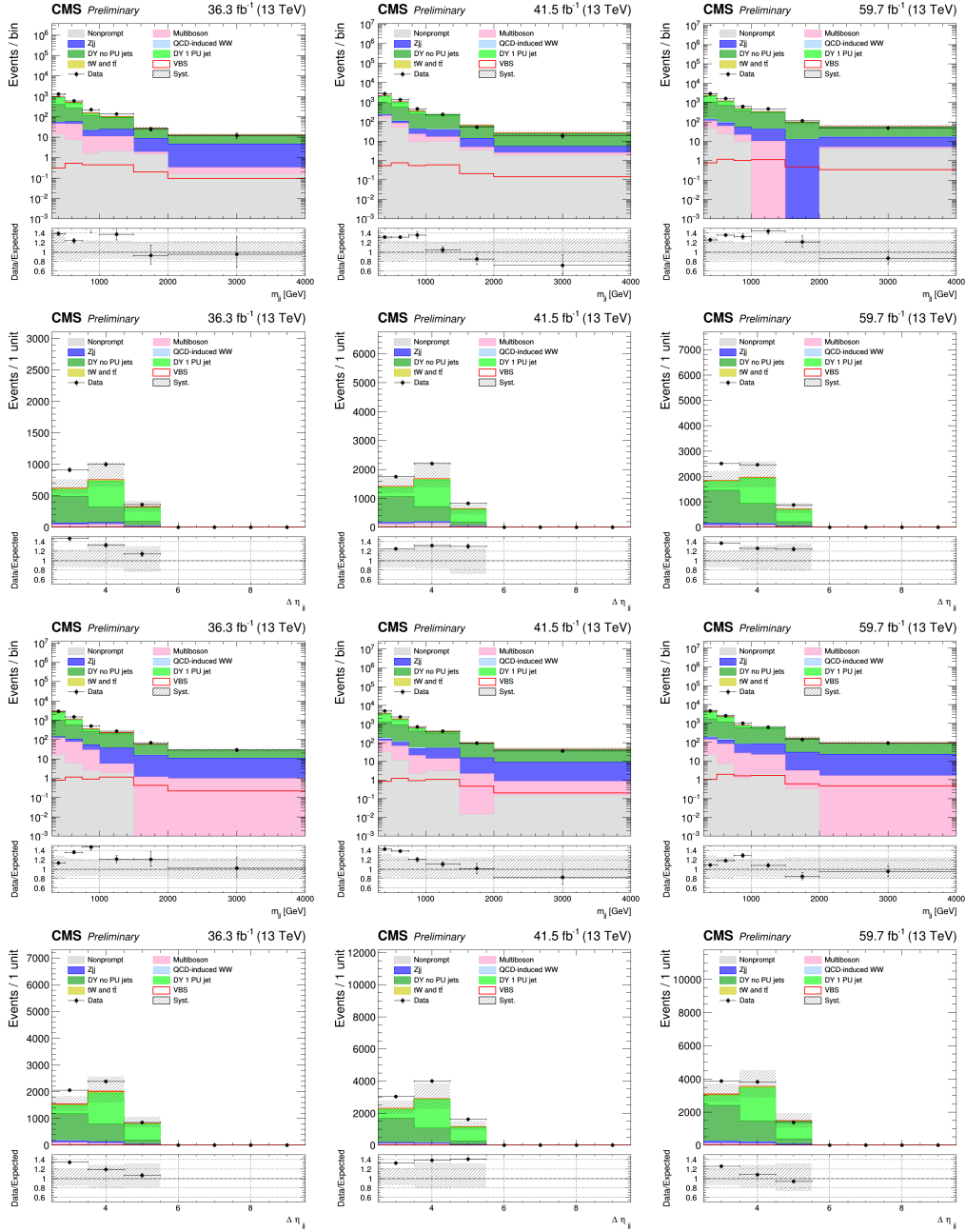
Figure 5.17: Observation and prediction in DY $|\Delta\eta_{jj}| < 5$ ee and $\mu\mu$ CRs of 2016 (left), 2017 (center) and 2018 (right) data sets. The m_{jj} and $|\Delta\eta_{jj}|$ distributions are shown in the first (third) and second (fourth) row for the ee ($\mu\mu$) category, respectively.
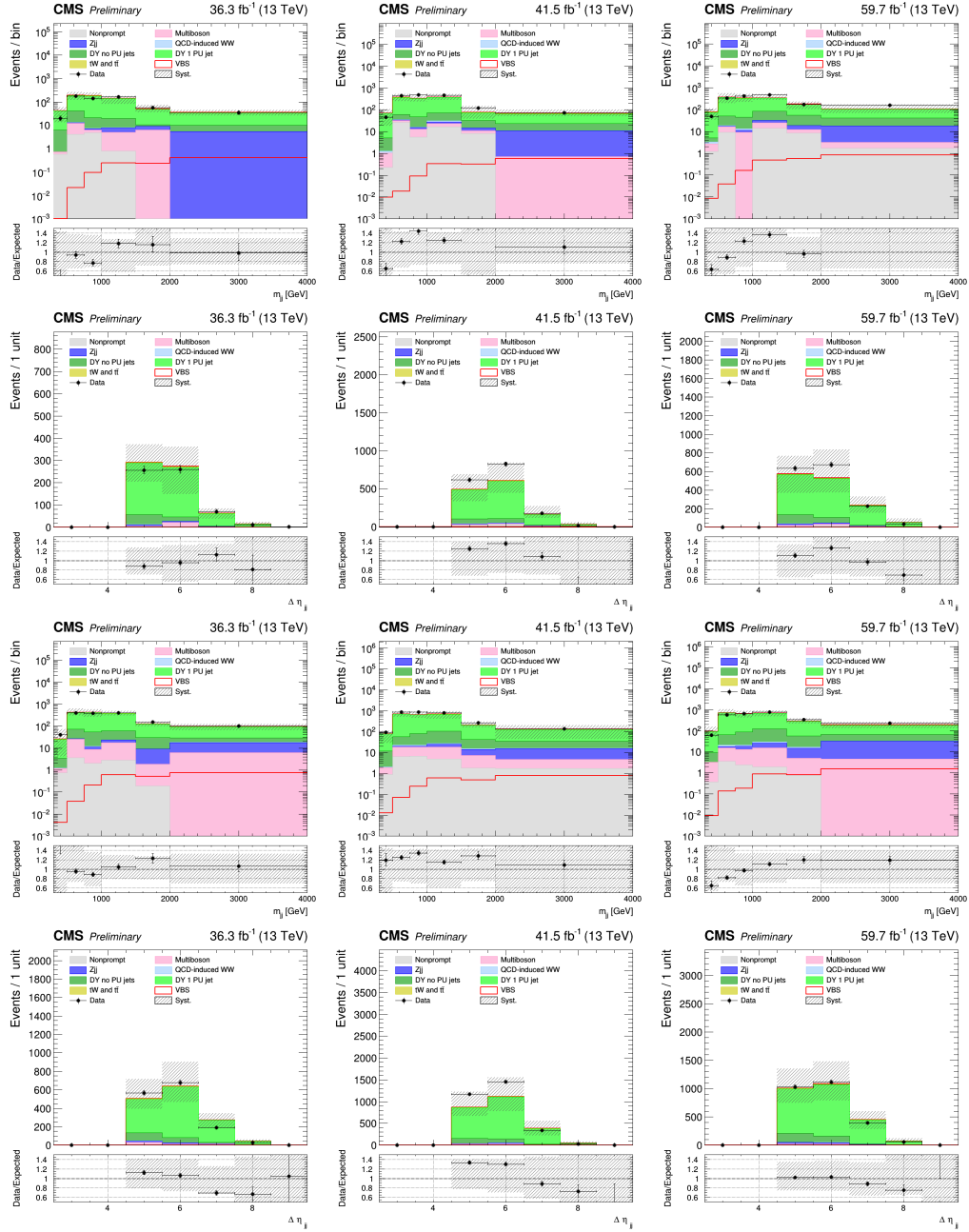
Figure 5.18: Observation and prediction in DY $|\Delta\eta_{jj}| > 5$ ee and $\mu\mu$ CRs of 2016 (left), 2017 (center) and 2018 (right) data sets. The m_{jj} and $|\Delta\eta_{jj}|$ distributions are shown in the first (third) and second (fourth) row for the ee ($\mu\mu$) category, respectively.
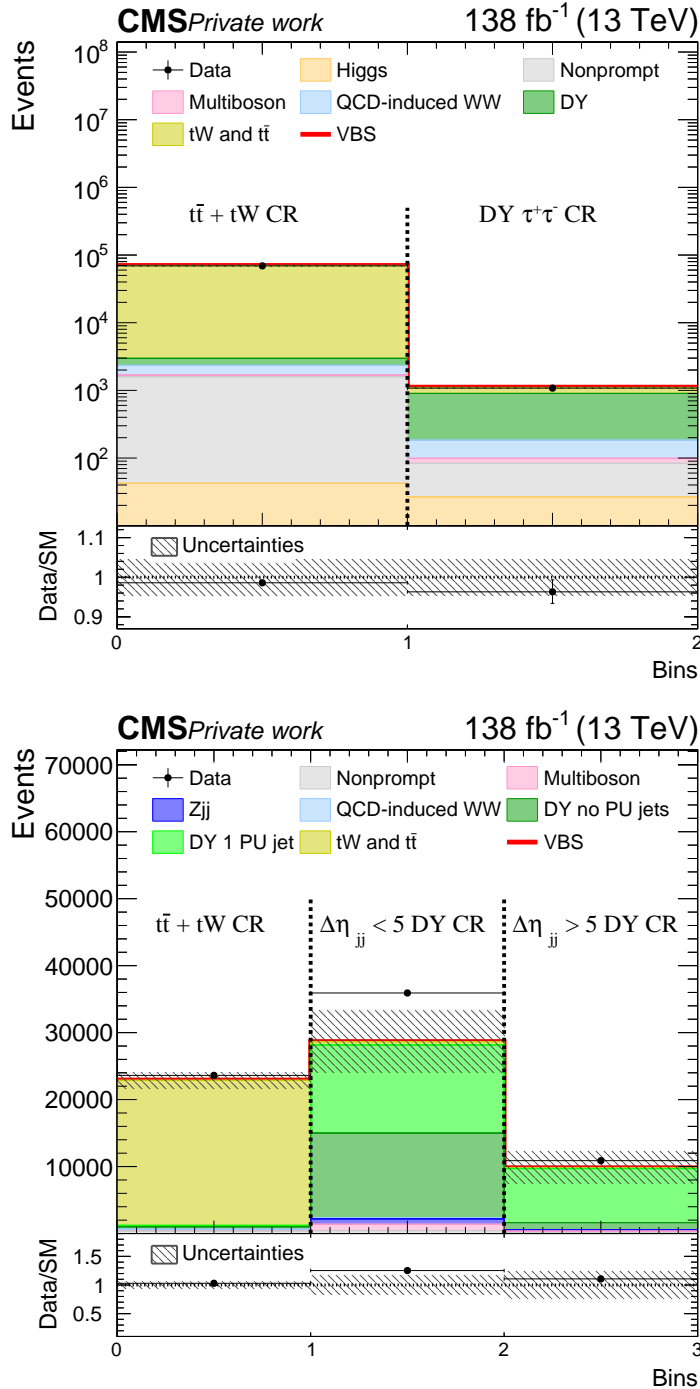
Figure 5.19: Pre-fit number of events in different-flavor (top) and same-flavor (bottom, ee and $\mu\mu$ combined) CRs. In the left plot, the first bin contains the number of events in the $t\bar{t}$ + tW $e\mu$ CR, and the second bin those in the $Z/\gamma^* \to \tau^+\tau^-$ CR. In the bottom plot, the first bin contains the number of events in the $t\bar{t}$ + tW ee and $\mu\mu$ CRs combined, and the second (third) bin those in the $|\Delta\eta_{jj}| < 5$ ($|\Delta\eta_{jj}| > 5$) DY CR. The contributions from background and signal processes (red line) are shown as stacked histograms; systematic uncertainties are plotted as dashed gray bands.

5.5   Systematic uncertainties

Several systematic uncertainties are considered when extracting the VBS cross section, affecting both signal and background predictions. These uncertainties may vary either the normalization or the shape of our distributions of interest, and how they are modeled and included in the fit procedure is described in Sec. 5.6. Systematic uncertainties arise from three different sources: background estimation, experimental measurements and theory prediction. The first one has a considerable impact in the total uncertainty, given the large contribution from $t\bar{t}$ pair production in SRs on the one hand and the difficulty in constraining the QCD-induced W^+W^- background with high precision on the other. Experimental uncertainties affect every reconstructed physics objects such as leptons, jets, b jets and p_T^{miss}. Theoretical uncertainties are included as well and discussed in Sec. 5.5.3. The impact of each uncertainty to the final cross section measurement is reported in Table. 6.6.

5.5.1   Background estimation uncertainties

Uncertainties in the background estimation directly affect the VBS cross section measurement, since signal events are extracted from the fit procedure by subtracting background events from data. Top, QCD-induced W^+W^-, and DY background processes are scaled by normalization factors, which are assigned a flat a-priori distribution and determined in CRs. Most important background uncertainties are listed below:

- **Top background:** The mixture of $t\bar{t}$ and tW samples is treated as one process, therefore the relative contribution of the two is given an uncertainty of about 8%. Indeed, this uncertainty is included to cover variations in the tW-to-$t\bar{t}$ fraction that could modify the shape of variables of interest, such as the DNN output and m_{jj} distribution. The top background normalization is constrained by corresponding CRs and scaled simultaneously in SRs: to avoid any potential tension in the fit between eμ and ee/$\mu\mu$ final states, mainly because of the different kinematic selections applied, the top background is scaled with two independent parameters, one per category (contributions in ee and $\mu\mu$ SRs and CRs are scaled together). Additionally, as already mentioned in Sec. 4.2, different PDF sets and underlying event modeling were used for simulating the 2016 data set with respect to 2017 and 2018 ones. For this reason, the top background is measured with a separate set of scaling parameter in 2016 data set. This strategy is also employed

for estimating all main background normalizations, unless otherwise stated.

- **W$^+$W$^-$ background:** The LO cross section of the gluon-induced W$^+$W$^-$ component is scaled to NLO accuracy by a factor of 1.53, with a corresponding uncertainty of 15% [76]. QCD- and gluon-induced W$^+$W$^-$ normalizations are scaled together with the same correlation scheme as used for the top background estimation.

- **DY background:** The normalization of the DY background in both the eμ and ee/$\mu\mu$ categories is estimated through their respective CRs. In ee and $\mu\mu$ categories, as explained in Sec. 5.2.3, the DY process is divided into two contributions depending on the number of pileup jets in the final state, and they are measured during the fit procedure with independent scaling parameters. For the DY contribution where at least one pileup jet is reconstructed, such parameters are uncorrelated among the three data sets, since the pileup profile is year-dependent, whereas DY contributions from hard scattering are fit with a unique parameter across 2017 and 2018 data set, and a separate one in 2016. In eμ categories, another scaling parameter is used to estimate the normalization of the Z/$\gamma^* \to \tau^+\tau^-$ process as simulated with the τ-embedded technique described in Sec. 5.2.3, with the same correlation scheme as used for measuring top and QCD-induced W$^+$W$^-$ background normalizations. Uncertainties related to the τ-embedding technique are much smaller than those one should include with a standard MC sample, as they only come from measurements of trigger effiency and leptons identification efficiency and energy scale. Residual contamination from diboson and top background processes can enter τ-embedded samples, and these events are removed from MC simulations if the two final state leptons originate from τ leptons, to avoid a potential double-counting: for each vetoed samples, a 10% shape uncertainty is added to take this effect into account.

- **Non-prompt leptons background:** Non-prompt leptons are modeled by applying weights to a superset of signal candidate events identified by leptons passing the loose selection criteria, as described in detail in Sec. 5.2.4. Systematic uncertainties on non-prompt leptons prediction arise from the limited size of the dijet control sample used to estimate this contribution and the difference in the quark-flavor composition of jets faking leptons between control and application regions. The latter effect is estimated by varying the p_T of the jet that recoils

against the lepton in the dijet control sample. The maximum devia-
tion of weights from the nominal value is of order 5% to 10% for both
sources. There is, however, a limitation in capturing the full effect
of jet flavor composition difference with these multiplicative factors.
Therefore, a conservative 30% normalization uncertainty is addition-
ally assigned to this background prediction. Uncertainties in the trans-
fer function are uncorrelated among the three data sets, as far as the
statistical component is considered, and correlated for the jet flavor
composition modeling component.

- **Other minor background processes:** MC samples describing minor
  background processes - multi-boson final states mostly, plus some Higgs
  boson contribution in the eμ SR - receive specific weights (either event-
  by-event or overall) to better match the simulation prediction with
  the observation from the collision data. These weight factors carry
  systematic uncertainties, which are correlated among the three data
  sets.

5.5.2   Experimental uncertainties

Experimental uncertainties can affect both the normalization and the shape
of background and signal processes: the first contribution is only considered
for those samples whose normalization is directly taken from MC simulation,
whereas the latter is always taken into account. The full list of experimental
uncertainties is presented here:

- **Luminosity:** The integrated luminosities for the 2016, 2017 and 2018
  data taking years have individual uncertainties of 1.2, 2.3 and 2.5%,
  respectively [77–79], and the overall uncertainty for the 2016-2018 pe-
  riod is 1.6%. Luminosity measurements are statistically independent
  of each other, but the applied method is the same for all years. To
  account for this, uncertainties related to the finite sample size used to
  calibrate the luminosity are not correlated across the three data sets,
  but systematic effects are.

- **Trigger efficiency:** The trigger efficiency is applied to simulated sam-
  ples as a scale factor computed in bins of lepton p_{T} and η, each carrying
  its own uncertainty. Moreover, in 2016 and 2017 data sets, the trigger
  inefficency due to ECAL L1 trigger inputs is considered as an addi-
  tional source of systematic uncertainty [80]; all these components are
  kept uncorrelated and can modify both the normalization and shape of
  histograms.

- **Lepton identification and isolation efficiency:** As for the trigger efficency, uncertainties due to electron and muon identification and isolation effiency come from scale factors applied to simulated samples and are uncorrelated across the three years.

- **Lepton momentum scale:** Electron and muon momentum scale uncertainties are computed by varying the momenta of leptons within one standard deviation from their nominal value. For each variation, an alternative set of histograms is derived, where each affected physics observable is recomputed to account for possible migrations of simulated events inside or outside the analysis acceptance.

- **Jet energy scale and resolution:** JEC uncertainties are computed by including eleven sources of corrections, which model the knowledge of the absolute and relative jet energy scale, as a function of the jet p_T and η, respectively, and the jet flavor composition. As for the lepton momentum scale, these variations may modify the distributions of several kinematic quantities, which are recomputed to properly account for such effects. Six JEC uncertainties are correlated across the three data sets. Similarly, JER uncertainties are included in all simulated samples, but are kept uncorrelated among each other.

- **b tagging:** The uncertainty in the b tagging efficency is taken into account by five correlated sources, related to the methodology in the b tagging efficency estimation, and four independent uncertainties for the statistical accuracy of the measurement.

- **Unclustered energy scale:** The p_T^{miss} observable is affected by the precision in the measurement of all aforementioned physics objects, plus the contribution from pileup spurious tracks and jets. The effect of the p_T^{miss} resolution is included by applying a Gaussian smearing of 10% in the individual p_T^{miss} components, and each affected observable is recomputed. Since this quantity is solely determined by the reconstruction performances of the detector, an individual uncertainty is applied to each data set.

- **Pileup jet identification efficiency:** This measurement is performed in bins of the jet p_T and η and considering jets with $p_T < 50$ GeV, as plieup identification techniques are only applied to the low-p_T jet spectrum. Given that this is a purely detector effect, corresponsing uncertainties are uncorrelated across the three data takings.

- **MC statistic uncertainties:** The statistical uncertainty due to the limited size of MC simulated events is included in each bin of the signal and background samples.

5.5.3 Theoretical uncertainties

Theoretical uncertainties are assigned to simulated samples to cover the limited knowledge of physics processes: they include uncertainties in the choice of PDF sets, renormalization and factorization scales, in the parton showering, underlying event and pileup modeling.

- **Renormalization and factorization scales:** These uncertainties are taken into account because of missing higher order terms in the perurbative expansions of cross section calculations. They are computed by varying renormalization and factorization scales up and down independently by a factor of two with respect to their nominal values, ignoring the extreme cases where they are shifted in opposite directions [81,82]. The envelopes of the various distributions are taken as one standard-deviation variation. Only shape effects are included when varying such scales for theoretical uncertainties that affect the signal and main backgrounds, since their normalizations are directly measured in data.

- **PDF sets:** PDF uncertainties are computed as recommended by the NNPDF collaboration prescription. As far as the signal process is concerned, their shape effect is negligible. Similar considerations hold for the QCD-induced W^+W^- background. For top and DY backgrounds, shape variations introduced by PDF uncertainties can only change the ratio of the expected yields between the SR and the CR, as an acceptance factor. Such uncertainties are considered in CRs and estimated to be 1% and 2% for $t\bar{t}$ and DY MC samples, respectively. Contributions from other MC samples are small and have been neglected. Overall, the impact of this uncertainty in the signal cross section measurement is less than 1%.

- **Parton shower:** For each simulated sample, parton shower uncertainties are computed by PYTHIA 8: the renormalization scale, which regulates the dynamics of the parton splitting evolution, is shifted by a factor of 2 and 0.5 for both initial and final state radiations. Only shape effects are retained for the signal and the main background processes.

- **Underlying event:** Uncertainties in the underlying event modeling are derived by varying PYTHIA 8 tune parameters as described in Ref. [57].

- **Pileup:** To quantify this uncertainty, the total inelastic pp cross section is varied by 5% with respect to its nominal value of 69.2 mb, as measured from data [83, 84].

A summary of all systematic uncertainties included in this analysis, as well as their correlation scheme in the fit procedure, is showed in Table 5.4.

Uncertainty	Process	Type	Correlation scheme
Background uncertainties			
Single top tt̄ composition	top	shape	correlated
top normalization	top	free floating normalization	correlated for 2017 and 2018 data sets, uncorrelated between eμ and ee/μμ categories
Z/γ* → τ+τ− normalization	Z/γ* → τ+τ−	free floating normalization	correlated for 2017 and 2018 data sets
Z/γ* → ℓ+ℓ− normalization	Z/γ* → ℓ+ℓ−	free floating normalization	correlated for 2017 and 2018 data sets, uncorrelated between eμ and ee/μμ categories
QCD-induced W+W− normalization	QCD-induced W+W−	free floating normalization	correlated for 2017 and 2018 data sets, uncorrelated between eμ and ee/μμ categories
Fake rate (limited size sample)	non-prompt	shape	uncorrelated
Fake rate (jet flavor composition)	non-prompt	global normalization	correlated
Experimental uncertainties			
Integrated luminosity	all MC but top, W+W− and DY	global normalization	partially uncorrelated
b-tagging scale factors	all MC	shape	partially uncorrelated
Trigger efficiency	all MC	shape	uncorrelated
Prefiring scale factor	all MC	shape	uncorrelated, only for 2016 and 2017 data sets
Lepton efficiency	all MC	shape	uncorrelated
Lepton p_T scale	all MC	normalization per category	uncorrelated
Jet energy scale	all MC	normalization per category	partially uncorrelated
Jet energy resolution	all MC	normalization per category	uncorrelated, only for 2017 and 2018 data sets
Jet pile up ID scale factor	all MC	shape	DY without pileup jets: uncorrelated for 2017 and 2018 data sets, DY with pileup jets: uncorrelated
Unclustered p_T^{miss}	all MC	normalization per category	uncorrelated
Theoretical uncertainties			
Renormalization and factorization scales	all MC	shape for VBS, top, W+W− and DY, global normalization for the rest	correlated
PDF set	top and DY	shape	correlated
Parton shower	all MC	shape	correlated
Underlying event	all MC	global normalization	correlated for 2016 and 2017 data sets
Pileup	all MC	global normalization	uncorrelated

Table 5.4: Systematic uncertainties and correlation scheme. Free floating normalization uncertainties are unconstrained parameters that scale background processes in SRs and CRs. Global normalization parameters are assigned to uncertainties that affect the overall yield of a given process in both SRs and CRs, whereas normalization parameters per category have different effects in SRs and CRs, but are correlated among each other. Conversely, shape uncertainties modify process yields bin-by-bin.

5.6   Signal extraction

The signal extraction is performed through a maximum-likelihood template
fit of the discriminating variable discussed in Sec. 5.3. This method [3,85] is
a technique for estimating the values of a set of parameters $\boldsymbol{\theta} = (\theta_1, ..., \theta_m)$
from a finite sample of data. Given n measurements of a random variable x
distributed according to a probability density function (p.d.f.) $f(x; \boldsymbol{\theta})$, the
likelihood function is defined as:

$$L(\boldsymbol{\theta}) = \prod_{i=1}^{n} f(x_i; \boldsymbol{\theta}) \tag{5.1}$$

where x_i is the outcome of the random variable x for the i-th measurement
and L is treated as a function of the parameters $\boldsymbol{\theta}$. The maximum-likelihood
(ML) estimators $\hat{\boldsymbol{\theta}}$ of the true parameters $\boldsymbol{\theta}$ are those which maximize the
likelihood function; if $L(\boldsymbol{\theta})$ is a differentiable function of $(\theta_1, ..., \theta_m)$ and the
maximum is not at the boundary of the parameters range, ML estimators
are solutions to the following equations:

$$\frac{\partial L}{\partial \hat{\theta}_i} = 0 \quad i = 1, ..., m \tag{5.2}$$

where $\hat{\theta}_i$ is evaluated at the global maximum. Since the functional form of
the p.d.f for this measurement is not analytically known, a binned ML fit
is performed. This procedure consists in replacing the unknown p.d.f. with
histograms of the random variable x, called templates, representing each
signal and background contribution obtained from MC simulations.

In fact, the likelihood function definition may be extended to the case
of a histogram containing N bins, each filled with $N_{obs}^{(i)}$ number of observed
events, where $i = \{1, ..., N\}$. In order to check whether the measured number
of signal events is compatible with the SM hypothesis, it is convenient to
introduce the signal strenght "modifier" parameter μ, defined as the ratio
between the measured signal cross section and the SM expectation. Thus,
$N_{obs}^{(i)}$ is expected to be Poisson-like distributed around $\mu s_i + b_i$, where s_i and
b_i are the expected yields of signal and background events for the i-th bin,
respectively, and μ is referred to as the parameter of interest (POI):

$$L(\mu) = \prod_{i=1}^{N} \frac{(\mu s_i + b_i)^{N_{obs}^{(i)}}}{N_{obs}^{(i)}!} e^{-(\mu s_i + b_i)} \equiv \prod_{i=1}^{N} \mathcal{P}(N_{obs}^{(i)}; \mu s_i + b_i) \tag{5.3}$$

Maximizing $L(\mu)$ with respect to μ gives the ML estimator $\hat{\mu}$ for the true value
μ. This estimation is called a template fit. After one or more discriminating

variables are selected, all templates in each category are embedded within the binned likelihood function, determining how the signal strength is adjusted during the fit procedure. However, the likelihood function defined in Eq. (5.3) does not take into account any systematic uncertainty that modifies the templates. The effects caused by these uncertainties may either vary the normalization or the shape of the histograms. Systematic uncertainties are included in the likelihood as additional parameters: even though they are determined through the same fit procedure, they are not of interest to the analysis, hence they are called nuisance parameters $\boldsymbol{\nu}$, or simply nuisances. The likelihood function can be rewritten as follows:

$$L(\mu, \boldsymbol{\nu}) = \prod_{i=1}^{N} \mathcal{P}(N_{obs}^{(i)}; \mu s_i + b_i) \mathcal{N}(\boldsymbol{\nu}) \tag{5.4}$$

where $\mathcal{N}(\boldsymbol{\nu})$ is a constraint on the likelihood function determined by the set of nuisances $\boldsymbol{\nu}$. The value of a normalization uncertainty is estimated a-priori and modeled by a parameter z that is assumed to be distributed as a log-normal p.d.f., representing the degree of belief in the knowledge of this source.

$$f(z; \nu, \sigma_z) = \frac{1}{z \sigma_z \sqrt{2\pi}} \exp\left(-\frac{(\ln z - \nu)^2}{2\sigma_z^2}\right) \tag{5.5}$$

The log-normal distribution is suitable for this purpose since we are dealing with the estimation of non-negative parameters. The hypothesis $\nu = 0$ corresponds to the nominal yield, and the value of σ_z determines the size of the constraint in the associated nuisance parameter z.

Nuisances that modify the template's shape are called shape uncertainties and need to be treated differently, as they cannot be parametrized by a single a-priori distribution. For each systematic source, two additional input templates must be provided to account for shape uncertainties, corresponding to up and down variations of one standard deviation. Such nuisance parameters are estimated by bin-wise interpolation of the histograms: a spline function is used between the one standard deviation interval, and it becomes a straight line outside of this range. Implementation details can be found at this documentation [86].

Finally, statistical fluctuations due to the limited size of MC samples are assigned to bin-by-bin nuisance parameters, which scale the total bin yield within its uncertainty. This is estimated as the Guassian uncertainty of un-weighted events in each bin, and a single parameter is given to all processes entering that bin - if at least a total of ten un-weighted events are found, which is always the case. This approximation is known as the

Barlow-Beeston-lite approach [87], and it is particularly useful to reduce the number of nuisances in the likelihood function.

Chapter 6

Results

All SRs and CRs are simultaneously fit to data through the maximum-likelihood template fit described in Sec. 5.6. Results are presented and discussed in this Chapter.

6.1 Expected results

Before moving to the results obtained from real data, it is important to estimate the expected sensitivity of this analysis to the VBS signal. This can be quantitavely done by means of the so called "Asimov" toy data set, a pseudo experiment in which data are replaced with the amount of signal-plus-background events predicted by SM simulations in each bin of the histograms. Additionally, all nuisances are fixed to their nominal a-priori value in this particular data set. The maximization of the likelihood function with respect to the model parameters will return $\hat{\mu} = 1$ and $\hat{z} = 0 \pm \sigma_z$ by construction, for signal strenght and nuisance parameters, respectively. However, this procedure allows to preliminary assess the total expected uncertainty in the POI, assuming that real data will exactly be distributed as the SM prediction in the signal-plus-background hypothesis H_{s+b}.

A similar estimation can be performed in terms of the statistical significance of the VBS signal. This quantity gives a measure of how consistent data are with the background-only hypothesis H_b. In the fit to the Asimov data set, this is the significance that one would obtain if exactly the SM signal is observed. In order to formulate a statement about the compatibility between data and the H_b hypothesis, it is convenient to construct a test statistic: requiring a threshold on this variable is equivalent to defining a critical region that is used to decide whether the H_b hypothesis may be rejected or not. By the Neyman-Pearson lemma [88], the profile-likelihood

(PL) ratio $\lambda(\mu)$ is the test statistic with the highest discriminating power between any two hypotheses. The PL ratio is defined as:

$$\lambda(\mu) = \frac{L(\mu, \hat{\hat{\boldsymbol{\nu}}})}{L(\hat{\mu}, \hat{\boldsymbol{\nu}})} \tag{6.1}$$

where $\hat{\mu}$ and $\hat{\boldsymbol{\nu}}$ are ML estimators of the POI and nuisances, respectively, while $\hat{\hat{\boldsymbol{\nu}}}$ is the set of nuisances that maximizes the likelihood function for a given signal strength μ. The assumption of the H_b hypothesis corresponds to computing the PL ratio with $\mu = 0$. To extract the significance of a $\hat{\mu} > 0$ result obtained by fitting our chosen discriminating variables to either the Asimov data set or real data, the following test statistic is used:

$$q_0 = \left\{ \begin{array}{ll} -2 \ln \lambda_0 & \hat{\mu} \geq 0 \\ 0 & \hat{\mu} < 0 \end{array} \right. \tag{6.2}$$

where $\lambda_0 \equiv \lambda(\mu = 0)$ is the PL ratio in the H_b hypothesis. The definition of q_0 provided by Eq. (6.2) reflects the fact that only upward fluctuations of data are regarded as signal evidence ($\hat{\mu} \geq 0$). Thus, this scenario must be protected from the case in which a negative signal strength parameter is estimated, that might happen when observed data are less than the amount of expected background events.

This test has both the desirable properties to satisfy the Neyman-Pearson lemma by construction and, according to the Wilks' theorem [89], can be asymptotically approximated as a χ^2 distribution with 1 degree of freedom. In the large sample limit, the statistical significance is computed as $Z = \sqrt{q_0}$, where $\sqrt{q_0}$ will follow a gaussian distribution with null mean and standard deviation $\sigma = 1$. In other words, Z may be regarded as the "number of sigmas" by which the test statistic, assuming $\mu = 0$, deviate from the H_b hypothesis.

To estimate the a-priori uncertainty in the POI, the test statistic $q(\mu) = -2 \ln \lambda(\mu)$ is employed again: by definition, $q(\mu)$ has a minimum in 0 for $\mu = \hat{\mu}$ and the $\gamma = 68\%$ confidence level (CL) - to be interpreted as the range that includes the true parameter with a probability of 68% - is taken as the interval in which the test statistic increases by one. In the asymptotic limit, this procedure correspond to extract from a gaussian distribution the quantiles associated to a probability 1-γ/2, i.e. boundaries at ± 1 standard deviation. Even though the likelihood will be not perfectly distributed as a gaussian function, it can be shown that this prescription still ensure the 68% coverage; in general, such an interval is asymmetric with respect to $\hat{\mu}$.

Expected results for the eμ category are shown in Table 6.1, where performances of the m_{jj} variable and DNN output are compared. The expected

significance obtained when the DNN score is fit to the Asimov data set is a $\sim 10\%$ better than the result from using the m_{jj} distribution as discriminating variable, and also the expected total uncertainty is slightly smaller in the first case. Therefore, the former observable is chosen for extracting the VBS signal out of real data.

Fit variable	Expected significance (number of σ)	Expected signal strenght
m_{jj}	4.0	$1.00^{+0.26}_{-0.25}$
DNN output	4.3	$1.00^{+0.25}_{-0.24}$

Table 6.1: Expected significance and signal strength errors in eμ categories. Results obtained from fitting the m_{jj} and DNN output distributions are compared.

When adding ee and $\mu\mu$ categories to the likelihood function, the expected significance overcomes the 5σ threshold, i.e., the minimum distance from the H_b hypothesis to be discarded, and above which we can claim for the signal observation - if confirmed in data. Expected results for each channel and their combination, with the full Run 2 data set, are summarized in Table 6.2.

Channel	Expected significance (number of σ)	Expected signal strenght
ee	1.7	$1.00^{+0.61}_{-0.58}$
$\mu\mu$	2.6	$1.00^{+0.43}_{-0.40}$
eμ	4.3	$1.00^{+0.25}_{-0.24}$
eμ + ee + $\mu\mu$	5.2	$1.00^{+0.21}_{-0.20}$

Table 6.2: Expected significance and signal strength errors in eμ, ee, $\mu\mu$ categories and their combination with the full Run 2 data set.

6.2 Post-fit distributions

The full Run 2 CMS data set is analyzed to extract the VBS cross section. To do so, the histograms of discriminating variables discussed in Sec. 5.3 are fed into the binned likelihood function, together with the number of events in CRs. Figs. 6.1 and 6.2 show the observed post-fit distributions in bins of the DNN output for the eμ category, and in bins of m_{jj} and $|\Delta\eta_{\mathrm{jj}}|$ for the ee and $\mu\mu$ categories combined, respectively. For displaying purposes, distributions in Figs. 6.1 and 6.2 are derived with a common binning, to include the whole data set in a single histogram; all systematic uncertainties are propagated and properly taken into account. The difference between data and MC in the last bin of the DNN output for $Z_{\ell\ell} < 1$ in Fig. 6.1 was investigated

by verifying that input variables reasonably agreed with data at DNN >
0.88. The discrepancy is not localized in any bins of such distributions and,
because of the good modeling of the top background, is therefore considered
to be compatible with a statistical under-fluctuation of data. Fig. 6.3 shows
the number of post-fit events in the CRs. Post-fit event yields are shown
in Table 6.4. Observed results for each channel and their combination are
summarized in Table 6.3.

Channel	Observed significance (number of σ)	Observed signal strenght
ee	1.5	$1.45^{+0.75}_{-0.70}$
$\mu\mu$	3.4	$1.42^{+0.48}_{-0.44}$
eμ	3.5	$0.85^{+0.26}_{-0.25}$
eμ + ee + $\mu\mu$	5.6	$1.12^{+0.22}_{-0.22}$

Table 6.3: Observed significance and signal strength errors in eμ, ee, $\mu\mu$
categories and their combination with the full Run 2 data set.
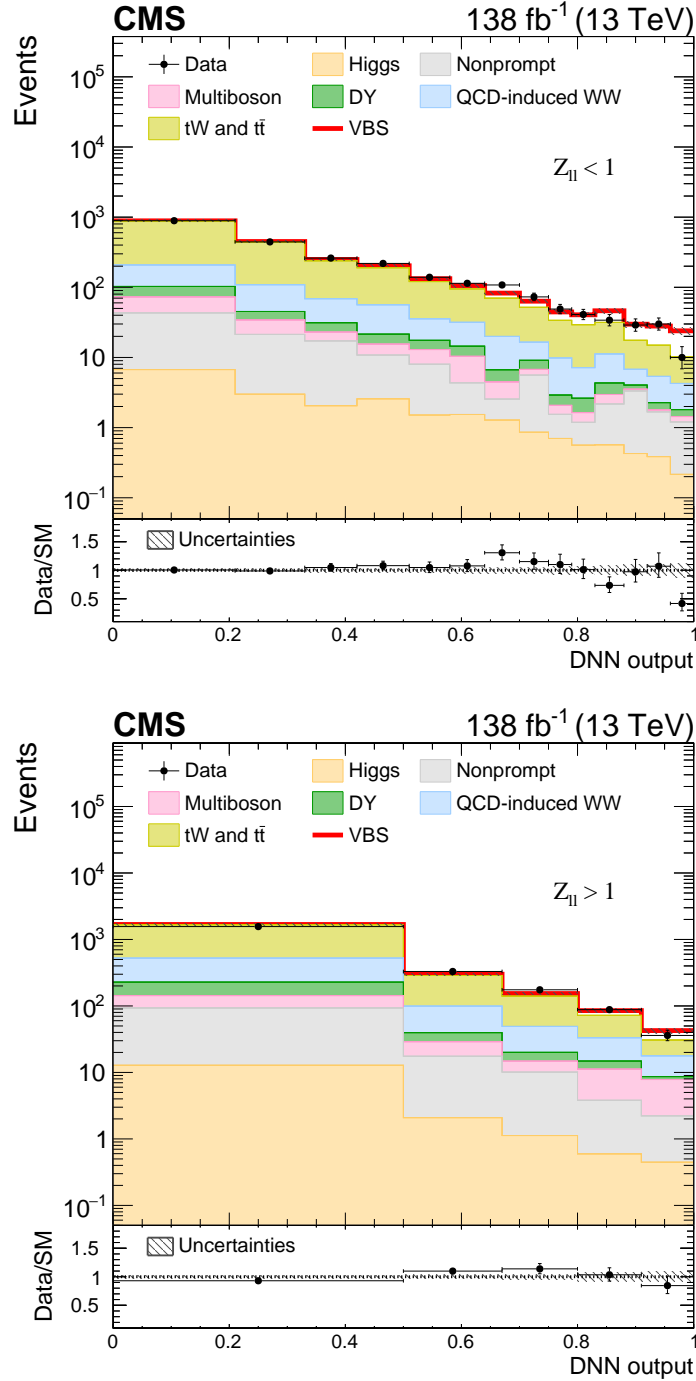
Figure 6.1: Post-fit DNN output distribution in different-flavor SRs for $Z_{\ell\ell} < 1$ (top) and $Z_{\ell\ell} > 1$ (bottom) categories. This variable quantifies how likely each event is signal. The contributions from background and signal (red line) processes are shown as stacked histograms; systematic uncertainties are plotted as dashed gray bands.
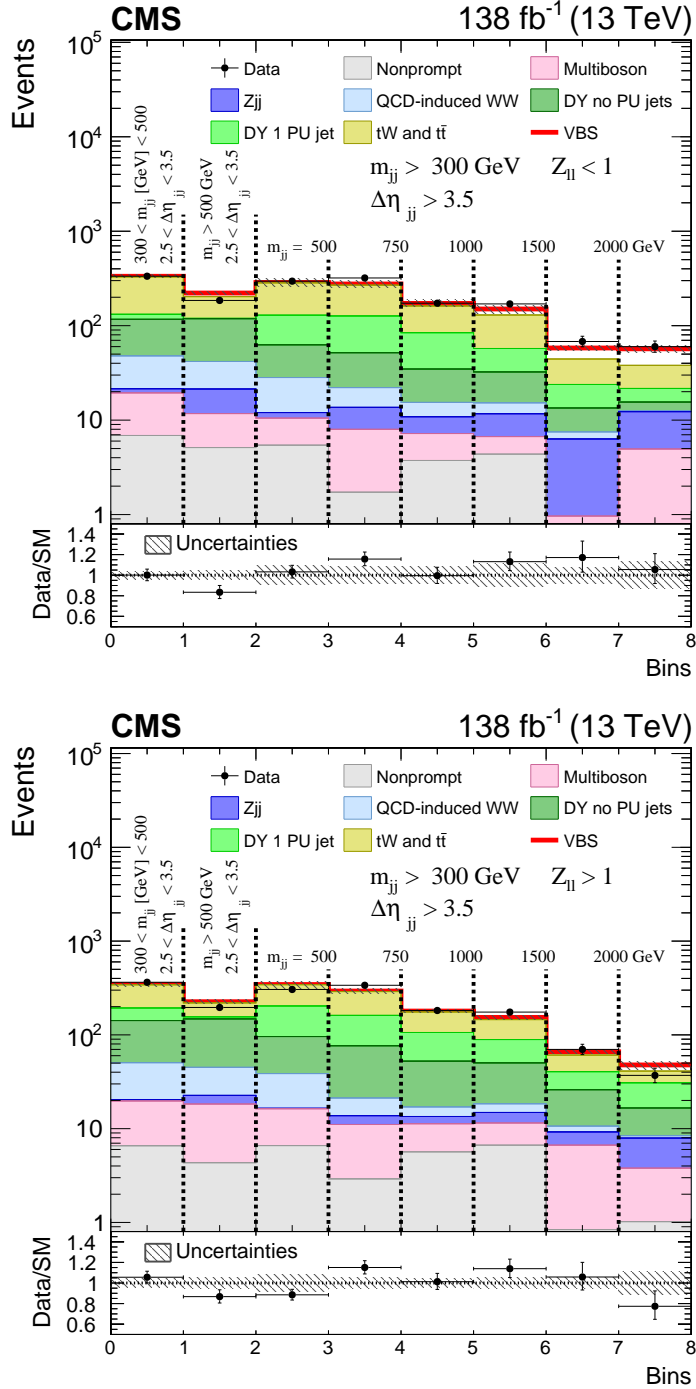
Figure 6.2: Post-fit m_{jj} distribution and number of events in ee and $\mu\mu$ combined SRs for $Z_{\ell\ell} < 1$ (top) and $Z_{\ell\ell} > 1$ (bottom) categories. The first two bins contain the number of events in the selected region (as reported in the plots themselves). The third bin contains the number of events in the $300 < m_{jj}$ [GeV] < 500 and $|\Delta\eta_{jj}| > 3.5$ regions and, for display purposes, is included in the m_{jj} distribution, shown in the last five bins. The contributions from background and signal (red line) processes are shown as stacked histograms; systematic uncertainties are plotted as dashed gray bands.

Figure 6.3: Post-fit number of events in different-flavor (top) and same-flavor (bottom, ee and $\mu\mu$ combined) CRs. In the left plot, the first bin contains the number of events in the $t\bar{t}$ + tW eμ CR, and the second bin those in the $Z/\gamma^* \to \tau^+\tau^-$ CR. In the bottom plot, the first bin contains the number of events in the $t\bar{t}$ + tW ee and $\mu\mu$ CRs combined, and the second (third) bin those in the $|\Delta\eta_{jj}| < 5$ ($|\Delta\eta_{jj}| > 5$) DY CR. The contributions from background and signal processes (red line) are shown as stacked histograms; systematic uncertainties are plotted as dashed gray bands.
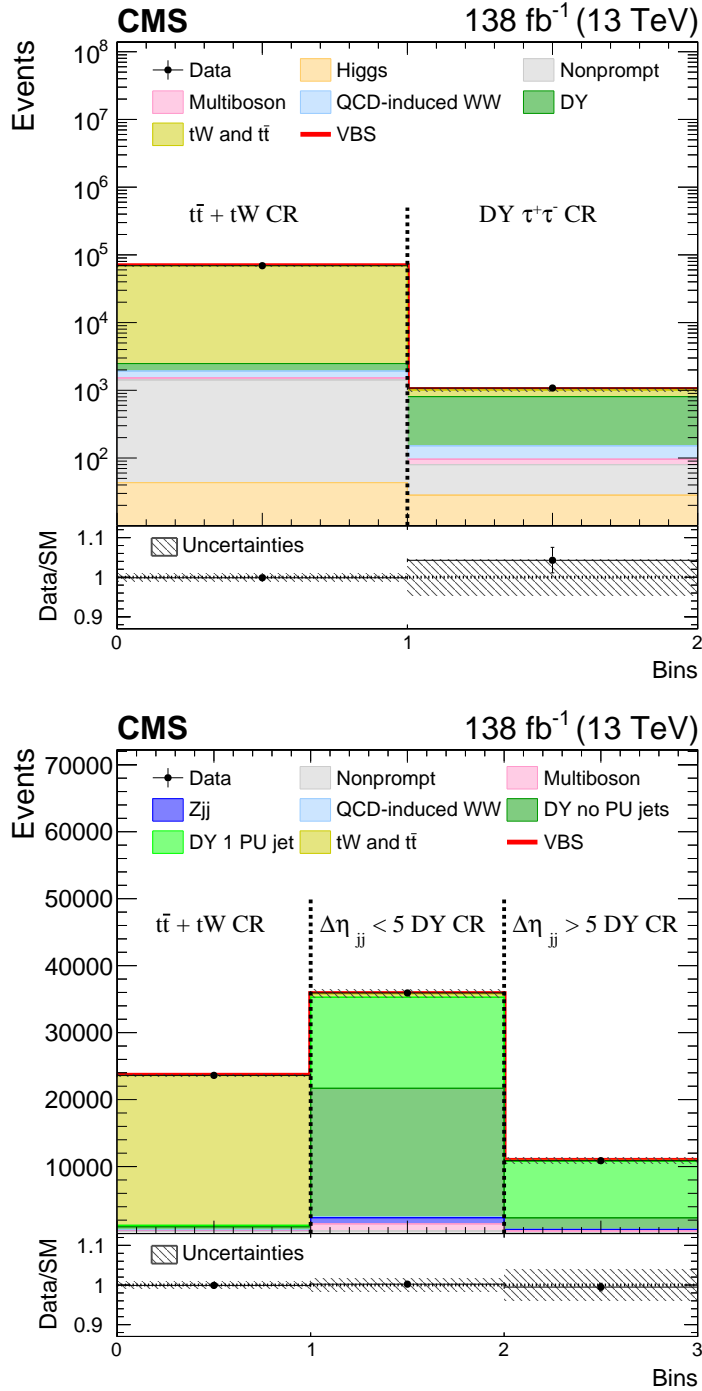
Process	SR eμ $Z_{\ell\ell} < 1$	SR eμ $Z_{\ell\ell} > 1$	SR ee/$\mu\mu$ $Z_{\ell\ell} < 1$	SR ee/$\mu\mu$ $Z_{\ell\ell} > 1$
DATA	2441	2192	1606	1667
Signal + background	2396.8 ± 98.5	2239.6 ± 106.0	1590.4 ± 49.4	1660.5 ± 43.6
Signal	169.1 ± 20.2	69.9 ± 8.4	98.0 ± 6.5	38.3 ± 2.5
Background	2227.7 ± 96.4	2169.7 ± 105.6	1492.4 ± 48.9	1622.1 ± 43.5
$t\bar{t}$ + tW	1629.4 ± 71.4	1452.5 ± 69.5	767.8 ± 14.5	642.5 ± 13.2
QCD-induced W^+W^-	327.0 ± 61.6	409.3 ± 77.3	111.1 ± 16.6	121.5 ± 17.3
Nonprompt	107.0 ± 18.4	109.9 ± 16.4	30.0 ± 4.9	32.0 ± 4.2
DY no PU jets	–	–	259.5 ± 27.3	408.3 ± 17.1
DY + 1 PU jets	–	–	222.7 ± 33.3	337.4 ± 32.9
$Z/\gamma^* \to \tau^+\tau^-$	69.2 ± 4.6	102.0 ± 5.8	–	–
Multiboson	67.7 ± 6.6	75.6 ± 7.3	60.9 ± 3.8	60.1 ± 4.8
EWK Z + 2j	1.0 ± 0.2	0.4 ± 0.0	40.5 ± 4.2	20.3 ± 1.3
Higgs	26.6 ± 1.5	20.1 ± 1.0	–	–

Table 6.4: Post-fit process yields and uncertainties in each SR (ee and $\mu\mu$ final states combined).

To validate our approach for the DY estimation in same-flavor categories, in Fig. 6.4 we show the m_{jj} and $|\Delta\eta_{\mathrm{jj}}|$ post-fit distributions in the inclusive CRs shows both. If compared to Fig. 5.3, data are much more well described, although none of these observables have been included in the likelihood function. This provide proof for the goodness of our method, which means that separating the pileup jets DY contribution from hard scattering events greatly helps in restoring the agreement between data and MC simulation in a VBS-like phase space, where the DY background is difficult to model.
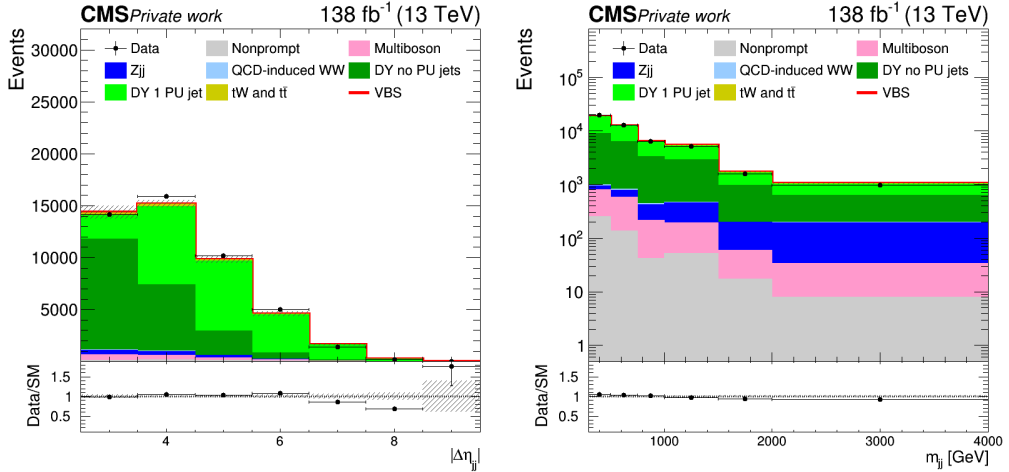
Figure 6.4: Observation and prediction in the inclusive DY CR from the full Run 2 data set of post-fit $|\Delta\eta_{\mathrm{jj}}|$ (left) and m_{jj} (right) distributions.

Moreover, we also verified post-fit distributions for the most relevant input variables that are fed to the DNN algorithm. In particular, in Fig. 6.5, the m_{jj} and $|\Delta\eta_{jj}|$ distributions are shown in the two $Z_{\ell\ell}$ categories, and predictions agree with data within post-fit uncertainties.
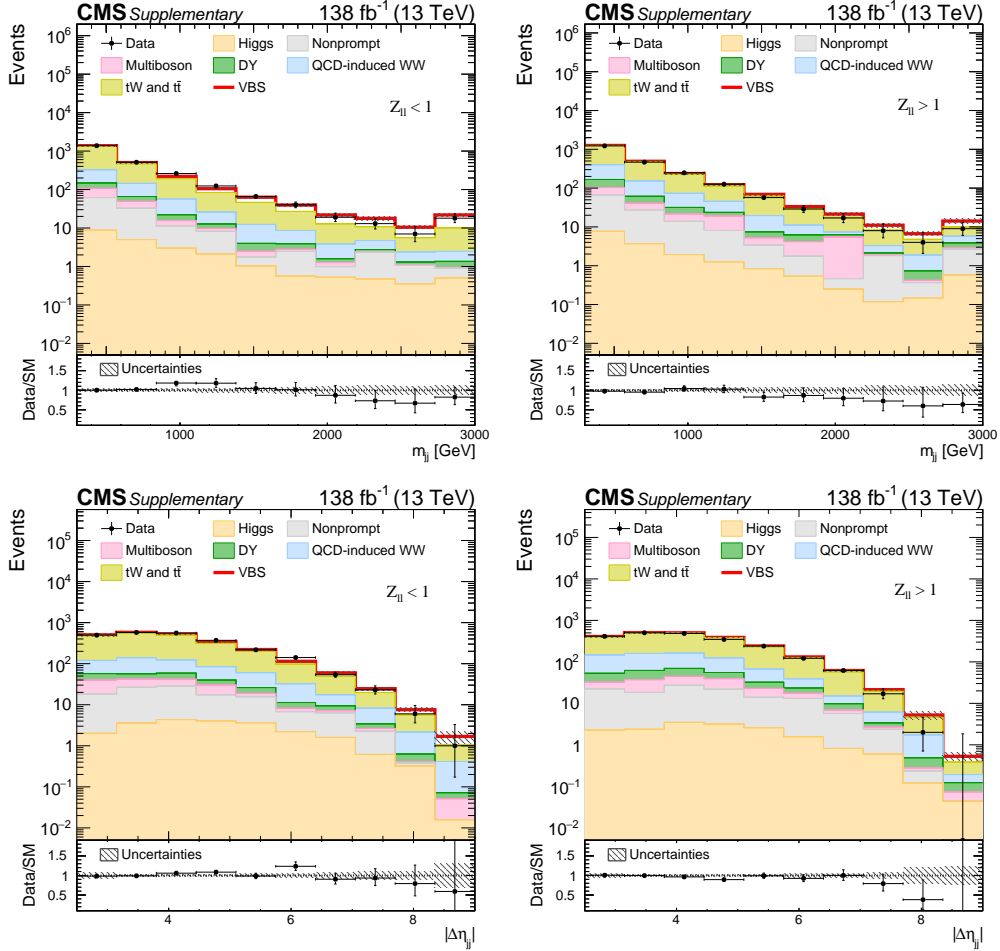
Figure 6.5: Post-fit distributions of m_{jj} (upper row) and $|\Delta\eta_{jj}|$ (lower row) variables in different-flavor SRs for $Z_{\ell\ell} < 1$ (left column) and $Z_{\ell\ell} > 1$ (right column) categories. These variables are among the nine observables used as inputs for the DNN, as listed in Table 5.2. The contributions from background and signal (red line) processes are shown as stacked histograms; systematic uncertainties are plotted as dashed gray bands.

6.3 Cross section measurements

The EW W^+W^- production cross section is measured in two different fiducial volumes, i.e., restricted portions of the generator-level phase space: one is defined to closely match the acceptance of detector-level selections, thus limiting extrapolation uncertainties, whereas the other one represents the region where the VBS signal sample is generated. The former volume is defined with the same set of selections as that outlined in Table 5.1 for SRs, but kinematic requirements are transposed to generator-level. To maximize the overlap between the fiducial and the experimental volumes, generator-level selections replicate physics-objects definitions as much as possible: if a photon is found within a distance $\Delta R < 0.1$ from a lepton, its four-momentum is added to that of the lepton, making a "dressed" lepton. Additionally, if such a lepton is found within a distance $\Delta R = 0.4$ from a jet axis, the jet is discarded from the corresponding collection. Electrons and muons coming from a τ decay are vetoed. The missing transverse momentum is computed as the modulus of the vector sum of transverse momenta associated with all invisible particles generated in the event, and is required to be greater than 20 GeV. A summary of the requirements of the experimental-like fiducial volume is presented in Table 6.5. The measured fiducial cross section is 10.2 ± 2.0 fb, to be compared with the LO theoretical prediction of 9.1 ± 0.6 (scale) fb, where the uncertainty is computed by varying the factorization scale of the signal. The observed (expected) significance for the signal with respect to the H_b hypothesis is 5.6 (5.2) standard deviations, therefore this measurement represents the first observation of the EW W^+W^- production and is compatible with the SM prediction.

In the more inclusive fiducial volume, parton-level requirements define the phase space of interest, in particular the two outgoing partons $(qq^{'})$ are required to have $p_T > 10$ GeV and an invariant mass $m_{qq'} > 100$ GeV; τ leptons are included in the simulated signal sample, and their subsequent decay to leptons is included as part of the signal. The measured fiducial inclusive cross section is 99 ± 20 fb, and falls within the LO prediction of 89 ± 5 (scale) fb.

The complete list of systematic uncertainties included in the signal extraction procedure was presented in Table 5.4. In Table 6.6, the effect each source has in the cross section measurement is reported. The same set of theoretical uncertainties is considered for the signal sample across the two fiducial volumes, from the choice of the factorization scale, to the parton shower and underlying event modeling. PDF variations have not been included, since they do not introduce any shape effect in the m_{jj} and DNN output distributions - a normalization rescaling of the signal does not affect

Objects	Requirements
Leptons	eμ, ee, $\mu\mu$ (not from τ decay), opposite charge $p_\mathrm{T}^{\mathrm{dressed}\,\ell} = p_\mathrm{T}^\ell + \sum_i p_\mathrm{T}^{\gamma_i}$ if $\Delta\mathrm{R}(\ell, \gamma_i) < 0.1$ $p_\mathrm{T}^{\ell_1} > 25$ GeV, $p_\mathrm{T}^{\ell_2} > 13$ GeV, $p_\mathrm{T}^{\ell_3} < 10$ GeV $\lvert\eta\rvert < 2.5$ $p_\mathrm{T}^{\ell\ell} > 30$ GeV, $m_{\ell\ell} > 50$ GeV
Jets	$p_\mathrm{T}^{j} > 30$ GeV $\Delta\mathrm{R}(j, \ell) > 0.4$ At least 2 jets, no b jets $\lvert\eta\rvert < 4.7$ $m_\mathrm{jj} > 300$ GeV, $\lvert\Delta\eta_\mathrm{jj}\rvert > 2.5$
$p_\mathrm{T}^{\mathrm{miss}}$	$p_\mathrm{T}^{\mathrm{miss}} > 20$ GeV

Table 6.5: Definition of the fiducial volume similar to the reconstructed SR.

the measured cross section. The different effect theoretical uncertainties have in the two volumes is taken into account. The POI is the signal strength parameter, so to quote cross sections we perform a dedicated fit with theoretical uncertainties normalized such that the cross section in the relevant fiducial volume is left unaltered. The signal strength parameter from this fit is then simply multiplied by the expected cross section in its respective phase space to get the measured cross section. The normalization factor turns out to be very close for the two volumes, therefore the total relative uncertainty is basically the same in the two cases. The systematic component of the overall relative uncertainty is 13.1%, and the combined relative uncertainty is 19.8%. The statistical contribution is evaluated by freezing all systematic uncertainties to their best-fit result, and its value is 14.9%.

Despite the large amount of data collected by the CMS experiment from 2016 to 2018, the analysis sensitivity is still limited by statistical uncertainties, which, however, are becoming comparable in size with the systematic component. Future LHC runs of data taking, such as the Run 3 - officially started in July 2022, expected to end in 2025 and collect 250 fb^{-1} of data - will further increase the experimental precision in VBS measurements, and possibly open a window for differential cross section measurements, which can provide additional information to either confirm or disprove SM predictions.

Uncertainty source	Value
QCD-induced W^+W^- normalization	5.3%
$t\bar{t}$ scale variation	5.1%
VBS signal scale variation	5.0%
$t\bar{t}$ normalization	4.9%
b tagging	3.5%
Trigger corrections	3.3%
DY normalization	2.9%
Jet energy scale + resolution	2.6%
Unclustered p_T^{miss}	2.4%
QCD-induced W^+W^- scale variation	2.1%
Integrated luminosity	2.0%
Muon efficiency	2.0%
Pileup	1.8%
Electron efficiency	1.5%
Underlying event	1.3%
Parton shower	1.0%
Other	<1%
Total systematic uncertainty	13.1%
Total statistical uncertainty	14.9%
Total uncertainty	19.8%

Table 6.6: Sources of systematic uncertainty affecting the cross section measurement by more than 1%. The total uncertainty is also reported, as well as the total systematic and statistical contributions.

Conclusions

In this work, the first observation of the EW production of a W^+W^- bosons pair is reported. The analysis is based on the full Run 2 data set collected by the CMS experiment, and corresponding to an integrated luminosity of $138\,\text{fb}^{-1}$. Signal candidates must pass either single or double lepton triggers, as both W bosons are required to decay into a light lepton, along with its corresponding neutrino. Moreover, two VBS-like jets are selected, i.e. tight m_{jj} and $|\Delta\eta_{jj}|$ kinematic cuts are applied to the two jets with the highest p_T in the event. To achieve a better sensitivity to the VBS signal process, both different- and same-flavor final states are considered for this analysis, which, combined together, have enough statistical power to make the observation possible.

Indeed, the main challenges of this analysis are the background estimation and reduction techniques, which are fundamental ingredients for measuring such a rare process. Unlike other VBS modes, the W^+W^- channel is populated by the $t\bar{t}$ pair production background, which represents the main background source for its huge cross section: a DNN algorithm is used to disentangle this background and the QCD-induced W^+W^- production from the VBS signal in eμ categories. On the other hand, ee and $\mu\mu$ final states are also dominated by DY events in which pileup jets fake the real source of p_T^{miss} that one would expect from the emission of neutrinos. A dedicated strategy is developed to measure this background process, and the m_{jj} variable has enough discriminating power to suppress it in ee and $\mu\mu$ categories.

The statistical significance of the EW W^+W^- production is 5.6 standard deviations with respect to the background-only hypothesis (5.2 expected). Two fiducial cross section measurements are quoted for this process, one being more inclusive, as it represents the cross section measured in the phase space where the signal sample has been generated, and the other one being closer to the experimental selection outlined at reconstruction-level. The measured (expected) value is 99 ± 20 fb for the former and 10.2 ± 2.0 fb for the latter, and they are both in agreement with LO predictions - 89 ± 5 (scale) fb and 9.1 ± 0.6 (scale) fb, respectively.

Future data taking periods of the LHC will enable further precision studies in the context of VBS measurement, from the Run 3 - which has just started - to the upcoming high luminosity phase, which will allow to collect more than 3000 fb^{-1} of new data. In this landscape, differential cross section measurements and combinations of multiple diboson VBS channels will play a key role in understanding the physics of these rare EW processes, possibly pointing to new physics phenomena that governate laws of nature in the realm of high energy interactions.

Bibliography

[1] The CMS Collaboration. First observation of the electroweak production of a leptonically decaying W^+W^- pair in association with two jets in $\sqrt{s} = 13$ TeV pp collisions. Technical report, CERN, Geneva, 2021. URL: `https://cds.cern.ch/record/2791336`.

[2] Michael E. Peskin and Daniel V. Schroeder. *An Introduction to quantum field theory.* Addison-Wesley, Reading, USA, 1995. URL: `http://www.slac.stanford.edu/~mpeskin/QFT.html`.

[3] Particle Data Group et al. Review of Particle Physics. *Progress of Theoretical and Experimental Physics*, 2022(8), 08 2022. 083C01. `arXiv:https://academic.oup.com/ptep/article-pdf/2022/8/083C01/45434166/ptac097.pdf`, `doi:10.1093/ptep/ptac097`.

[4] Sheldon L. Glashow. Partial-symmetries of weak interactions. *Nuclear Physics*, 22(4):579 – 588, 1961. URL: `http://www.sciencedirect.com/science/article/pii/0029558261904692`, `doi:https://doi.org/10.1016/0029-5582(61)90469-2`.

[5] Abdus Salam. Weak and Electromagnetic Interactions. *Conf. Proc.*, C680519:367–377, 1968.

[6] Steven Weinberg. A model of leptons. *Phys. Rev. Lett.*, 19:1264–1266, Nov 1967. URL: `https://link.aps.org/doi/10.1103/PhysRevLett.19.1264`, `doi:10.1103/PhysRevLett.19.1264`.

[7] Peter W. Higgs. Broken symmetries and the masses of gauge bosons. *Phys. Rev. Lett.*, 13:508–509, Oct 1964. URL: `https://link.aps.org/doi/10.1103/PhysRevLett.13.508`, `doi:10.1103/PhysRevLett.13.508`.

[8] The ATLAS Collaboration. Observation of a new particle in the search for the Standard Model Higgs boson with the ATLAS detector at the

LHC. *Phys. Lett. B*, 716:1, 2012. `arXiv:1207.7214, doi:10.1016/j.physletb.2012.08.020`.

[9] The CMS Collaboration. Observation of a new boson at a mass of 125 GeV with the CMS experiment at the LHC. *Phys. Lett. B*, 716:30, 2012. `arXiv:1207.7235, doi:10.1016/j.physletb.2012.08.021`.

[10] The CMS Collaboration. Observation of a new boson with mass near 125 GeV in pp collisions at $\sqrt{s} = 7$ and 8 TeV. *JHEP*, 06:081, 2013. `arXiv:1303.4571, doi:10.1007/JHEP06(2013)081`.

[11] Steven Weinberg. *The Quantum Theory of Fields: 15. Non-Abelian gauge theories*, volume 2, page 1–62. Cambridge University Press, 1996. `doi:10.1017/CBO9781139644174.003`.

[12] David J. Gross and Frank Wilczek. Ultraviolet behavior of non-abelian gauge theories. *Phys. Rev. Lett.*, 30:1343–1346, Jun 1973. URL: `https://link.aps.org/doi/10.1103/PhysRevLett.30.1343, doi:10.1103/PhysRevLett.30.1343`.

[13] Guido Altarelli and G. Parisi. Asymptotic Freedom in Parton Language. *Nucl. Phys.*, B126:298–318, 1977. `doi:10.1016/0550-3213(77)90384-4`.

[14] Matteo Cacciari, Gavin P. Salam, and Gregory Soyez. The anti-k_t jet clustering algorithm. *JHEP*, 04:063, 2008. `arXiv:0802.1189, doi:10.1088/1126-6708/2008/04/063`.

[15] Benjamin W. Lee, C. Quigg, and H. B. Thacker. Weak interactions at very high energies: The role of the Higgs-boson mass. *Phys. Rev. D*, 16:1519, 1977. `doi:10.1103/PhysRevD.16.1519`.

[16] Michał Szleper. The higgs boson and the physics of *ww* scattering before and after higgs discovery, 2014. URL: `https://arxiv.org/abs/1412.8367, doi:10.48550/ARXIV.1412.8367`.

[17] The CMS Collaboration. Observation of electroweak production of same-sign W boson pairs in the two jet and two same-sign lepton final state in proton-proton collisions at $\sqrt{s} = 13$ TeV. *Phys. Rev. Lett.*, 120:081801, 2018. `arXiv:1709.05822, doi:10.1103/PhysRevLett.120.081801`.

[18] The ATLAS Collaboration. Observation of electroweak production of a same-sign W boson pair in association with two jets in pp collisions at $\sqrt{s} = 13$ TeV with the ATLAS detector. *Phys. Rev. Lett.*, 123:161801, 2019. `arXiv:1906.03203, doi:10.1103/PhysRevLett.123.161801`.

[19] Albert M Sirunyan et al. Measurements of production cross sections of WZ and same-sign WW boson pairs in association with two jets in proton-proton collisions at $\sqrt{s} = 13$ TeV. *Phys. Lett. B*, 809:135710, 2020. `arXiv:2005.01173`, `doi:10.1016/j.physletb.2020.135710`.

[20] The ATLAS Collaboration. Observation of electroweak w±z boson pair production in association with two jets in pp collisions at s=13 tev with the atlas detector. *Physics Letters B*, 793:469–492, 2019. URL: `https://www.sciencedirect.com/science/article/pii/S0370269319303211`, `doi:https://doi.org/10.1016/j.physletb.2019.05.012`.

[21] The CMS Collaboration. Measurements of production cross sections of polarized same-sign W boson pairs in association with two jets in proton-proton collisions at $\sqrt{s} = 13$ TeV. *Phys. Lett. B*, 812:136018, 2021. `arXiv:2009.09429`, `doi:10.1016/j.physletb.2020.136018`.

[22] H. Georgi and M. Machacek. Doubly charged Higgs bosons. *Nucl. Phys. B*, 262:463, 1985. `doi:10.1016/0550-3213(85)90325-6`.

[23] The CMS Collaboration. Evidence for electroweak production of four charged leptons and two jets in proton-proton collisions at s=13tev. *Physics Letters B*, 812:135992, 2021. URL: `https://www.sciencedirect.com/science/article/pii/S0370269320307954`, `doi:https://doi.org/10.1016/j.physletb.2020.135992`.

[24] The ATLAS Collaboration. Observation of electroweak production of two jets and a *z*-boson pair, 2020. URL: `https://arxiv.org/abs/2004.10612`, `doi:10.48550/ARXIV.2004.10612`.

[25] The CMS Collaboration. Observation of electroweak production of $w\gamma$ with two jets in proton-proton collisions at s=13 tev. *Physics Letters B*, 811:135988, 2020. URL: `https://www.sciencedirect.com/science/article/pii/S0370269320307917`, `doi:https://doi.org/10.1016/j.physletb.2020.135988`.

[26] The CMS Collaboration. Measurement of the $w\gamma$ production cross section in proton-proton collisions at $\sqrt{s} = 13$ TeV and constraints on effective field theory coefficients. *Phys. Rev. Lett.*, 126:252002, Jun 2021. URL: `https://link.aps.org/doi/10.1103/PhysRevLett.126.252002`, `doi:10.1103/PhysRevLett.126.252002`.

[27] The ATLAS Collaboration. Measurement of electroweak $z(\nu\bar{\nu})\gamma jj$ production and limits on anomalous quartic gauge couplings in pp collisions at $\sqrt{s} = 13$ tev with the atlas detector, 2022. URL: `https://arxiv.org/abs/2208.12741`, `doi:10.48550/ARXIV.2208.12741`.

[28] The CMS Collaboration. Measurement of the cross-section of the electroweak production of a $Z\gamma$ pair in association with two jets in pp collisions at $\sqrt{s} = 13$ TeV with the ATLAS detector. Technical report, CERN, Geneva, 2021. URL: `https://cds.cern.ch/record/2779171`.

[29] The CMS Collaboration. Evidence for ww/wz vector boson scattering in the decay channel lnqq produced in association with two jets in proton-proton collisions at s=13 tev. *Physics Letters B*, 834:137438, 2022. URL: `https://www.sciencedirect.com/science/article/pii/S037026932200572X`, `doi:https://doi.org/10.1016/j.physletb.2022.137438`.

[30] The CMS Collaboration. Search for electroweak diboson production in association with a high-mass dijet system in semileptonic final states in pp collisions at $\sqrt{s} = 13$ TeV with the atlas detector. *Phys. Rev. D*, 100:032007, Aug 2019. URL: `https://link.aps.org/doi/10.1103/PhysRevD.100.032007`, `doi:10.1103/PhysRevD.100.032007`.

[31] Lyndon Evans and Philip Bryant. LHC Machine. *JINST*, 3:S08001, 2008. `doi:10.1088/1748-0221/3/08/S08001`.

[32] The ATLAS Collaboration. The ATLAS Experiment at the CERN Large Hadron Collider. *JINST*, 3:S08003, 2008. `doi:10.1088/1748-0221/3/08/S08003`.

[33] The CMS Collaboration. The CMS experiment at the CERN LHC. *Journal of Instrumentation*, 3(08):S08004–S08004, aug 2008. URL: `https://doi.org/10.1088%2F1748-0221%2F3%2F08%2Fs08004`, `doi:10.1088/1748-0221/3/08/s08004`.

[34] The LHCb Collaboration. The LHCb Detector at the LHC. *JINST*, 3:S08005, 2008. `doi:10.1088/1748-0221/3/08/S08005`.

[35] The ALICE Collaboration. The ALICE experiment at the CERN LHC. *JINST*, 3:S08002, 2008. `doi:10.1088/1748-0221/3/08/S08002`.

[36] The CMS Collaboration. Particle-flow reconstruction and global event description with the CMS detector. *JINST*, 12:P10003, 2017. `arXiv:1706.04965`, `doi:10.1088/1748-0221/12/10/P10003`.

[37] The CMS Collaboration. Performance of the CMS muon detector and muon reconstruction with proton-proton collisions at $\sqrt{s} = 13$ TeV. *JINST*, 13:P06015. 53 p, Apr 2018. URL: `http://cds.cern.ch/record/2313130`, `arXiv:1804.04528`, `doi:10.1088/1748-0221/13/06/P06015`.

[38] The CMS Collaboration. Description and performance of track and primary-vertex reconstruction with the CMS tracker. *Journal of Instrumentation*, 9(10):P10009–P10009, oct 2014. `doi:10.1088/1748-0221/9/10/p10009`.

[39] The CMS Collaboration. Higgs boson production in association with top quarks in final states with electrons, muons, and hadronically decaying tau leptons at $\sqrt{s} = 13$ TeV. Technical report, CERN, Geneva, 2020. URL: `https://cds.cern.ch/record/2725523`.

[40] The CMS Collaboration. Measuring Electron Efficiencies at CMS with Early Data. Technical report, CERN, Geneva, Dec 2008. URL: `https://cds.cern.ch/record/1194482`.

[41] A. Bodek, A. van Dyne, J. Y. Han, W. Sakumoto, and A. Strelnikov. Extracting muon momentum scale corrections for hadron collider experiments. *The European Physical Journal C*, 72(10), oct 2012. URL: `https://doi.org/10.1140%2Fepjc%2Fs10052-012-2194-8`, `doi:10.1140/epjc/s10052-012-2194-8`.

[42] The CMS Collaboration. Electron and photon reconstruction and identification with the CMS experiment at the CERN LHC. *Journal of Instrumentation*, 16(05):P05014, may 2021. URL: `https://doi.org/10.1088%2F1748-0221%2F16%2F05%2Fp05014`, `doi:10.1088/1748-0221/16/05/p05014`.

[43] Matteo Cacciari and Gavin P. Salam. Pileup subtraction using jet areas. *Physics Letters B*, 659(1):119 – 126, 2008. URL: `http://www.sciencedirect.com/science/article/pii/S0370269307011094`, `doi:https://doi.org/10.1016/j.physletb.2007.09.077`.

[44] The CMS Collaboration. Pileup Removal Algorithms. Technical report, CERN, Geneva, 2014. URL: `http://cds.cern.ch/record/1751454`.

[45] The CMS Collaboration. Jet algorithms performance in 13 TeV data. Technical report, CERN, Geneva, 2017. URL: `http://cds.cern.ch/record/2256875`.

[46] The CMS Collaboration. Determination of jet energy calibration and transverse momentum resolution in CMS. *Journal of Instrumentation*, 6(11):P11002–P11002, nov 2011. URL: `https://doi.org/10.1088%2F1748-0221%2F6%2F11%2Fp11002`, `doi:10.1088/1748-0221/6/11/p11002`.

[47] The CMS Collaboration. Identification of heavy-flavour jets with the CMS detector in pp collisions at 13 TeV. *JINST*, 13(05):P05011, 2018. `arXiv:1712.07158`, `doi:10.1088/1748-0221/13/05/P05011`.

[48] E. Bols, J. Kieseler, M. Verzetti, M. Stoye, and A. Stakia. Jet flavour classification using DeepJet. *JINST*, 15:P12012, 2020. `arXiv:2008.10519`, `doi:10.1088/1748-0221/15/12/p12012`.

[49] Daniele Bertolini, Philip Harris, Matthew Low, and Nhan Tran. Pileup per particle identification. *Journal of High Energy Physics*, 2014(10), oct 2014. URL: `https://doi.org/10.1007%2Fjhep10%282014%29059`, `doi:10.1007/jhep10(2014)059`.

[50] The CMS Collaboration. Performance of missing transverse momentum reconstruction in proton-proton collisions at $\sqrt{s} = 13\,\mathrm{TeV}$ using the CMS detector. *JINST*, 14:P07004, 2019. `arXiv:1903.06078`, `doi:10.1088/1748-0221/14/07/P07004`.

[51] Torbjörn Sjöstrand, Stefan Ask, Jesper R. Christiansen, Richard Corke, Nishita Desai, Philip Ilten, Stephen Mrenna, Stefan Prestel, Christine O. Rasmussen, and Peter Z. Skands. An introduction to PYTHIA 8.2. *Comput. Phys. Commun.*, 191:159, 2015. `arXiv:1410.3012`, `doi:10.1016/j.cpc.2015.01.024`.

[52] S. Agostinelli et al. Geant4—a simulation toolkit. *Nuclear Instruments and Methods in Physics Research Section A: Accelerators, Spectrometers, Detectors and Associated Equipment*, 506(3):250 – 303, 2003. URL: `http://www.sciencedirect.com/science/article/pii/S0168900203013688`, `doi:https://doi.org/10.1016/S0168-9002(03)01368-8`.

[53] Richard D. Ball, Valerio Bertone, Stefano Carrazza, Luigi Del Debbio, Stefano Forte, Alberto Guffanti, Nathan P. Hartland, and Juan Rojo. Parton distributions with QED corrections. *Nucl. Phys. B*, 877:290, 2013. `arXiv:1308.0598`, `doi:10.1016/j.nuclphysb.2013.10.010`.

[54] Richard D. Ball, Valerio Bertone, Francesco Cerutti, Luigi Del Debbio, Stefano Forte, Alberto Guffanti, Jose I. Latorre, Juan Rojo, and Maria

Ubiali. Unbiased global determination of parton distributions and their uncertainties at NNLO and at LO. *Nucl. Phys. B*, 855:153, 2012. `arXiv:1107.2652, doi:10.1016/j.nuclphysb.2011.09.024`.

[55] Richard D. Ball et al. Parton distributions from high-precision collider data. *Eur. Phys. J. C*, 77:663, 2017. `arXiv:1706.00428, doi:10.1140/epjc/s10052-017-5199-5`.

[56] Vardan Khachatryan et al. Event generator tunes obtained from underlying event and multiparton scattering measurements. *Eur. Phys. J. C*, 76:155, 2016. `arXiv:1512.00815, doi:10.1140/epjc/s10052-016-3988-x`.

[57] The CMS Collaboration. Extraction and validation of a new set of CMS PYTHIA8 tunes from underlying-event measurements. *Eur. Phys. J. C*, 80:4, 2020. `arXiv:1903.12179, doi:10.1140/epjc/s10052-019-7499-4`.

[58] J. Alwall, R. Frederix, S. Frixione, V. Hirschi, F. Maltoni, O. Mattelaer, H. S. Shao, T. Stelzer, P. Torrielli, and M. Zaro. The automated computation of tree-level and next-to-leading order differential cross sections, and their matching to parton shower simulations. *JHEP*, 07:079, 2014. `arXiv:1405.0301, doi:10.1007/JHEP07(2014)079`.

[59] Barbara Jager, Alexander Karlberg, Simon Platzer, Johannes Scheller, and Marco Zaro. Parton-shower effects in Higgs production via Vector-Boson Fusion. *Eur. Phys. J. C*, 80(8):756, 2020. `arXiv:2003.12435, doi:10.1140/epjc/s10052-020-8326-7`.

[60] The CMS Collaboration. Measurements of properties of the higgs boson in the W boson pair decay channel in proton-proton collisions at $\sqrt{s} = 13$ TeV. CMS Physics Analysis Summary CMS-PAS-HIG-20-013, CERN, 2022. URL: `http://cds.cern.ch/record/2803738`.

[61] Enrico Bothmann, Gurpreet Singh Chahal, Stefan Höche, Johannes Krause, Frank Krauss, Silvan Kuttimalai, Sebastian Liebschner, Davide Napoletano, Marek Schönherr, Holger Schulz, and et al. Event generation with sherpa 2.2. *SciPost Physics*, 7(3). URL: `http://dx.doi.org/10.21468/SciPostPhys.7.3.034, doi:10.21468/scipostphys.7.3.034`.

[62] Steffen Schumann and Frank Krauss. A Parton shower algorithm based on Catani-Seymour dipole factorisation. *JHEP*, 03:038, 2008. `arXiv:0709.1027, doi:10.1088/1126-6708/2008/03/038`.

[63] Christian Bierlich, Andy Buckley, Jonathan Butterworth, Christian Holm Christensen, Louie Corpe, David Grellscheid, Jan Fiete Grosse-Oetringhaus, Christian Gutschow, Przemyslaw Karczmarczyk, Jochen Klein, Leif Lönnblad, Christopher Samuel Pollard, Peter Richardson, Holger Schulz, and Frank Siegert. Robust independent validation of experiment and theory: Rivet version 3. *SciPost Physics*, 8(2), feb 2020. URL: `https://doi.org/10.21468%2Fscipostphys.8.2.026`, `doi:10.21468/scipostphys.8.2.026`.

[64] Vardan Khachatryan et al. Measurement of differential cross sections for top quark pair production using the lepton+jets final state in proton-proton collisions at 13TeV. *Phys. Rev. D*, 95:092001, 2017. `arXiv:1610.04191`, `doi:10.1103/PhysRevD.95.092001`.

[65] Simone Alioli, Paolo Nason, Carlo Oleari, and Emanuele Re. A general framework for implementing NLO calculations in shower Monte Carlo programs: the POWHEG BOX. *JHEP*, 06:043, 2010. `arXiv:1002.2581`, `doi:10.1007/JHEP06(2010)043`.

[66] John M. Campbell, R. Keith Ellis, and Walter T. Giele. A multi-threaded version of MCFM. *Eur. Phys. J. C*, 75:246, 2015. `arXiv:1503.06182`, `doi:10.1140/epjc/s10052-015-3461-2`.

[67] The CMS Collaboration. An embedding technique to determine $\tau\tau$ backgrounds in proton-proton collision data. *JINST*, 14:P06032, 2019. `arXiv:1903.01216`, `doi:10.1088/1748-0221/14/06/P06032`.

[68] Rikkert Frederix and Stefano Frixione. Merging meets matching in MC@NLO. *Journal of High Energy Physics*, 2012(12), dec 2012. URL: `https://doi.org/10.1007%2Fjhep12%282012%29061`, `doi:10.1007/jhep12(2012)061`.

[69] Keith Hamilton, Paolo Nason, and Giulia Zanderighi. Finite quark-mass effects in the NNLOPS POWHEG+MiNLO Higgs generator. *JHEP*, 05:140, 2015. `arXiv:1501.04637`, `doi:10.1007/JHEP05(2015)140`.

[70] Sara Bolognesi, Yanyan Gao, Andrei V. Gritsan, Kirill Melnikov, Markus Schulze, Nhan V. Tran, and Andrew Whitbeck. Spin and parity of a single-produced resonance at the lhc. *Phys. Rev. D*, 86:095031, Nov 2012. URL: `https://link.aps.org/doi/10.1103/PhysRevD.86.095031`, `doi:10.1103/PhysRevD.86.095031`.

[71] David L. Rainwater, R. Szalapski, and D. Zeppenfeld. Probing color singlet exchange in Z + two jet events at the CERN LHC. *Phys. Rev.*

D, 54:6680, 1996. `arXiv:hep-ph/9605444, doi:10.1103/PhysRevD.54.6680`.

[72] Simone Alioli, Sven-Olaf Moch, and Peter Uwer. Hadronic top-quark pair-production with one jet and parton showering. *JHEP*, 01:137, 2012. `arXiv:1110.5251, doi:10.1007/JHEP01(2012)137`.

[73] Diederik P. Kingma and Jimmy Ba. Adam: A method for stochastic optimization. In *3rd International Conference on Learning Representations, ICLR 2015, San Diego, CA, USA, May 7-9, 2015, Conference Track Proceedings*, 2015. URL: `https://arxiv.org/abs/1412.6980`, `arXiv:1412.6980`.

[74] D. R. Cox. The regression analysis of binary sequences. *J R Stat Soc Series B*, 20:215, 1958. `doi:10.1111/j.2517-6161.1958.tb00292.x`.

[75] Ian Goodfellow, Yoshua Bengio, and Aaron Courville. *Deep learning*. MIT Press, 2016. `http://www.deeplearningbook.org`.

[76] Giampiero Passarino. Higgs CAT. *Eur. Phys. J. C*, 74:2866, 2014. `arXiv:1312.2397, doi:10.1140/epjc/s10052-014-2866-7`.

[77] The CMS Collaboration. Precision luminosity measurement in proton-proton collisions at $\sqrt{s} = 13$ TeV in 2015 and 2016 at CMS. *Eur. Phys. J. C*, 81:800, 2021. `arXiv:2104.01927, doi:10.1140/epjc/s10052-021-09538-2`.

[78] The CMS Collaboration. CMS luminosity measurement for the 2017 data-taking period at $\sqrt{s} = 13$ TeV. CMS Physics Analysis Summary CMS-PAS-LUM-17-004, 2017. URL: `https://cds.cern.ch/record/2621960`.

[79] The CMS Collaboration. CMS luminosity measurement for the 2018 data-taking period at $\sqrt{s} = 13$ TeV. CMS Physics Analysis Summary CMS-PAS-LUM-18-002, 2019. URL: `https://cds.cern.ch/record/2676164`.

[80] Albert M Sirunyan et al. Performance of the CMS Level-1 trigger in proton-proton collisions at $\sqrt{s} = 13\,\text{TeV}$. *JINST*, 15:P10017, 2020. `arXiv:2006.10165, doi:10.1088/1748-0221/15/10/P10017`.

[81] Stefano Catani, Daniel de Florian, Massimiliano Grazzini, and Paolo Nason. Soft gluon resummation for Higgs boson production at hadron colliders. *JHEP*, 07:028, 2003. `arXiv:hep-ph/0306211, doi:10.1088/1126-6708/2003/07/028`.

[82] M. Cacciari, S. Frixione, M. L. Mangano, P. Nason, and G. Ridolfi. The $t\bar{t}$ cross-section at 1.8TeV and 1.96TeV: a study of the systematics due to parton densities and scale dependence. *JHEP*, 04:068, 2004. `arXiv:hep-ph/0303085, doi:10.1088/1126-6708/2004/04/068`.

[83] The ATLAS Collaboration. Measurement of the inelastic proton-proton cross section at $\sqrt{s} = 13$ TeV with the atlas detector at the lhc. *Phys. Rev. Lett.*, 117:182002, Oct 2016. URL: `https://link.aps.org/doi/10.1103/PhysRevLett.117.182002, doi:10.1103/PhysRevLett.117.182002`.

[84] The CMS Collaboration. Measurement of the inelastic proton-proton cross section at $\sqrt{s} = 13$TeV. *JHEP*, 07:161, 2018. `arXiv:1802.02613, doi:10.1007/JHEP07(2018)161`.

[85] G. Cowan. *Statistical Data Analysis*. Oxford science publications. Clarendon Press, 1998. URL: `https://books.google.it/books?id=ff8ZyWOnlJAC`.

[86] Combine tool for higgs analysis. URL: `http://cms-analysis.github.io/HiggsAnalysis-CombinedLimit/part2/settinguptheanalysis/#binned-shape-analysis`.

[87] Roger J. Barlow and Christine Beeston. Fitting using finite Monte Carlo samples. *Comput. Phys. Commun.*, 77:219–228, 1993. `doi:10.1016/0010-4655(93)90005-W`.

[88] J. Neyman and E. S. Pearson. On the problem of the most efficient tests of statistical hypotheses. *Philosophical Transactions of the Royal Society of London. Series A, Containing Papers of a Mathematical or Physical Character*, 231:289–337, 1933. URL: `http://www.jstor.org/stable/91247`.

[89] Luca Lista. Statistical Methods for Data Analysis in Particle Physics. *Lect. Notes Phys.*, 941:1–257, 2017. `doi:10.1007/978-3-319-62840-0`.